BOSTON UNIVERSITY

COLLEGE OF ENGINEERING

Dissertation

PHYSICS AND MODELING OF ION IMPLANTATION INDUCED TRANSIENT DEACTIVATION AND DIFFUSION PROCESSES IN BORON DOPED SILICON

by

SRINIVASAN CHAKRAVARTHI

B.Tech., Banaras Hindu University, 1995

Submitted in partial fulfillment of the

requirements for the degree of

Doctor of Philosophy

2001

Approved by

First Reader ______________________________

Scott T. Dunham, Ph.D.
Associate Professor of Electrical and Computer Engineering

Second Reader ______________________________

Daniel Cole, Ph.D.
Associate Professor of Manufacturing Engineering

Third Reader ______________________________

Michael Yeung, Ph.D.
Assistant Professor of Manufacturing Engineering

Fourth Reader ______________________________

Soumendra N. Basu, Ph.D.
Associate Professor of Manufacturing Engineering

ACKNOWLEDGEMENTS

I would like to first thank my research adviser, Professor Scott T. Dunham for his guidance and support that greatly enhanced my graduate school education at Boston University. His expertize in the field of process modeling and his curiosity to learn more made my experience extremely enjoyable and rewarding.

I would like to thank committee members Professors Dan Cole, Michael Yeung, Soumendra Basu for their constructive comments related to my research and dissertation. I am also deeply indebted to Professor Theodore Moustakas for agreeing to serve as my oral committee chairman.

I would like to thank Professor Soumendra N. Basu for his guidance as my academic adviser during the course of my doctoral work. I would like to thank Professor Michael Yeung for introducing me to process modeling.

I would like to acknowledge the Semiconductor Research Corporation whose financial support made this research project possible.

My many thanks also go to Dr. Alp Gencer for providing with the DOPDEES framework which was almost used exclusively in this work. My colleagues (present and past) and friends from the electronic materials community in the boston area (in no particular order): Brendon Murphy, Pavel Fastenko, Dr. Marius Bunea, Dr. Alp Gencer, Dr. Mitra Navi, Dr. Iuval Clejan, Dr. Anu Agarwal, Aimee Smith, and Dr. Dharanipal Doppalapudi have been good friends and provided with invaluable suggestions, discussions and support.

I would like to thank the following people for discussions and providing their experimental data: Dr. Nick Cowern, Dr. Aditya Agarwal, Dr. Iuval Clejan, Dr. Dan Downey, Dr. Martin Giles, Dr. Hans Gossmann, Dr. Sandro Solmi, Dr. Silva Theiss. I would also like to thank Dr. Martin Giles and the process modeling group at Intel TCAD for giving me a chance to work with them, as part of a summer internship in 1997.

Lastly, I would like to express my love and gratitude to my parents who kept me focused and encouraged me to do my best, to my sisters for their constant support. I would also like to acknowledge all my friends who made my graduate school experience memorable.

PHYSICS AND MODELING OF ION IMPLANTATION INDUCED TRANSIENT DEACTIVATION AND DIFFUSION PROCESSES IN BORON DOPED SILICON

(Order No.)
SRINIVASAN CHAKRAVARTHI
Boston University, College Of Engineering, 2001
Major Professor: Scott T. Dunham,
Associate Professor of Electrical and Computer Engineering

ABSTRACT

The economics of silicon processing requires predictive modeling capabilities for the continued rapid advancement of semiconductor technology. This is because it has become prohibitively expensive to develop a new process by running a large series of test lots through multi-billion dollar fabrication facilities. Effective process modeling requires an accurate physical understanding of the various interacting processes. The complexity of this problem is compounded by highly non-equilibrium phenomena associated with IC fabrication processes such as implantation annealing. Point defect supersaturations of many orders of magnitude are introduced following ion implantation, which is used to introduce the dopants into silicon. Such supersaturations dramatically alter the diffusion of dopants and reduce the electrical activation during the initial phase of the anneal.

Boron is the primary *p*-type dopant used in silicon and thus understanding and modeling its deactivation/activation and diffusion is critical to predictive process simulation. Since boron is smaller than silicon, boron agglomerates with interstitials becoming electrically inactive. Modeling of boron clusters is complicated, as there is a huge array of potential boron-interstitial cluster compositions. A physical model for boron clustering is derived by identifying dominant clusters and rate limiting steps via atomistic calculations performed at Lawrence Livermore National Labs. The model is then used successfully to match a wide variety of chemical and electrical data. We further apply this model to understand and successfully predict ultra shallow junction formation. We find it is possible to explain some intriguing phenomenon observed during the formation of ultra shallow junctions, like saturation in junction depth despite increasing ramp-up rates.

Researchers are exploring novel experimental processing steps like high energy Si preimplants to produce highly active and shallow B junctions. To understand and model this phenomenon it is essential to be able to model the evolution of the excess vacancy region formed after the implant. Hence we have developed a detailed model for vacancy clustering built based on atomistic calculations and verified the model by comparison to data from gold labeling experiments. However this model is computationally intractable for routine use in TCAD (Technology Computer Aided Design). Hence, a computationally efficient

physical model has been derived from this full model that can be readily incorporated into process simulators.

This research leads to an understanding of a broad range of data applicable to both current and future generation of devices and present a self-consistent model which can be incorporated into TCAD diffusion equation solvers.

Contents

1 Introduction **1**

2 Dopant Diffusion in Silicon **5**

2.1 Atomistic perspective of dopant diffusion . . . 5

2.1.1 Vacancy mechanism . . . 6

2.1.2 Interstitial mechanism . . . 7

2.2 Coupled diffusion . . . 11

2.3 Point defect properties . . . 18

2.4 Metal diffusion . . . 18

2.4.1 Zinc diffusion . . . 19

2.4.2 Platinum diffusion . . . 20

2.5 Boron indiffusion . . . 30

2.6 Summary . . . 32

3 Ion Implant Damage Evolution **33**

3.1 Initial damage . . . 33

3.2 Early work on boron deactivation and TED . . . 35

3.3 Interstitial clusters . . . 36

3.4 Boron interstitial clusters . . . 37

3.5 Vacancy clusters . . . 41

3.6 Simulation of initial damage . . . 42

3.6.1 Effect of surface . . . 42

3.6.2 Effect of clustering during recombination . . . 43

3.7 Summary . . . 48

4 Boron Cluster Models **49**
4.1 Kinetic precipitation model . . . 49
4.2 Multi cluster models . . . 55
4.2.1 Analysis of model . . . 56
4.3 Simple cluster model . . . 57
4.4 Extension to charge states . . . 61
4.5 Comparison to chemical data . . . 64
4.6 Solid Solubility Model . . . 64
4.7 Comparison to marker layer experiments . . . 69
4.7.1 Experimental background . . . 69
4.7.2 Model results . . . 72
4.8 Comparison to electrical activation data . . . 78
4.9 Summary . . . 83

5 Ultra Shallow Boron Junctions **84**
5.1 Rapid thermal soak anneals . . . 84
5.2 Spike anneals . . . 89
5.3 Summary . . . 98

6 High Energy Implants and Vacancy Clustering **99**
6.1 Vacancy cluster model . . . 99
6.2 Comparison to Au-labeling experiments . . . 102
6.3 Moment based models . . . 111
6.4 Summary . . . 120

7 Conclusions and Future Work **121**
7.1 Summary . . . 121
7.2 Future Directions . . . 122

8 Bibliography **124**

9 Vita **133**

List of Tables

4.1 Cluster energetics based on atomistic calculations [60] used for the full system. 56

6.1 Parameters from Bongiorno *et al*. [11] used for the simulations. $E_\mathrm{f}(n)$ is the formation energy and $E_\mathrm{b}(n)$ is the binding energy in eV. We use SPC formation energies for $n > 24$ and HRC for the clusters smaller than 25. . 103

List of Figures

1.1 Cost per lot of 25 wafers of packaged DRAM with time, for each DRAM generation labeled as bits per chip. 3

1.2 A MOS transistor showing how a source/drain implant affects the channel dopant distributions during annealing. The interstitial flux not only leads to an enhanced dopant diffusion in the source/drain but also that in the channel region. Further such interactions become more critical with decrease in lateral channel length. 4

2.1 The dopant (D) vacancy (V) pair migration in a silicon lattice. The dopant and vacancy start the diffusion step as first nearest neighbors. The hopping rates are such that the dopant can hop into the empty site and back many times without any effect on diffusion. The host atoms, though, could also hop into the empty site such that at some point the vacancy moves to a third nearest neighbor site with respect to the dopant. The vacancy can go around the six member ring of atoms and approach the dopant from a different direction. After the dopant hops into the now empty site the dopant vacancy pair completes one diffusion step. 6

2.2 Schematic of kick-out mechanism showing interstitial assisted mechanism of diffusion. In (a) the dark atom is the substitutional dopant atom to be kicked out by the silicon self interstitial (unfilled atom). (b) shows the dopant atom that is now kicked into an interstitial site and can now diffuse in the lattice. 8

2.3 Diffusion path for boron interstitial for the kick-out mechanism as calculated by Zhu *et al.* [103]. 10

2.4 Comparison of the diffusion path for boron via the kick-out mechanism as calculated by Windl *et al.* [98] for (a) neutral (b) negative charge states. . 10

2.5 Normalized zinc diffusion profiles at 870°C into defect-free silicon and comparison to simulations using point defect parameters from Bracht *et al.* [12]. 20

2.6 Normalized zinc diffusion profiles at 1208°C into defect-free silicon and comparison to simulations using point defect parameters from Bracht *et al.* [12]. . . . 21

2.7 Normalized zinc diffusion profiles at 870°C into defect-free silicon and comparison to simulations using point defect parameters obtained in this work. . . . 22

2.8 Normalized zinc diffusion profiles at 1208°C into defect-free silicon and comparison to simulations using point defect parameters obtained in this work. . . . 23

2.9 Measured and simulated platinum profiles at 770°C [105]. . . . 24

2.10 Measured and simulated platinum profiles at 700°C [106]. Note the uniform Pt concentration in bulk which is unchanged with time, and the inverse U profile. . . . 25

2.11 Effect of carbon on zinc diffusion at 870°C. Carbon has only a minor effect even at the lowest available diffusion temperature. . . . 26

2.12 Extracted values of $D_{\mathrm{V}}C_{\mathrm{V}}^{*}/C_{s}$, $D_{\mathrm{I}}C_{\mathrm{I}}^{*}/C_{s}$ (C_{s} is the silicon lattice density) from fitting Zn diffusion data of Bracht *et al.* [12] and comparison to previous analysis based on metal diffusion [49]. . . . 27

2.13 Extracted values of C_{V}^{*} and C_{I}^{*} from fitting Zn diffusion data of Bracht *et al.* [12] and comparison to previous analysis based on both metal diffusion and atomistic calculations [94]. . . . 28

2.14 Effect of variation in a single point defect parameter and reoptimizing all the profiles. It can be seen that $D_{\mathrm{I}}C_{\mathrm{I}}^{*}$ is the most reliably extracted parameter and C_{V}^{*} is the least. . . . 29

2.15 Boron diffusion from implanted polysilicon from Garben *et al.* [39] and comparison to prediction of coupled diffusion model. Also shown is prediction by Fermi model not considering point-defect mediated diffusion. 30

2.16 Boron indiffusion for the highest surface concentration, also plotted is $C_{\mathrm{I}}/C_{\mathrm{I}}^{*}$. Note that the tail diffusion is enhanced by a factor of about 3. . . . 31

3.1 Total and net damage created by a 40 keV, 5×10^{13} cm^{-2} Si implant. Monte Carlo simulations with TRIM [10]. . . . 34

3.2 Monte Carlo simulation showing net initial distributions of interstitials and vacancies following a 2 MeV, 1×10^{16} cm^{-2} Si implant. The vacancy rich layer extends well over a μm. . . . 35

3.3 Boron chemical (SIMS) and activation (SRP) profiles after annealing of a $2 \times 10^{15}\,\mathrm{cm}^{-2}$ dose implant at 850°C for 2 h. The peak of the implanted boron profile is immobile and inactive to concentrations well below equilibrium solubility (from Solmi *et al.* [90]). Equilibrium boron solid solubility at 850°C $\sim 5 \times 10^{19}\,\mathrm{cm}^{-3}$. 37

3.4 Delta doped boron marker layer after TED driven by a $5 \times 10^{13}\,\mathrm{cm}^{-2}$, 40 keV Si implant and annealed at 790°C for 10 mins. 38

3.5 Area density of interstitials contained in {311} defects as a function of background boron concentration following anneal at 740°C for 15 mins. The solid line is a fit to the data assuming a quadratic dependence on B concentration. This would be the dependence of a cluster of type $B_{2m}I_m$. . 39

3.6 Clustering driven by a $2 \times 10^{13}\,\mathrm{cm}^{-2}$, 40 keV Si implant for a B marker layer of doses $2 \times 10^{13}\,\mathrm{cm}^{-2}$, annealed at 800°C for 35 mins. 40

3.7 Clustering driven by a $2 \times 10^{13}\,\mathrm{cm}^{-2}$, 40keV Si implant for a B marker layer of doses $9 \times 10^{13}\,\mathrm{cm}^{-2}$, annealed at 800°C for 35 mins. Note that a low interstitial dose can deactivate a much larger fraction of boron. 41

3.8 Net interstitial dose remaining after the recombination process starting from the total initial defect distributions. E_b is the barrier to I/V recombination. 43

3.9 Dose dependence of TED measured for a boron marker layer following 200 keV Si implants. A “+n” model based on the full initial defect profile is able to predict diffusion behaviour. 44

3.10 Prediction of B TED for 40 keV $10^{13}\mathrm{cm}^{-2}$ B implant. A “+1” model predicts less diffusion than seen experimentally. A “+n” model based on the full initial defect profile is able to predict diffusion behaviour. Data is from Intel Corp. [44]. 45

3.11 Interstitial super-saturations at 600°C and 800°C obtained using full damage (bold lines) and using a “+1” model (dashes). Note that the supersaturations obtained are almost independent of the initial conditions. . . . 46

3.12 Figure shows evolution of interstitial and vacancy clusters during annealing of a $2 \times 10^{13}\mathrm{cm}^{-2}$ Si implant at 600°C. The vacancies exist till around 600 sec, after which the interstitials trapped in interstitial clusters is close to a “+1”. 47

4.1 Array of possible BICs. Also indicated schematically are the range of compositions considered by cluster and KPM approaches. 50

4.2 Simulations results for a $2 \times 10^{14}\,\mathrm{cm}^{-2}$, 40 keV B implant annealed at 700°C using KPM model compared to data from Intel Corp. [44]. 52

4.3 Simulations results for a 2×10^{14} cm^{-2}, 40 keV B implant annealed at 800°C using KPM model compared to data from Intel Corp. [44]. 53

4.4 Simulations results for a 2×10^{14}cm^{-2}, 80 keV B implant annealed at 800°C using KPM model, compared to data from Intel Corp. 54

4.5 Cluster reactions considered in the full model as given by fundamental physical calculations [102]. 55

4.6 Simulations using the full cluster model of normalized cluster concentrations (relative to their equilibrium value) versus time for an 800°C anneal. 58

4.7 Equilibrium cluster concentrations versus free boron concentration at 800°C for free interstitial concentrations of $10^9 C_I^*$ characteristic of very early stages of TED. Initially, BI_2 is the primary cluster and helps immobilize the boron as noted by Pelaz *et al.* [83] 59

4.8 Equilibrium cluster concentrations versus free boron concentration at 800°C for free interstitial concentrations of $10^3 C_I^*$ typical of TED conditions in the presence of {311} defects. B_3I is the primary cluster during most of the anneal. 60

4.9 Comparison of full model with the simplified model for a 40 keV 2×10^{14} cm^{-2} B implants annealed at 800°C for various times. Also shown for comparison are SIMS data from Intel [44]. Note that the full model and simple model show indistinguishable final profiles. The B_3I concentrations for the two models (shown after a 1 h anneal) are also nearly identical. . . . 61

4.10 Comparison of simulation to experimental data [44] for 2×10^{14} cm^{-2} (a) 20 keV (b) 80 keV boron implants after 1 hr anneals at 800°C. 65

4.11 Comparison of simple model to data from Solmi *et al.* [90] for a 5×10^{14} cm^{-2} 20 keV B implant annealed at 800°C for (a) 30 min (b) 2 hr. 66

4.12 Comparison of model to experimental data [44] for a 2×10^{15} cm^{-2} 40 keV boron implant after a 60 min anneal at 800°C. 67

4.13 Comparison of model to experimental data for a 2×10^{15} cm^{-2}, 20 keV B implant annealed at 800°C for 2 hrs. SIMS data is from Solmi *et al.* [90] 68

4.14 SIMS profiles of boron before and after annealing for a range of times at 600°C. Data from Mannino *et al.* [68]. Also plotted is the total damage from the Si implant as calculated by UTMARLOWE [62]. 70

4.15 Supersaturations observed by the deeper marker layers for Wafer A (No B layer) and Wafer B (B layer) shown with time at 600°C. Data from Mannino *et al.* [68]. 71

4.16 The figure sketches the depth and time variation of $S(x,t)$ in wafers A and B after the initial BIC nucleation phase (after Mannino *et al.* [68]). 72

4.17 SIMS profiles of boron before and after annealing at 600°C for 1 sec compared to experimental SIMS data. Experimental data from Mannino *et al.* [68]. 74

4.18 SIMS profiles of boron before and after annealing at 600°C for 15 min compared to experimental SIMS data. Experimental data from Mannino *et al.* [68]. 75

4.19 SIMS profiles of boron before and after annealing at 600°C for 2 h compared to experimental SIMS data. Experimental data from Mannino *et al.* [68]. 76

4.20 Simulated supersaturations compared to experimentally observed values at 600°C. Experimental data from Mannino *et al.* [68]. 77

4.21 Comparison of experimentally-measured active fraction [87] to model for 150 keV, $2 \times 10^{14}\,\mathrm{cm}^{-2}$ and $2 \times 10^{15}\,\mathrm{cm}^{-2}$ boron implants annealed for 30 min. at various temperatures. Lines represent model predictions, and symbols represent data. 79

4.22 Comparison of simulated and experimentally measured active fraction for a $2 \times 10^{14}\,\mathrm{cm}^{-2}$ boron implant annealed at 800°C. Data from Pelaz *et al.* [84]. 80

4.23 Comparison of simulation with SIMS and SRP data from Pelaz *et al.* [84] for a $2 \times 10^{14}\,\mathrm{cm}^{-2}$ implant annealed at 800°C for 1 s. Note that most of the boron is already in clusters. 81

4.24 Comparison of simulation with SIMS and SRP data from Pelaz *et al.* [84] for a $2 \times 10^{14}\,\mathrm{cm}^{-2}$ implant annealed at 800°C for 1000 s. 82

5.1 Simulated and measured boron profiles following $10^{15}\mathrm{cm}^{-3}$ boron implants at 0.5 to 5 keV. Data from Agarwal *et al.* [3]. 85

5.2 Comparison between simulated and measured broadening of boron delta-doped super-lattices in the presence of an MBE-deposited boron layer and annealing at 950°C for 10 sec. Data from Agarwal *et al.* [3]. 86

5.3 Comparison between simulated and measured broadening of boron delta-doped super-lattices in the presence of an MBE-deposited boron layer and annealing at 1050°C for 10 sec. Data from Agarwal *et al.* [3]. 87

5.4 Predicted and measured diffusivity enhancement of boron marker layers for various 0.5 keV boron implant doses and annealing at 1050°C for 10 sec. Data from Agarwal *et al.* [2]. 88

5.5 Temperature dependence of MBE marker layers as reported by Agarwal *et al.* [6] and compared to simulations. As observed at 800°C there is no enhancement, however a preanneal at 1050°C maintains an enhancement. The enhancements at higher temperature are plotted for 10 s. 89

5.6 Temperature versus time profiles used for the simulations. Ramp-up is modeled as linear whereas cool down is radiative. 91

5.7 Boron profiles versus oxygen partial pressure for 1keV, 10^{15}cm^{-2} boron implants annealed 10 s at 1050°C (Lerch *et al.* [65]) are shown along with simulations matched to these profiles by varying the surface interstitial concentration. 92

5.8 The effect of ramp rate on reduction in junction depth for 1×10^{15}cm^{-2} B implants following 1050°C spike anneals. The difference in junction depth (x_j@5×10^{18} cm^{-3}) relative to a ramp-up rate of 2000°C/s is shown for various implant energies. 93

5.9 The effect of ramp rate on reduction in junction depth for 1×10^{15}cm^{-2} B implants following 1050°C spike anneals. The effect of changing the cooling rate is shown. Note that increasing the ramp-down rate gives a greater junction depth reduction for higher ramp-up rates, since more of the TED then occurs during ramp-down. 94

5.10 Comparison of simulation and experiment for a 1×10^{15}cm^{-2} 250 eV B^+ implant for a 1050°C spike anneal in 33 ppm O_2 in N_2 ambient. Ramp-up rates are 50°C/s and 425°C/s, and initial ramp-down rate is 87°C/s. Data from Downey *et al.* [30]. 95

5.11 Comparison of simulation and experiment for a 1×10^{15}cm^{-2} 500 eV B^+ implant for a 1050°C spike anneal in 33 ppm O_2 in N_2 ambient. Ramp-up rates are 50°C/s and 425°C/s, and initial ramp-down rate is 87°C/s. Data from Downey *et al.* [30]. 96

5.12 Comparison of simulation and experiment for a 1×10^{15}cm^{-2} 1 keV and implant for a 1050°C spike anneal in 33 ppm O_2 in N_2 ambient. Ramp-up rates are 50°C/s and 425°C/s, and initial ramp-down rate is 87°C/s. Data from Downey *et al.* [30]. 97

6.1 Boron profiles formed from a 2×10^{14} cm^{-2}, 5 keV B implant after a two-step anneal at 800°C/60sec and then 1000°C/15sec. A shallower junction is formed if a 100 keV Si pre-implant is used prior to the boron implantation. 100

6.2 Cluster energetics calculations from Bongiorno *et al.* [11]. It can be noted that for small clusters ($n < 24$), Hexagonal Ring Clusters are more energetically favorable with respect to Spheroidal Clusters. 101

6.3 Simulated size distribution of clusters after a short time anneal at 750°C and 950°C. Clusters are ripening into larger clusters more predominantly at the higher temperature. This also shows the most stable small cluster sizes to be around 6, 10, 14, 18 and 24 due to the non-monotonic binding energy. 104

6.4 Simulated clustered vacancy concentrations compared to Au RBS data for 750°C anneals of 10 min and 1 h. Simulation show that there is very litle change in the clustered vacancy concentration between 10 min and 1 h. This is in agreement with results from Venezia *et al*. [96] who also report that Au concentrations are nearly constant for longer anneals up to 8 h at 750°C. Note that the surface peak in the data is because of the Au implant used for the in-diffusion. 105

6.5 Simulated and clustered vacancy concentrations compared to Au RBS data after 950°C anneal of 10 s and 10 min. At 950°C, vacancy clusters are annihilated by an increased dissolution of interstitial defects from the bulk and loss to the surface. Note that the simulations agree well with the time dependence of the data. 106

6.6 Simulation and clustered vacancy concentrations compared to Au RBS data after a 1000°C anneal of 10 min. At 1000°C, the vacancy clusters are increasingly annihilated from the surface and the dissolution of interstitial defects from the bulk. The clusters around $R_p/2$ are the largest and therefore the most stable. Hence there is a peak in cluster concentration at $R_p/2$ (0.9 μm) in the simulations similar to that observed in the experimental data [96]. 107

6.7 At 750°C, a considerable fraction of the vacancies are in smaller sized clusters. 108

6.8 The above figure shows the significance of the addition of larger sized clusters. At 950°C most of the clusters especially around $R_p/2$ have ripened into larger clusters ($n > 35$). 109

6.9 Time dependence of vacancies in system (depth of 1000 μm). Using only a $\{311\}$ model without any loop formation leads to dissolution of all the clusters by about 60 s, contrary to experiments. It should be noted that the experimental value reported by Venezia *et al*. [96] is measured between 0.2 – 1 μm to avoid including the Au implant profile. This method also leaves out the dose of vacancies below 0.2 μm. Hence the experimental results are expected to be lower than the simulation results despite having a good agreement in the depth distributions. Also, without loops the vacancy concentration drops below the equilibrium value due to the interstitial supersaturation from the dissolving $\{311\}$ defects. 110

6.10 γ_0 values extracted from simulations of the full system of rate equations for three different temperatures (400, 800, 1000°C) . Also shown in the same plot is γ_0 value for a 1000°C anneal after a preanneal at 400°C. Note that the γ_0 is almost independent of its thermal history. 114

6.11 γ_1 values extracted from simulations of the full system of rate equations for three different temperatures (400, 800, 1000°C) . Also shown in the same plot is γ_1 value for a 1000°C anneal after a preanneal at 400°C. Note that the γ_1 is almost independent of its thermal history. 115

6.12 Analytic fit to γ_0 neglecting small size effects. This was done to avoid the exponential change in γ_i values. 116

6.13 Analytic fit to γ_1 neglecting the near exponential change near small sizes. 117

6.14 Comparison of AKPM and full discrete cluster model at 950°C 118

6.15 Comparison of AKPM and full discrete cluster model at 1000°C 119

Chapter 1

Introduction

One of the most important challenges in developing VLSI technology today is to shrink device sizes to their limits, since both the speed and the number of transistors per unit area increase as devices get smaller. Each new generation requires a large developmental effort, traditionally executed by scaling the existing technology generation to the requirements of the new generation and addressing emerging problems with a series of matrix-type experiments. Wafer lots are processed and in each lot selected parameters are varied. An existing technology is similarly fine-tuned while commercial product is shipped to customers. Fig. 1.1 illustrates that this approach becomes prohibitively expensive, with the current cost per DRAM lot, or one experiment at about a million dollars today, and projected to exceed 10 million dollars in 2012. For the figure it was assumed that 50% of a wafer area yields usable dies; and packaging is included in the cost [1, 52]. This makes computer-aided technology development imperative, requiring accurate, truly predictive simulation tools. The goal, therefore, consists of replacing real experiments with virtual ones, i.e. a new process is placed in manufacturing only after it has been ascertained, in computer simulations of the proposed sequence, that the resulting devices will meet all the specifications. Current process simulators contain empirical models and often lack physical elements needed for accurate simulation. However, the ever-progressing shrinkage of device dimensions and tolerances leads to new non-equilibrium processes that can not be modeled using empirical models commonly used in the industry. Thus physics-based models are necessary for use in these process simulators.

Ion implantation is the most powerful and widely used tool for the introduction of dopants in silicon device technology. However, implantation also introduces a large amount of crystal damage to the semiconductor. This damage consists of high concentrations of interstitials and vacancies and is much higher than the implant dose. Hence, any subsequent annealing step is a highly non-equilibrium process and involves the formation/dissolution of extended defects, metastable phases and precipitates. Unfortunately, the introduced dopants themselves do not all lie on substitutional sites. Therefore, a high temperature post implant anneal is necessary to activate the dopant atoms and remove damage which

compromises device performance. As a result of this high temperature anneal, both point defects and dopant atoms experience a period of high mobility. This activation process is characterized by anomalous diffusion in that during post-implant annealing dopant atoms may actually diffuse much larger distances for low temperature anneals compared to higher temperature anneals. This anomalous dopant diffusion during the anneal of an implant is know as transient enhanced diffusion (TED). Due to the highly non-equilibrium point defect concentrations involved, dopant atoms may also form inactive immobile clusters and deactivate much below their solid solubility. This is a characteristic exhibited during TED by smaller atoms like boron whose agglomeration is enhanced by excess interstitials. In devices with large critical dimensions, this diffusion of dopants during post-implant annealing may not significantly affect device performance. However, with continued shrinkage of devices, even minor changes in dopant distributions may lead to large changes in electrical behavior of the devices. For example, in a MOS device as shown schematically in Fig 1.2, the source/drain implant and associated interstitial excess leads to a change in the dopant distribution in the channel region as well as in the source and drain regions. The final dopant distribution is thus a net sum of a wide range of atomic interactions. In order to predict the final threshold voltage of this device, it is necessary to model all these complex interactions simultaneously. The simulation of such a system involves a large number of parameters to describe each mechanism. Specially designed and tailored experiments have been used successfully to identify key mechanisms. Though these experiments have been very helpful to better understand important processes they are still limited in their ability to separate mechanisms at an atomic level. For example, while experiments are able to find the total diffusion coefficient, they generally can not determine the microscopic diffusion mechanism. Recent advances in atomistic techniques such as *ab-initio* and molecular dynamics provide further information to probe more deeply into the various atomistic mechanisms of diffusion and defect interactions, thus bridging the knowledge gap.

This research has the following unique features:

- Knowledge from atomistic calculations is used (when available), coupled with experimental knowledge in developing physical models.

- Our work relies on a physical model of diffusion and interaction of dopant atoms and point defects, rather than on an empirical approach.

- The work is based on the evolution of the size distributions of extended defects during TED.

- It includes deactivation of boron and incorporation of point defects into boron clusters or precipitates.

- Simple computationally efficient models are derived from complex but physical models developed during the work, for incorporation into process simulators.

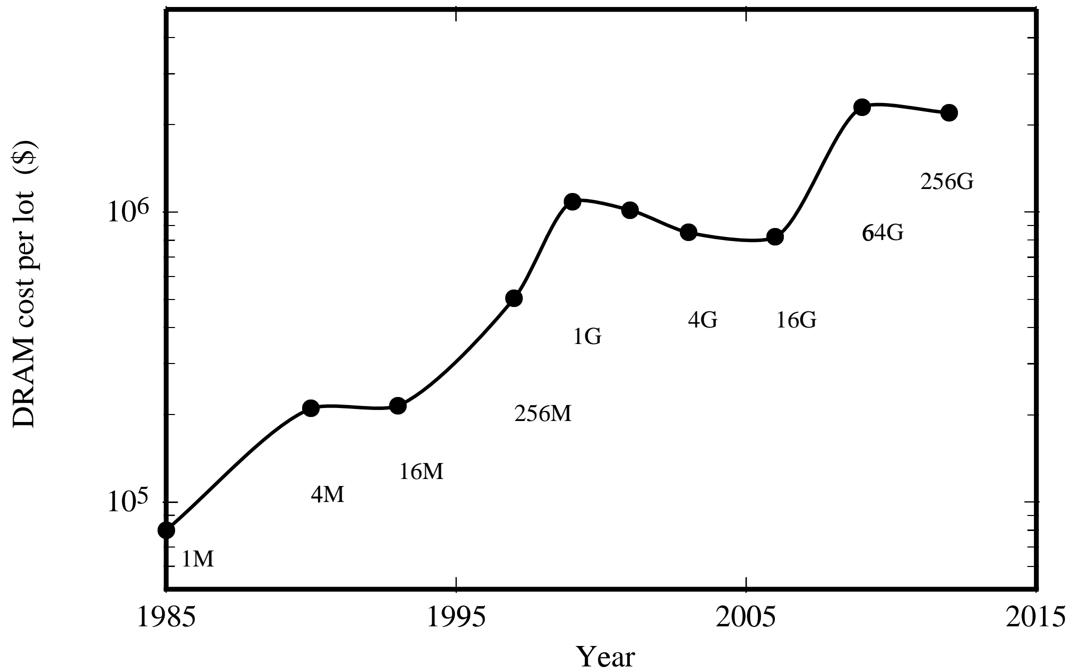

Figure 1.1: Cost per lot of 25 wafers of packaged DRAM with time, for each DRAM generation labeled as bits per chip.

We begin Chapter 2 by discussing the mechanism of boron diffusion in silicon and its interaction with point-defects. We gain valuable insights into the point-defect parameters used in the simulations by comparison to an extensive data set from metal diffusion experiments. In Chapter 3, various experiments by different researchers are analyzed to identify the primary physical mechanisms occurring during TED and lay the framework for our modeling efforts. We also look at the assumptions made for the initial cascade evolution. In Chapter 4, we consider different approaches to modeling boron clustering effects in silicon. A physical model for boron clustering is derived based on atomistic calculations. The model is then successfully used to match a wide variety of chemical and electrical activation data. In Chapter 5, we apply this model to understand and successfully predict ultra shallow junction formation. We demonstrate that we can successfully predict both qualitatively and quantitatively junction formation, including some intriguing phenomenon like saturation in junction depth despite increasing ramp-up rates. In Chapter 6, we model the formation of vacancy clusters during annealing of high energy implants. This is developed from atomistic energetics calculations of vacancy clusters. We then derive an efficient moment based model for incorporation into process simulation software. Finally, Chapter 7 summarizes the conclusions and future directions.

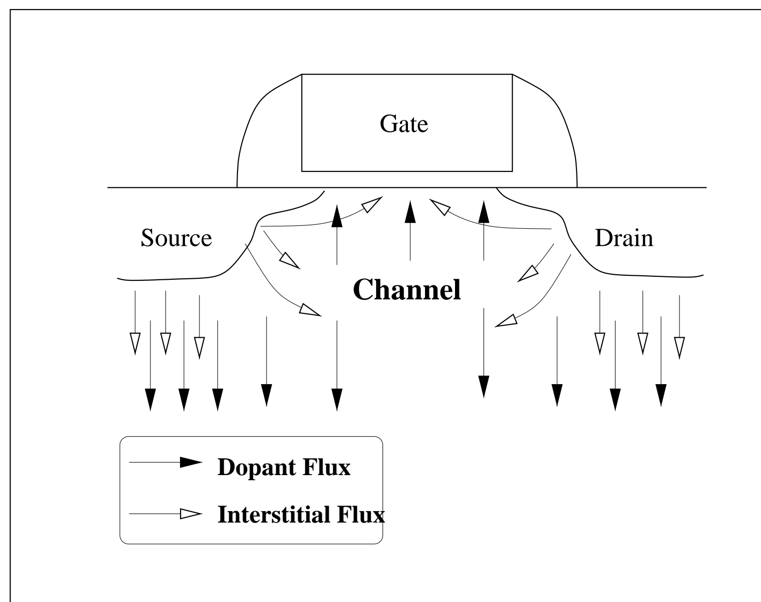

Figure 1.2: A MOS transistor showing how a source/drain implant affects the channel dopant distributions during annealing. The interstitial flux not only leads to an enhanced dopant diffusion in the source/drain but also that in the channel region. Further such interactions become more critical with decrease in lateral channel length.

Chapter 2

Dopant Diffusion in Silicon

Dopant diffusion in silicon occurs through the interaction of dopants with native point defects. This chapter is devoted to models and parameters associated with this process. We first review dopant diffusion in silicon, followed by a discussion of coupled diffusion models used in all our simulations. We then consider the properties of point defects in silicon. Finally, in Section 2.4 we present our analysis of metal diffusion experiments as a way to re-evaluate point defect properties.

2.1 Atomistic perspective of dopant diffusion

Historically, the diffusivity of dopants in silicon has been modeled macroscopically using the Arrhenius expression

$$D(T) = D_0 \exp\left(\frac{-E_a}{kT}\right) \tag{2.1}$$

where, D_0 is the pre-exponential constant and E_a is the activation energy of the diffusion constant. However, beginning with experiments performed in 1970's and 1980's, it was found that this simple diffusion model was inadequate. In these experiments, the diffusivity of dopants was seen to be different under varying environments, especially during oxidation of the silicon surface or after ion implantation [29, 38, 57, 63, 69, 76, 78]. This is because Eq. 2.1 considers only a temperature dependence of the diffusivity. In order to explain these results, a more complicated model for dopant diffusion based on point defect mediated diffusion is needed. In silicon, as in other semiconductor materials, dopant diffusion occurs via interactions with point defects, such as interstitials and vacancies. These interactions determine the dopant diffusivities.

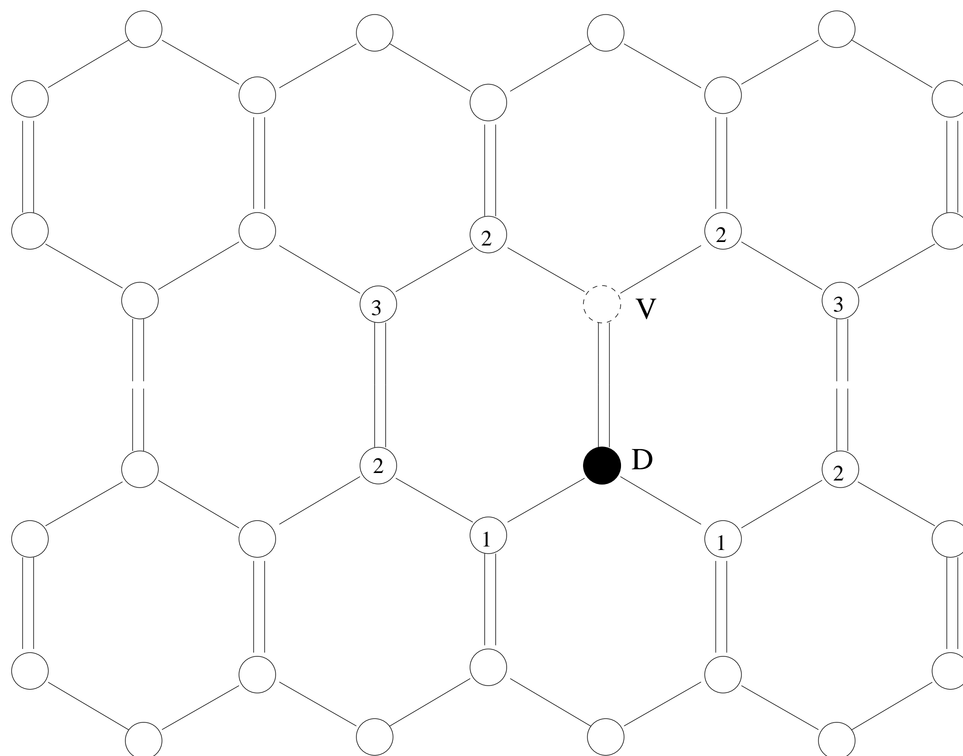

Figure 2.1: The dopant (D) vacancy (V) pair migration in a silicon lattice. The dopant and vacancy start the diffusion step as first nearest neighbors. The hopping rates are such that the dopant can hop into the empty site and back many times without any effect on diffusion. The host atoms, though, could also hop into the empty site such that at some point the vacancy moves to a third nearest neighbor site with respect to the dopant. The vacancy can go around the six member ring of atoms and approach the dopant from a different direction. After the dopant hops into the now empty site the dopant vacancy pair completes one diffusion step.

2.1.1 Vacancy mechanism

In the vacancy diffusion mechanism, a substitutional dopant atom exchanges position with an empty lattice site. This diffusion mechanism was proposed for silicon based on the experimental observation that the vacancy is the main point defect in metals [89].

A schematic of the pair diffusion is shown in Fig. 2.1. At an atomistic scale, this mechanism presents some particularities given the different dopant vacancy interactions. The vacancy mechanism does not occur through a simple vacancy dopant exchange, but through what is called a “ring mechanism.” The vacancy not only must exchange its position with the dopant but also has to move away to a third nearest neighbor site with respect to the dopant and return via a new direction for a long range migration of the dopant to take place.

Note that in the pair diffusion mechanism the resulting dopant flux is in the same direction as the vacancy flux. This is contradictory to the simple exchange mechanism in which the vacancy flux is opposite to the dopant flux. On a macroscopic scale, this process can be described by the reaction:

$$B_s + V \Leftrightarrow BV \tag{2.2}$$

For this reaction, the net rate of formation of BV from B_s and V is given as:

$$R_{BV} = 4\pi\sigma D_V (C_B C_V - \frac{C_{BV}}{K_{B/V}}) \tag{2.3}$$

where, D_V is the vacancy diffusivity, $K_{B/V}$ is the equilibrium constant given as,

$$K_{B/V} = \frac{1}{C_{Si}} \exp\left(\frac{E_B}{kT}\right). \tag{2.4}$$

C_{Si} is the number of available lattice sites in silicon $\sim 5 \times 10^{22}$ cm^{-3}, and E_B is the binding energy of BV relative to free boron and vacancy. σ is the capture radius of the reaction and is defined as:

$$\sigma = \frac{A_{cap}}{4\pi a_{hop}}. \tag{2.5}$$

a_{hop} is the hop distance of a vacancy and is taken to be equal to a_o, the lattice constant of silicon. A_{cap} is the capture cross-section of B_s and is given by,

$$A_{cap} = \pi (r_{cap})^2. \tag{2.6}$$

If $r_{cap} = 2a_0$, then $\sigma = a_0$. This is the assumption we will generally make in this work.

2.1.2 Interstitial mechanism

Experiments involving the injection of point defects into boron doped samples has shown that boron diffusion in silicon is dominated ($> 98\%$) by an interstitial mechanism [37, 53]. Most early workers assumed that the interstitial mediated diffusion occurs through an interstitialcy mechanism, i.e. the diffusing defect is a complex formed by an impurity atom and a Si atom sharing the same site [50]. For heavier atoms like Al and Au a kick-out mechanism was proposed [97, 48]. In this mechanism, a silicon self interstitial migrates through the lattice and approaches a substitutional atom. If the energy barrier is low, the substitutional atom is kicked into an interstitial position and could migrate through the silicon lattice. Fig. 2.2 shows an example of the kick-out mechanism. Cowern *et al.* [25] experimentally measured anomalous diffusion in the tails of a B concentration distribution as a result of short time anneals at low temperatures. The one-dimensional profile of the dopant after diffusion shows exponential tails not expected from Gaussian diffusion. Thus, they suggested the formation of a fast migrating intermediate species (B_i) that can diffuse

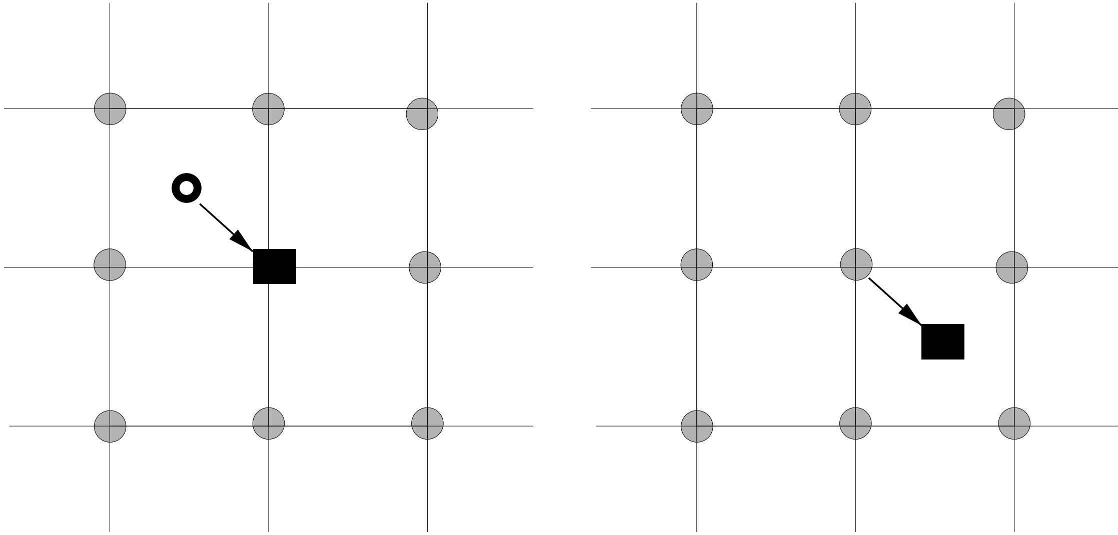

Figure 2.2: Schematic of kick-out mechanism showing interstitial assisted mechanism of diffusion. In (a) the dark atom is the substitutional dopant atom to be kicked out by the silicon self interstitial (unfilled atom). (b) shows the dopant atom that is now kicked into an interstitial site and can now diffuse in the lattice.

long distances before getting kicked back into a substitutional site. This process can be described by the reaction:

$$B_s + I \Leftrightarrow B_i. \tag{2.7}$$

To accurately model boron diffusion, it is necessary to know the atomic parameters governing the point defect energetics. First principles calculations have emerged as a tool to provide information on the energetics and different diffusion pathways in Si. The most accepted model until recently for B diffusion in Si assumed that a $B_s - Si_i^{T_{2n}}$ (a tetrahedral (T) interstitial in 2nd neighbor position with respect to B_s) pair is first formed [77]. Subsequently, the B_s becomes interstitial (B_i) by being kicked out into a [110] channel connecting hexagonal (H) and T interstitial sites. This model further suggest that in the network of [110] channels, the B_i diffuses rapidly by performing a large number of jumps before getting kicked back into a substitutional site releasing a interstitial (which may remain bound to the B_s). This mechanism (barriers from Zhu *et al.* [103]) is shown in Fig. 2.3. Macroscopically, this mechanism involves:

$$B + I \Leftrightarrow BI, \tag{2.8}$$

$$BI \Leftrightarrow B_i \tag{2.9}$$

More recently, Windl *et al.* [98, 86] have found a new boron diffusion mechanism. As shown in Fig 2.4 (a) the lowest energy configuration for the neutral case was found to be a $B_s - Si_i^{T_{1n}0}$ (a tetrahedral (T) interstitial in 1st neighbor position with respect to B_s) with a binding energy of 0.8 eV relative to neutral I^+ and B_s^-. Unlike the previous mechanism, Windl *et al.* found the B_s atom to migrate via the B_i^{S0} (a boron interstitialcy) to a hexagonal B_i^{H0} interstitial site with a migration barrier of 0.2 eV. Thus the diffusion pathway is

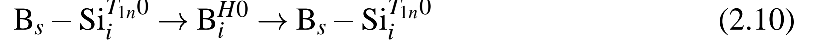

$$B_s - Si_i^{T_{1n}0} \rightarrow B_i^{H0} \rightarrow B_s - Si_i^{T_{1n}0} \tag{2.10}$$

For negatively charged systems, a B_i^{X-} (another interstitialcy configuration) was found to be the most stable configuration with a binding energy of 0.5 eV with respect to free B^- and I^0. As shown in Fig. 2.4 (b), they found a $B_i^{X-} \rightarrow B_i^{S-} \rightarrow B_i^{X-}$ path with an intermediate metastable B_i^{S-} configuration and a migration barrier of 0.6 eV. For the +1 charged system, $B_s - Si_i^{T_{1n}+}$ was found to be the most stable configuration with a binding energy of 1 eV with respect to B^- and I^{++}. However the migration pathway of a $B_s - Si_i^{T_{1n}+}$ was found to be a one-step process $B_s - Si_i^{T_{1n}+} \rightarrow B_s - Si_i^{T_{1n}+}$ with no intermediate metastable interstitial position and a migration barrier of 0.8 eV. Thus, these calculations predict that although the dominant pair is positively charged in *p*-type material, B diffusion is dominated by neutral pairs, consistent with the approximately linear dependence of B diffusivity on carrier concentration (p/n_i) as seen experimentally [99]. Thus, for all charge states the diffusion mechanism can be represented by the reaction of the type:

$$B + I \Leftrightarrow BI \tag{2.11}$$

where, BI is the lowest energy configuration for that charge state (e.g. $B_s - Si_i^{T0}$ for the neutral case), with subsequent diffusion of this complex. The migration barrier is given by the highest barrier energy in the pathway. Note that, a more accurate representation could involve all the reactions e.g., $B_s - Si_i^{T_{1n}0} \Leftrightarrow B_i^{S0} \Leftrightarrow B_i^{H0}$. However, under most conditions, it is sufficient to use the simplified single reaction step.

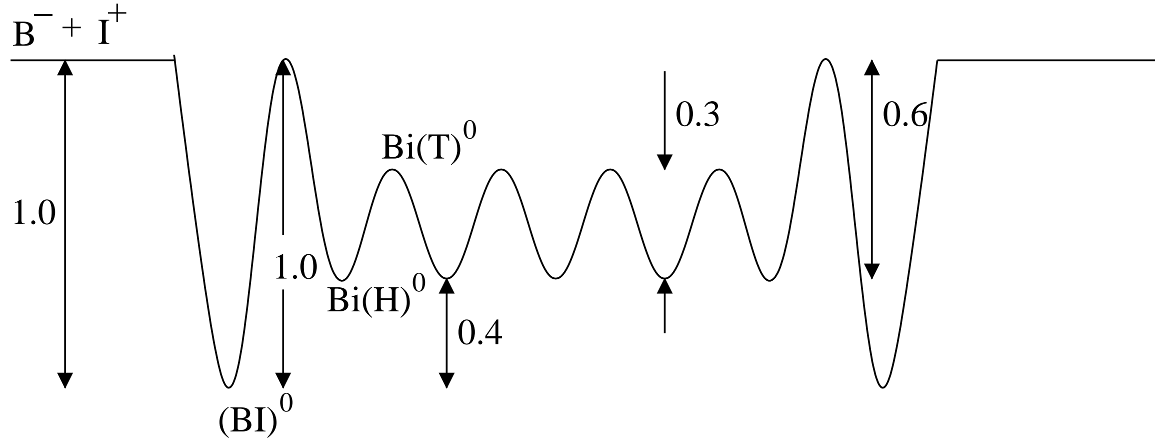

Figure 2.3: Diffusion path for boron interstitial for the kick-out mechanism as calculated by Zhu *et al.* [103].

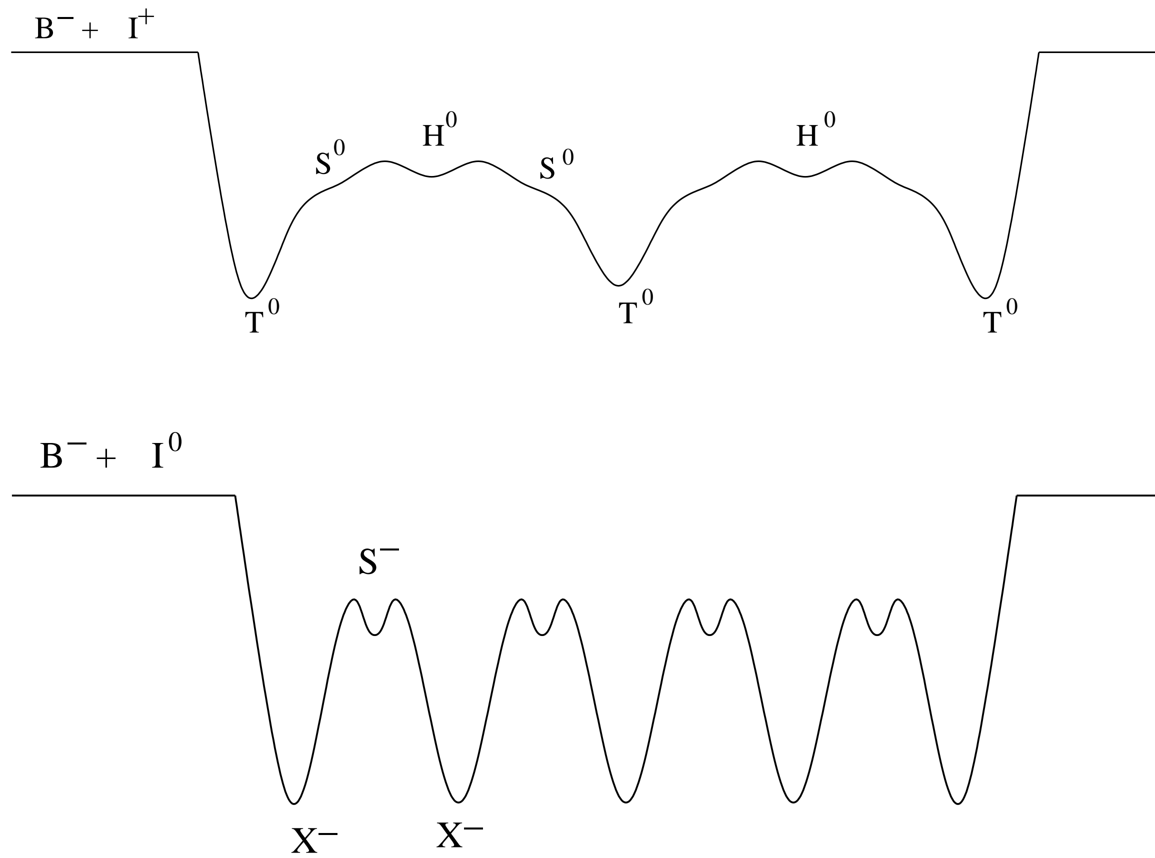

Figure 2.4: Comparison of the diffusion path for boron via the kick-out mechanism as calculated by Windl *et al.* [98] for (a) neutral (b) negative charge states.

2.2 Coupled diffusion

The current standard model for coupled dopant/defect diffusion is the pair diffusion model [33, 71, 72, 100, 101, 37]. For a system containing a single donor species, we first write down all the possible interactions. The pairing reactions are given as:

$$\mathrm{B}^i + \mathrm{I}^j \Leftrightarrow (\mathrm{BI})^{i+j}, \tag{2.12}$$

$$\mathrm{B}^i + \mathrm{V}^j \Leftrightarrow (\mathrm{BV})^{i+j}. \tag{2.13}$$

The parameters i and j represent the charge states of the defect or pair. The recombination and generation of Frenkel pairs can be described as:

$$\mathrm{I}^i + \mathrm{V}^j \Leftrightarrow (-i-j)e^-. \tag{2.14}$$

In addition, the pairs can interact directly with opposite type defects to produce a reaction which is equivalent to a pair dissociation followed by defect recombination.

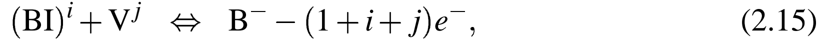

$$(\mathrm{BI})^i + \mathrm{V}^j \Leftrightarrow \mathrm{B}^- - (1+i+j)e^-, \tag{2.15}$$

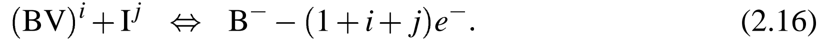

$$(\mathrm{BV})^i + \mathrm{I}^j \Leftrightarrow \mathrm{B}^- - (1+i+j)e^-. \tag{2.16}$$

We need to also consider ionization reactions or charge exchange reactions for each of the charged species.

Because electronic reactions are much faster than the atomic diffusion processes, we assume that all of the ionization reactions are near equilibrium. For example, the concentration of negatively charged interstitials is:

$$C_{\mathrm{I}^-} = \frac{\theta_{\mathrm{I}^-}}{\theta_{\mathrm{I}^0}} \exp\left(-\frac{E_{\mathrm{I}^-} - E_f}{kT}\right) C_{\mathrm{I}^0} = \frac{\theta_{\mathrm{I}^-}}{\theta_{\mathrm{I}^0}} \exp\left(\frac{E_f^i - E_{\mathrm{I}^-}}{kT}\right) C_{\mathrm{I}^0} \left(\frac{n}{n_i}\right) \tag{2.17}$$

where, E_f is the Fermi level with E_f^i being the intrinsic Fermi level and E_{I^-} is the energy level in the band gap. The terms n and n_i are the local and intrinsic carrier concentrations. The ratio of the number of configurations (θ) accounts for the fact that with unpaired electrons there is a spin degeneracy of 2 (+ or − spin). Thus, the concentrations of interstitials and BI pairs in various charge states are given by:

$$C_{\mathrm{I}^i} = K_{\mathrm{I}^i} C_{\mathrm{I}^0} (n_i/n)^i, \tag{2.18}$$

$$C_{(\mathrm{BI})^i} = K_{(\mathrm{BI})^i} C_{(\mathrm{BI})^-} (n_i/n)^{i+1} \tag{2.19}$$

where, K_{X} represents equilibrium coefficients.

It is necessary to determine the Fermi level in order to consider the behavior of charged species. It is possible to solve Poisson's equation in conjunction with continuity equations, but it has generally proven sufficient to simply assume local charge neutrality [37, 58], so

that the electron concentration can be calculated algebraically from the dopant distribution. In addition, we assume that charged defects and pairs when dilute can be ignored in determining the Fermi level. Since both defects and pairs can exist in multiple charge states (e.g., V^-, I^{++}), C_I, C_V, C_{BI} and C_{BV} have to be summed over all charge states. Thus, for example, the total interstitial concentration is

$$C_I = \sum_i C_{I^i} = \chi_I C_{I^0} = \sum_i \left[K_{I^i} \left(\frac{n_i}{n} \right)^i C_{I^0} \right], \tag{2.20}$$

where C_{I^0} is the concentration of neutral interstitials. Similarly, for pairs at equilibrium,

$$\begin{aligned} C_{BI} &= \sum_i C_{(BI)^i} = \pi_I C_B C_{I^0}, \\ C_{(BI)^-} &= K_{B^-/I^0} C_B C_{I^0} = K_{B^-/I^0} \frac{C_{BI}}{\pi_I}, \end{aligned} \tag{2.21}$$

where K_{B^-/I^0} is the equilibrium constant for the pairing of a neutral interstitial with a B substitutional atom. Since electronic exchange can occur before or after pairing and equilibrium concentration are independent of path, we can write,

$$K_{B^-/I^0} K_{(BI)^i} = K_{I^i} K_{B^-/I^i}. \tag{2.22}$$

Thus we can write,

$$\begin{aligned} \pi_I &= K_{B^-/I^0} \left[1 + K_{(BI)^0} \left(\frac{p}{n_i} \right) + K_{(BI)^{--}} \left(\frac{n}{n_i} \right) \right] \\ &= K_{B^-/I^0} + K_{B^-/I^+} K_{I^+} \left(\frac{p}{n_i} \right) + K_{B^-/I^-} K_{I^-} \left(\frac{n}{n_i} \right) \end{aligned} \tag{2.23}$$

Note that for simplicity, we have left off interaction with doubly charged defects in these equations. Boron being an accepter, K_{B^-/I^-} is expected to be small. This results in the following diffusion/reaction equations [43]:

$$\begin{aligned} \frac{\partial C_B}{\partial t} &= -R_{B+I} - R_{B+V} + R_{BI+V} + R_{BV+I} + 2R_{BI+BV} \\ \frac{\partial C_{BI}}{\partial t} &= -\vec{\nabla} \vec{J}_{BI} + R_{B+I} - R_{BI+V} - R_{BI+BV} \\ \frac{\partial C_{BV}}{\partial t} &= -\vec{\nabla} \vec{J}_{BV} + R_{B+V} - R_{BV+I} - R_{BI+BV} \\ \frac{\partial C_I}{\partial t} &= -\vec{\nabla} \vec{J}_I - R_{B+I} - R_{I+V} \\ \frac{\partial C_V}{\partial t} &= -\vec{\nabla} \vec{J}_V - R_{B+I} - R_{I+V} \end{aligned} \tag{2.24}$$

J_{X} represents the flux of species X and $R_{\mathrm{X+Y}}$ represents the net rate per unit volume of the reaction of species X and Y (e.g., $R_{\mathrm{B+I}}$ represents the net forward rate of the kick-out reaction given by Eq. 2.7). This model is commonly referred to as a "five stream model" based on the number of continuity equations for a single dopant. Each additional dopant adds three additional equations with corresponding flux and reaction terms added to the point defect equations.

Note that due to the charge of ions, the continuity equation will not only have a diffusion component ($\vec{J}^{\mathrm{diff}}$), but also a drift component ($\vec{J}^{\mathrm{drift}}$). The drift terms arise because the charged species can also move because of forces of the electric field, created by the gradient of electron concentration in the substrate. The total flux of point defects and pairs will be equal to the sum of fluxes of each charge state i:

$$\vec{J}_{(\mathrm{BI})^i} = \vec{J}^{\mathrm{diff}}_{(\mathrm{BI})^i} + \vec{J}^{\mathrm{drift}}_{(\mathrm{BI})^i} \tag{2.25}$$

Boron being an acceptor, we will expand in terms of the negative defect pair $(\mathrm{BI})^-$. Thus the diffusion term is:

$$\begin{aligned}
\vec{J}^{\mathrm{diff}}_{(\mathrm{BI})^i} &= -D_{(\mathrm{BI})^i}\vec{\nabla}C_{(\mathrm{BI})^i} \qquad (2.26)\\
&= -D_{(\mathrm{BI})^i}\vec{\nabla}\left[K_{(\mathrm{BI})^i}C_{(\mathrm{BI})^-}(p/n_i)^{i+1}\right]\\
&= -D_{(\mathrm{BI})^i}K_{(\mathrm{BI})^i}\vec{\nabla}\left[C_{(\mathrm{BI})^-}(p/n_i)^{i+1}\right]\\
&= -D_{(\mathrm{BI})^i}K_{(\mathrm{BI})^i}\left[(p/n_i)^{i+1}\vec{\nabla}C_{(\mathrm{BI})^-} + (i+1)C_{(\mathrm{BI})^-}(p/n_i)^i\vec{\nabla}(p/n_i)\right].
\end{aligned}$$

The drift term becomes:

$$\begin{aligned}
\vec{J}^{\mathrm{drift}}_{(\mathrm{BI})^i} &= \mu_{(\mathrm{BI})^i}iq\vec{\mathcal{E}}C_{(\mathrm{BI})^i}\\
&= D_{(\mathrm{BI})^i}(q/kT)i\vec{\mathcal{E}}C_{(\mathrm{BI})^i},
\end{aligned} \tag{2.27}$$

where $\mu = D/kT$ is the mobility according to the Einstein relationship and $\vec{\mathcal{E}}$ is the electric field vector. The electric field can be calculated from the gradient of the potential, which in turn can be found from the local carrier concentration, given by a Boltzmann distribution (Ψ denotes the intrinsic potential):

$$n = n_i \exp\left(\frac{\Psi}{kT/q}\right), \tag{2.28}$$

or Fermi Dirac distribution.

$$\begin{aligned}
\vec{\mathcal{E}} &= -\vec{\nabla}\Psi\\
&= -\vec{\nabla}\left[kT/q\ln(n/n_i)\right]\\
&= \vec{\nabla}\left[kT/q\ln(p/n_i)\right]
\end{aligned} \tag{2.29}$$

$$
\begin{aligned}
\vec{J}^{\text{drift}}_{(\text{BI})^i} &= iD_{(\text{BI})^i}C_{(\text{BI})^i}\vec{\nabla}\ln(p/n_i) \\
&= iD_{(\text{BI})^i}\left[K_{(\text{BI})^i}C_{(\text{BI})^-}(p/n_i)^{i+1}\right](n_i/p)\vec{\nabla}(p/n_i) \\
&= iD_{(\text{BI})^i}K_{(\text{BI})^i}C_{(\text{BI})^-}(p/n_i)^i\vec{\nabla}(p/n_i). \qquad (2.30)
\end{aligned}
$$

Adding the diffusion and drift terms we get:

$$
\begin{aligned}
\vec{J}_{\text{BI}^i} &= -D_{(\text{BI})^i}K_{(\text{BI})^i}(p/n_i)^{i+1}\left[\vec{\nabla}C_{(\text{BI})^-} + C_{(\text{BI})^-}\vec{\nabla}\ln(p/n_i)\right] \qquad (2.31) \\
&= -D_{(\text{BI})^i}K_{(\text{BI})^i}K_{\text{B}^-/\text{I}^0}(p/n_i)^{i+1}\left[\vec{\nabla}\left(\frac{C_{\text{BI}}}{\pi_{\text{I}}}\right) + \frac{C_{\text{BI}}}{\pi_{\text{I}}}\vec{\nabla}\ln\left(\frac{p}{n_i}\right)\right].
\end{aligned}
$$

Summing over all the charge states, we get:

$$
\begin{aligned}
\vec{J}_{\text{BI}} &= \sum_{i=-1}^{+1}\vec{J}_{\text{BI}^i} \qquad (2.32) \\
&= -\frac{(D_{\text{B}}^{\text{I}^0} + D_{\text{B}}^{\text{I}^+}(p/n_i) + D_{\text{B}}^{\text{I}^-}(n/n_i))}{C^*_{\text{I}^0}}\left[\vec{\nabla}\left(\frac{C_{\text{BI}}}{\pi_{\text{I}}}\right) + \frac{C_{\text{BI}}}{\pi_{\text{I}}}\vec{\nabla}\ln\left(\frac{p}{n_i}\right)\right].
\end{aligned}
$$

The separate components of diffusivities such as $D_{\text{B}}^{\text{I}^+}$ stand for diffusivity of boron due to pairing with interstitials in a given charge state (I^+ or $(\text{BI})^0$ in this case). From oxidation and nitridation experiments, it is known that boron diffuses primarily by interstitials [54] (i.e $f_I^{\text{intr}} \sim 1$). It is also necessary to make an assumption on the variation of f_I for each charge state. Assuming, f_I^{intr} is independent of Fermi level,

$$
f_I^{\text{intr}} = \frac{D_{\text{B}}^{\text{I}^0} + D_{\text{B}}^{\text{I}^+}}{D_{\text{B}}^0 + D_{\text{B}}^+} \qquad (2.33)
$$

It is also necessary to make assumption on the ratio $f_{\text{I}}^0/f_{\text{I}}^+$ or $D_{\text{B}}^{I^0}/D_{\text{B}}^{I^+}$ and we assume they are equal. Hence,

$$
f_I^{\text{intr}} = \frac{D_{\text{B}}^{\text{I}^0}}{D_{\text{B}}^{\text{I}^0} + D_{\text{B}}^{\text{V}^0}} = \frac{D_{\text{B}}^{\text{I}^+}}{D_{\text{B}}^{\text{I}^+} + D_{\text{B}}^{\text{V}^+}}. \qquad (2.34)
$$

we can now calculate $D_{\text{B}}^{\text{I}^+}$ from experimental boron diffusivity data. However, to calculate π_{I} it is necessary to assume that the diffusivity of boron interstitial pairs is independent of their charge state, since experiments yield the ratio:

$$
\frac{D_{\text{B}}^+}{D_{\text{B}}^0} = \frac{D_{(\text{BI})^0}}{D_{(\text{BI})^-}}\frac{K_{\text{I}^+}K_{\text{B}^-/\text{I}^+}}{K_{\text{I}^0}K_{\text{B}^-/\text{I}^0}}. \qquad (2.35)
$$

The dopant vacancy pair flux is calculated similarly,

$$\begin{aligned}
\vec{J}_{\mathrm{BV}} &= -\frac{D_{\mathrm{B}}^{\mathrm{V}}}{C_{\mathrm{V}^0}^*}\left[\vec{\nabla}\left(\frac{C_{\mathrm{BV}}}{\pi_{\mathrm{V}}}\right)+\frac{C_{\mathrm{BV}}}{\pi_{\mathrm{V}}}\vec{\nabla}\ln\left(\frac{p}{n_i}\right)\right], \\
D_{\mathrm{B}}^{\mathrm{V}} &= D_{\mathrm{B}}^{\mathrm{V}^0}+D_{\mathrm{B}}^{\mathrm{V}^+}\left(\frac{p}{n_i}\right)+D_{\mathrm{B}}^{\mathrm{V}^-}\left(\frac{n}{n_i}\right) \\
\pi_{\mathrm{V}} &= K_{\mathrm{B}^-/\mathrm{V}^0}+K_{\mathrm{B}^-/\mathrm{V}^+}K_{\mathrm{V}^+}\left(\frac{p}{n_i}\right)+K_{\mathrm{B}^-/\mathrm{V}^-}K_{\mathrm{V}^-}\left(\frac{n}{n_i}\right).
\end{aligned} \tag{2.36}$$

The total flux of interstitials in each of the charge states can be written in terms of the gradient in the neutral concentration and the electron concentration:

$$\vec{J}_{\mathrm{I}^i} = -D_{\mathrm{I}^i}\left(\vec{\nabla}C_{\mathrm{I}^i}-\frac{iq\vec{\mathcal{E}}}{kT}C_{\mathrm{I}^i}\right) = -D_{\mathrm{I}^i}K_{\mathrm{I}^i}\left(\frac{n_i}{n}\right)^i\vec{\nabla}C_{\mathrm{I}^0}, \tag{2.37}$$

where D_{I^i} represents the diffusivity of interstitials of charge state i. Thus the total interstitial flux is:

$$\vec{J}_{\mathrm{I}} = \sum_i \vec{J}_{\mathrm{I}^i} = -D_{\mathrm{I}^0}\chi_{\mathrm{I}}\vec{\nabla}C_{\mathrm{I}^0} \tag{2.38}$$

where,

$$\chi_{\mathrm{I}} = 1+K_{\mathrm{I}^+}\left(\frac{p}{n_i}\right)+K_{\mathrm{I}^-}\left(\frac{n}{n_i}\right) \tag{2.39}$$

Note again that, due to lack of better experimental evidence it is assumed that $D_{\mathrm{I}^i} = D_{\mathrm{I}^0}$. This assumption is made throughout this work. Similarly we can write for vacancies,

$$\begin{aligned}
\vec{J}_{\mathrm{V}} &= -D_{\mathrm{V}^0}\chi_{\mathrm{V}}\vec{\nabla}C_{\mathrm{V}^0} \\
\chi_{\mathrm{V}} &= 1+K_{\mathrm{V}^+}\left(\frac{p}{n_i}\right)+K_{\mathrm{V}^-}\left(\frac{n}{n_i}\right)
\end{aligned} \tag{2.40}$$

The expressions for the net rate of pairing and recombination reactions are also summed over all the charge states. Noting the definitions of $\chi_{\mathrm{I}},\chi_{\mathrm{V}}$ and $\pi_{\mathrm{I}},\pi_{\mathrm{V}}$ from Eq. 2.20 and 2.21, we can write down the net reaction rates of the pairing and recombination reactions as:

$$\begin{aligned}
R_{\mathrm{B+I}} &= k_{\mathrm{B/I}}[C_{\mathrm{B}}C_{\mathrm{I}}-\frac{\chi_{\mathrm{I}}}{\pi_{\mathrm{I}}}C_{\mathrm{BI}}] \\
R_{\mathrm{B+V}} &= k_{\mathrm{B/V}}[C_{\mathrm{B}}C_{\mathrm{V}}-\frac{\chi_{\mathrm{I}}}{\pi_{\mathrm{I}}}C_{\mathrm{BV}}] \\
R_{\mathrm{BI+V}} &= k_{\mathrm{BI/V}}(C_{\mathrm{BI}}C_{\mathrm{V}}-C_{\mathrm{I}^0}^*C_{\mathrm{V}^0}^*\pi_I\chi_V C_{\mathrm{B}}) \\
R_{\mathrm{BV+I}} &= k_{\mathrm{BV/I}}(C_{\mathrm{BV}}C_{\mathrm{I}}-C_{\mathrm{I}^0}^*C_{\mathrm{V}^0}^*\pi_V\chi_I C_{\mathrm{B}}) \\
R_{\mathrm{BV+BI}} &= k_{\mathrm{BV/BI}}(C_{\mathrm{BV}}C_{\mathrm{BI}}-C_{\mathrm{I}^0}^*C_{\mathrm{V}^0}^*\pi_I\pi_V C_{\mathrm{B}}^2)
\end{aligned} \tag{2.41}$$

Note that the kinetic forward reaction rate $k_{X/Y}$ for the reactants with diffusivities D_X and D_Y is assumed to be diffusion limited and thus equivalent to that derived in Eq. 2.5:

$$k_{X/Y} = 4\pi a_0 (D_X + D_Y) \tag{2.42}$$

When other species such as clusters or extended defects are also present additional continuity equations must be added and additional terms representing the formation/dissolution of these species must be included on the right hand sides of Eqs. 2.24. Under most conditions (although not during the early stages of ion implant annealing when the concentration of pairs is not dilute), the dopant/defect pairing reactions (e.g., $B + I \Leftrightarrow BI$) are fast enough to maintain the pair concentration near local equilibrium with the concentrations of isolated dopants and defects (e.g., $C_{(BI)^i} \cong K_{B^-/I^i} K_{I^i} C_{B^-} C_{I^0} (p/n_i)^{i+1}$).

Under these conditions, the five stream model can be reduced to three continuity equations (often referred to as the "fully-coupled" model) [33]. Though this model is used in most Process Simulators, it is not always correct to use this approach. To understand this case better, we can calculate the time it takes for the pair to reach equilibrium or the distance it moves as a pair before dissociating to a substitutional site and an self-interstitial. This is equivalent to looking at time scales smaller than the average life time (τ_{BI}) of a pair. In other words, most of the atoms have undergone only one migration event in times less than τ_{BI}. The life time of a pair is the reciprocal of the reverse reaction rate $\tau_{BI} = 1/k_r$. The distance which the pair travels in this time is on average

$$\lambda = \sqrt{D_{BI}\tau_{BI}} = \sqrt{\frac{D_B}{4\pi a D_I C_I^*}} \tag{2.43}$$

Interestingly, the pair diffusion length can be estimated in terms of macroscopic quantities. The calculated value at 800°C is 3.7 nm and compares favorably to the experimental value of 5 nm [25]. However at 600°C the calculated value is 20 nm which is twice the experimental value. It should be noted that the experimental determination was obtained monitoring the movement of a marker layer in a structure grown MBE which generally leads to higher levels of carbon. This could result in a lower value of λ. The value of λ thus calculated is also comparable to the junction depths of ultra low energy implants modeled in Chap. 5. Hence the "fully coupled" model is not used for any of the simulations in this thesis and instead the more physical "five-stream" (Eq. 2.24) model is used. Some instances when the five-stream model may not give reliable answers would involve very low dopant concentrations (e.g., a few atoms) where it would be questionable to use a continuum approach. Similarly, it may be inappropriate to use a continuum approach to model the initial recombination of point defects where the initial correlation between interstitial and vacancy cascades is expected to be important [15].

Under intrinsic conditions near equilibrium with no spatial variation in point defect concentrations, the effective diffusivity of a dopant can be shown to be (calculate from

Eq. 2.32 and 2.36) [37]:

$$\frac{D_{\mathrm{B}}}{D_{\mathrm{B}}^{*}} = f_{\mathrm{I}}^{\mathrm{intr}} \frac{C_{\mathrm{I}}}{C_{\mathrm{I}}^{*}} + (1 - f_{\mathrm{I}}^{\mathrm{intr}}) \frac{C_{\mathrm{V}}}{C_{\mathrm{V}}^{*}} \tag{2.44}$$

where, the '*' denotes equilibrium values. From Eq. 2.44 it is clear that dopant diffusivities can be altered by changes in point defect concentrations. Therefore, to understand dopant diffusion in silicon, it is necessary to understand and model how different process interact and thus govern point defect supersaturations. Hence one of the key parameters for modeling these systems are the parameters of the intrinsic point defects.

2.3 Point defect properties

The properties of point defects clearly play a central role in controlling diffusion processes, especially during TED. Because the diffusion of metal atoms (as well as dopants) depends quite directly on total point defect fluxes, values for the $D_{\mathrm{I}}C_{\mathrm{I}}^{*}$ and $D_{\mathrm{V}}C_{\mathrm{V}}^{*}$ products have become broadly accepted [12, 37, 49, 51, 74, 95, 109]. However, there continue to exist substantial disagreements over the magnitude of the diffusivities and equilibrium concentrations which go to make up these products.

Mainly two types of experiments give us information about point defects. Analysis of diffusion profiles for metals such as Au, Pt and Zn, and study of dopant diffusion under point defect injection conditions such as oxidation and nitridation. However, the latter method has provided a wealth of data about dopant diffusion mechanisms and much less on the intrinsic point defects involved. The most widely used estimates of vacancy parameters come from metal diffusion experiments, but even here the issue of vacancy diffusivity is not clear. Most of the metal diffusion experiments predict a relatively low vacancy diffusivity [12, 109]. In contrast, *ab-initio* [77, 103] and tight-binding MD calculations [94] find that formation energies for vacancies are on the same order or larger than that of interstitials and that the migration energy for vacancies is smaller than that of interstitials. This issue has been recently been complicated further as carbon has been shown to act as an interstitial trap and hence reduces the effective interstitial diffusivity if present in large amounts [91]. Until recently, the accepted view within the TCAD community had been that vacancies are relatively slow diffusers compared to interstitials, but are present in much larger numbers. This conclusion was largely based on analysis of metal diffusion experiments [12, 75, 107].

2.4 Metal diffusion

Upon reexamining the analysis of metal diffusion experiments which gave large equilibrium concentrations and low diffusivities for vacancies, it can be observed that in order to simplify the analysis, the original work [12, 107] generally neglected bulk recombination and made a number of assumptions about the dominant mechanisms controlling behavior at different temperatures and time scales. Hence, to resolve this issue, it was necessary to model metal diffusion experiments more rigorously.

The metals Au, Pt and Zn diffuse mainly via the kick-out and Frank-Turnbull (or dissociative mechanism) [12, 70, 108]. This leads to the reactions,

$$\mathrm{M}_s + \mathrm{I} \Leftrightarrow \mathrm{M}_{\mathrm{i}}, \tag{2.45}$$

$$M_s \Leftrightarrow M_i + V, \tag{2.46}$$

where M_i and M_s represent interstitial and substitutional metal as well as their concentrations. A third reaction that needs to be considered is the bimolecular recombination between interstitials and vacancies,

$$I + V \Leftrightarrow \phi. \tag{2.47}$$

Assuming that substitutional metal is immobile we can now write the full set of equations that need to be solved similar to that discussed in Section 2.2.

It is also necessary to specify the initial boundary conditions. For point defects, we assume that the Si/metal surface is an infinite source and sink for point defects. Hence, the concentrations of interstitials and vacancies are fixed at their equilibrium values (C_I^* and C_V^*) at all times during the diffusion process. The initial interstitial concentration is taken to be equal to C_I^*. However, there is some debate over the initial vacancy concentration since previous work on metal diffusion has used different initial concentrations of vacancies [12, 109]. We discuss this issue further in the subsequent sections. For the metals, the initial concentration in the silicon is considered negligible ($< 10^8 \mathrm{cm}^{-3}$). The surface concentration of interstitial metal is set to its solubility.

2.4.1 Zinc diffusion

Since extensive zinc diffusion data is available for both heavily dislocated and defect-free material [12, 13], we focus on this metal for much of our analysis. In the experiments, Bracht *et al.* [12] first equilibrated the samples at diffusion temperatures ranging from 870°C to 1208°C and then introduced zinc, which diffused in from both surfaces. Dislocations act as sources and sinks for point defects. Hence, in heavily dislocated material, point defect concentrations remain near equilibrium ($C_I = C_I^*$, $C_V = C_V^*$) and diffusion is independent of the intrinsic point defect properties.

We use the metal properties found by Bracht *et al.* [13] for diffusion in dislocated silicon in our modeling of the defect-free material. For consistency, instead of fitting single temperatures, all the curves were simultaneously fit using temperature activated parameters. Bracht *et al.* [12] extracted a high value for C_V^* from this data, but required an initial vacancy concentration much less than equilibrium ($C_V(t=0) \leq 10^{-4} C_V^*$). The simulated and measured profiles using the parameters extracted by Bracht *et al.* [12] are shown in Figs. 2.5 and 2.6. also unable to fit the data. However using the model described above and avoiding some of the assumptions made by Bracht, we were able to obtain a similar fit to the observed data using $C_V(t=0) = C_V^*$ (as expected given equilibrium) and a much lower value of C_V^* (Figs. 2.7 and 2.8). The extracted C_V^* has the further advantage of being much closer to theoretical predictions [49].

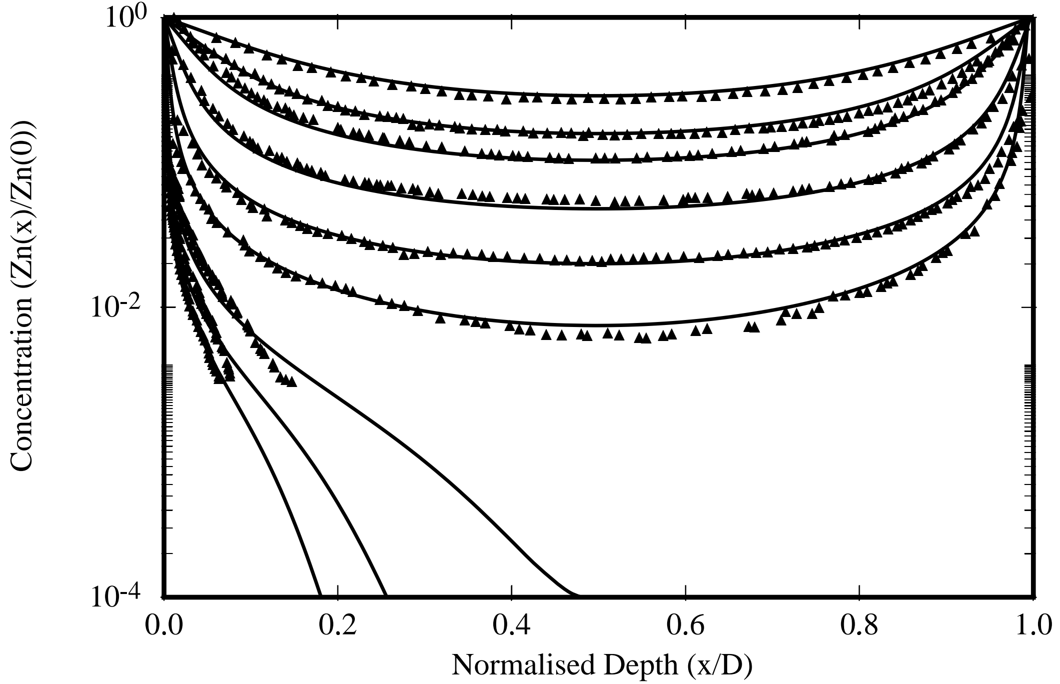

Figure 2.5: Normalized zinc diffusion profiles at 870°C into defect-free silicon and comparison to simulations using point defect parameters from Bracht *et al.* [12].

2.4.2 Platinum diffusion

Low temperature diffusion data exist for Pt as it diffuses faster than Zn or Au [66]. Platinum profiles are characterized by uniform bulk concentrations of the substitutional Pt which do not change with time, and at the lowest temperature an inverse U profile is seen in non-equilibrated samples [106]. The flat profiles have been attributed to the initial concentration of point defects and assuming the dominance of the dissociative reaction, Zimmermann *et al.* calculated a C_{V}^{*} value similar to that of Bracht *et al.* [12]. The inverse U profiles were explained by an initial super-saturation of vacancies, leading to a metal concentration in the bulk greater than its solid solubility. However, we find this behavior can also be explained by a carbon clustering model as discussed below and shown in Figs. 2.9 and 2.10.

It has been reported based on MBE grown samples with elevated carbon concentrations that carbon acts as an interstitial trap [91]. Carbon in silicon can be modeled [49] based on diffusion as an interstitial,

$$\mathrm{C}_s + \mathrm{I} \Leftrightarrow \mathrm{C}_i, \tag{2.48}$$

plus reaction of interstitial carbon with substitutional carbon to form an immobile complex

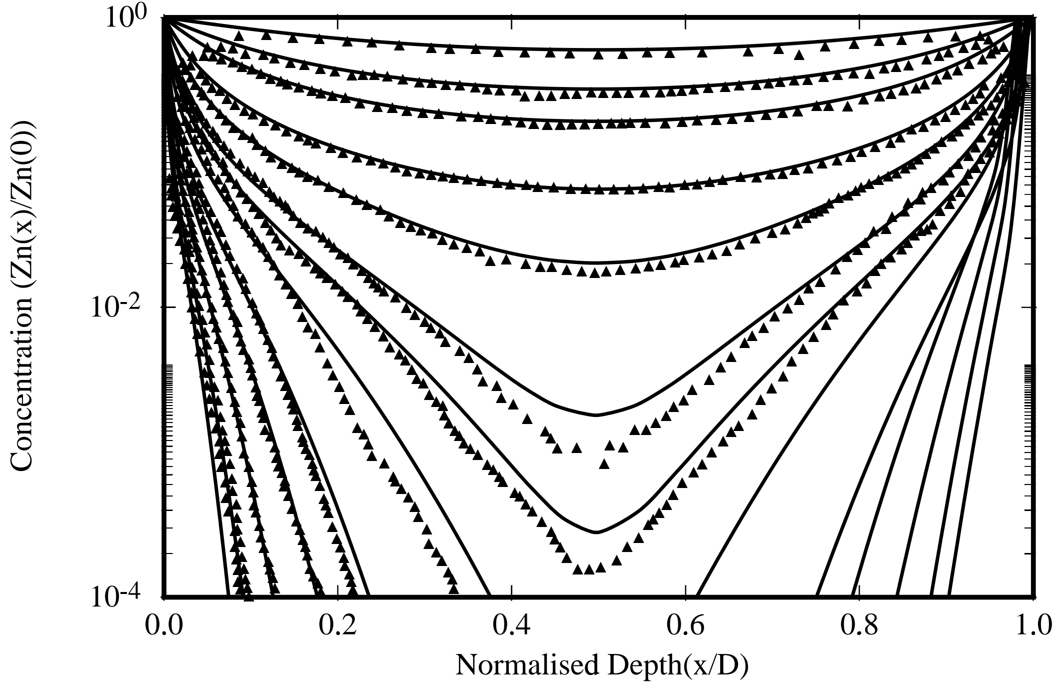

Figure 2.6: Normalized zinc diffusion profiles at 1208°C into defect-free silicon and comparison to simulations using point defect parameters from Bracht *et al.* [12].

C_2I,

$$C_i + C_s \Leftrightarrow C_2I. \tag{2.49}$$

Since carbon clusters with an interstitial, each cluster formation annihilates an interstitial or generates a vacancy. If the initial carbon cluster concentration is less than its equilibrium value, the formation of carbon clusters leads to an under-saturation of interstitials (or a corresponding super-saturation of vacancies) which leads to the inverse U profile. This is possible during FZ crystal growth, if we assume that the material is quenched from a high temperature at which the clusters are unstable. It should be noted that the flat profile of platinum in the bulk is expected even if the samples were equilibrated before the in-diffusion [104], although the bulk Pt concentration is lower in this case. To check our analysis, the same carbon model and parameters were used for simulations of zinc diffusion. As seen in Fig. 2.11, we find that at the higher temperatures used for zinc, moderate carbon levels carbon do not produce a significant change in the profiles.

Shown in Fig. 2.12 [16] is comparison of extracted values of $D_V C_V^*$, $D_I C_I^*$. From this analysis, we obtain $C_V^* \sim C_I^*$ as shown in Fig. 2.13 [16], four orders of magnitude smaller than originally calculated and much closer to the results of atomistic calculations. Fig. 2.14 shows the change in mean squared error as each of the parameters is changed

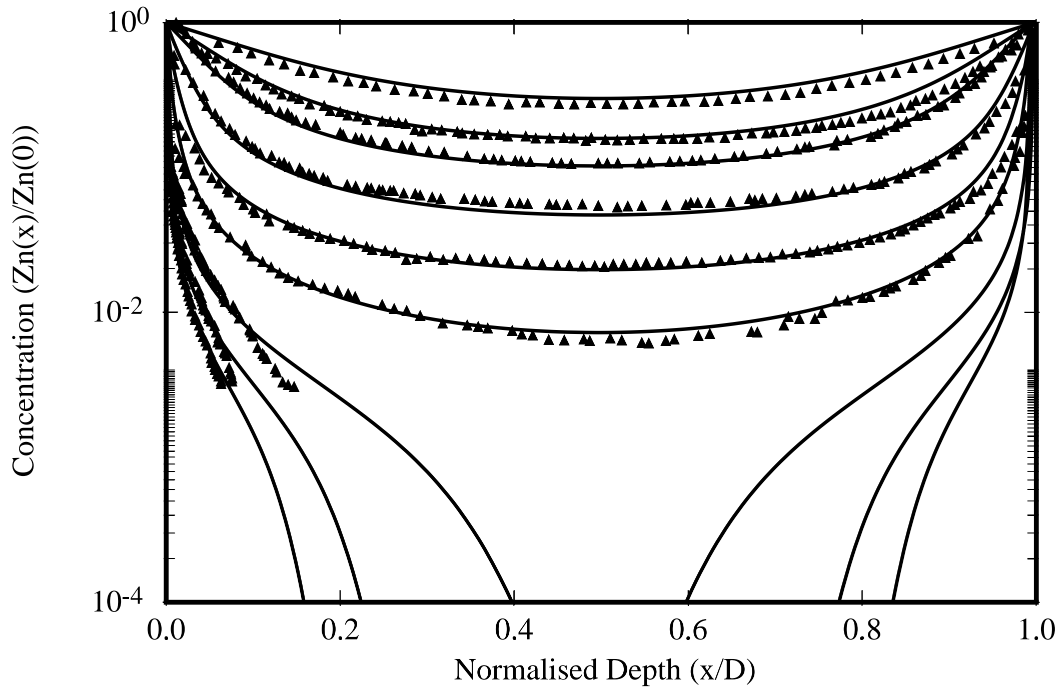

Figure 2.7: Normalized zinc diffusion profiles at 870°C into defect-free silicon and comparison to simulations using point defect parameters obtained in this work.

from its optimum value. Thus we can conclude that the $D_{\mathrm{I}}C_{\mathrm{I}}^*$ product is well characterized by the data and that it is possible to establish solid upper limits for $D_{\mathrm{V}}C_{\mathrm{V}}^*$ and C_{I}^*, but that C_{V}^* is not accurately determined by these experiments and only a relatively loose upper bound could be obtained.

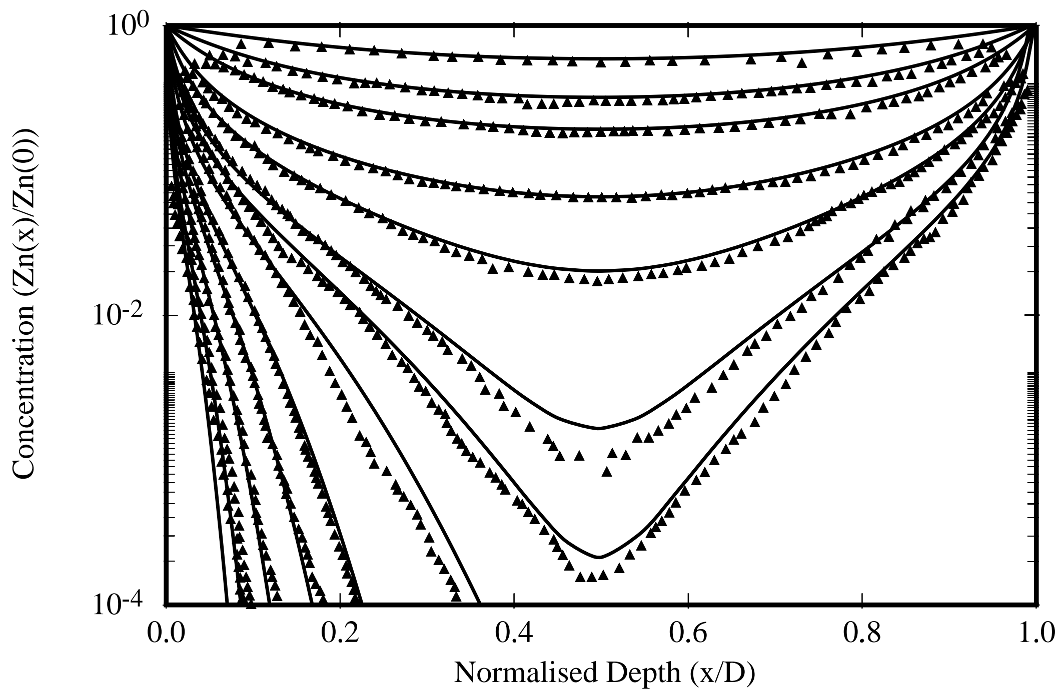

Figure 2.8: Normalized zinc diffusion profiles at 1208°C into defect-free silicon and comparison to simulations using point defect parameters obtained in this work.

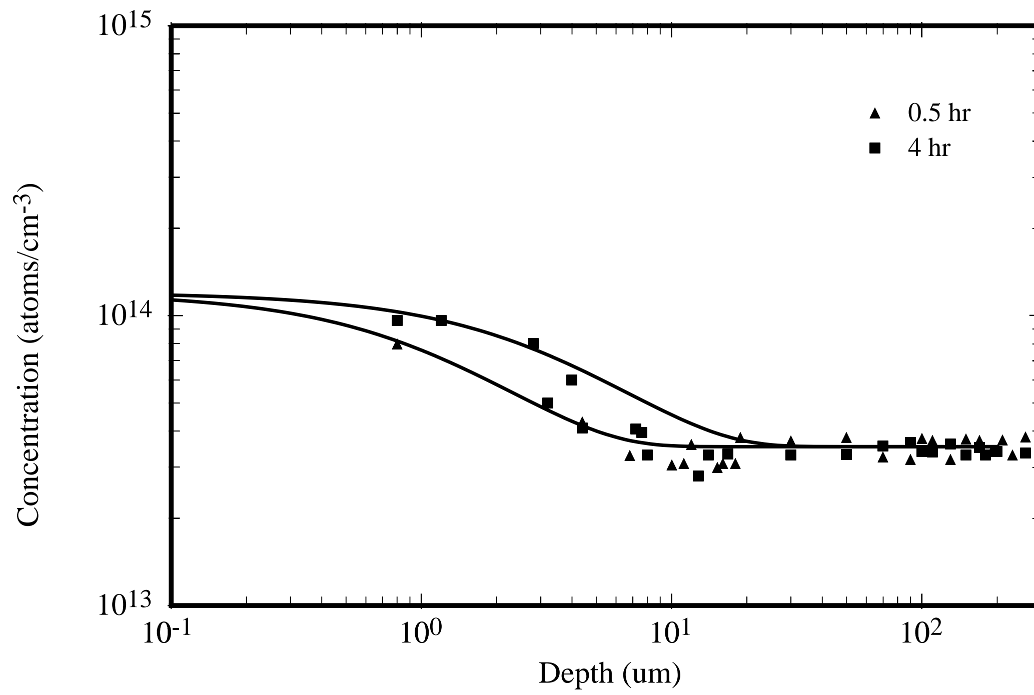

Figure 2.9: Measured and simulated platinum profiles at 770°C [105].

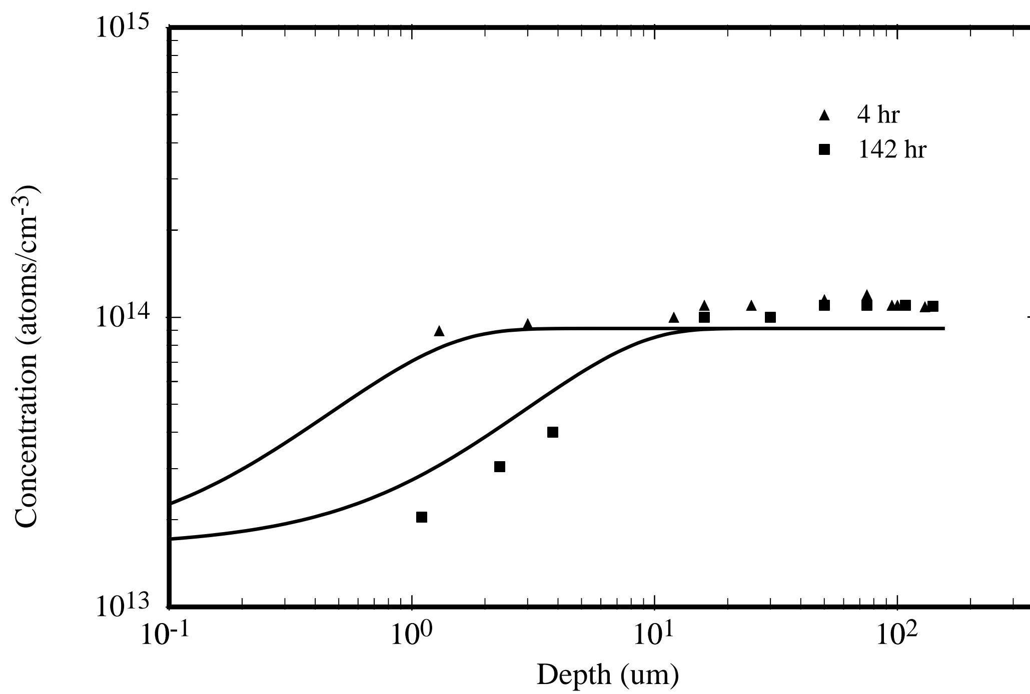

Figure 2.10: Measured and simulated platinum profiles at 700°C [106]. Note the uniform Pt concentration in bulk which is unchanged with time, and the inverse U profile.

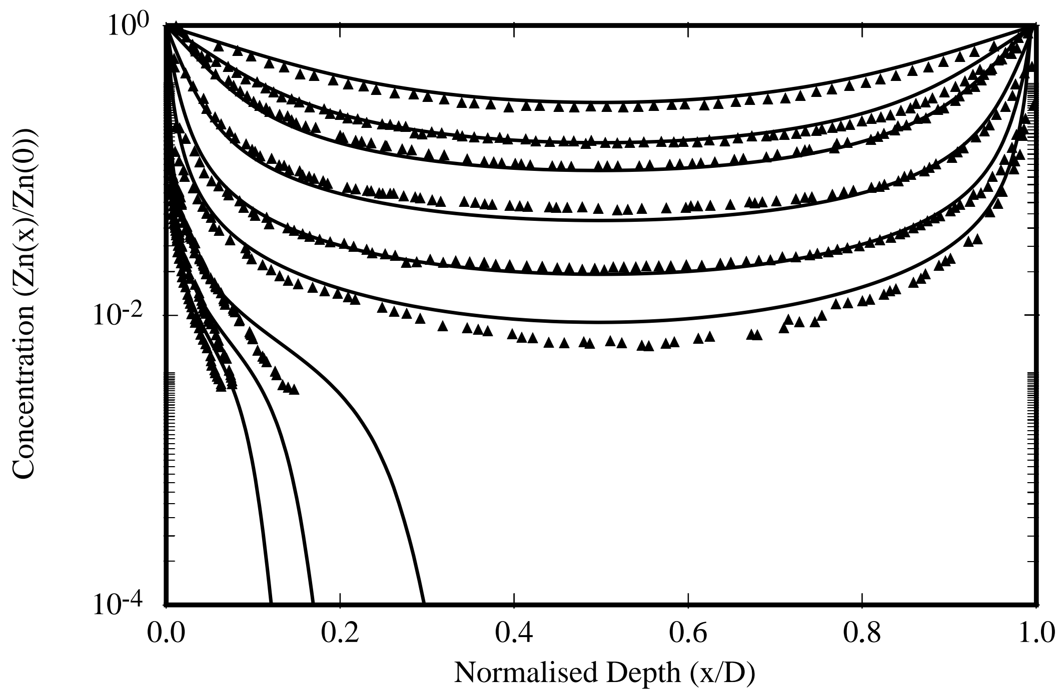

Figure 2.11: Effect of carbon on zinc diffusion at 870°C. Carbon has only a minor effect even at the lowest available diffusion temperature.

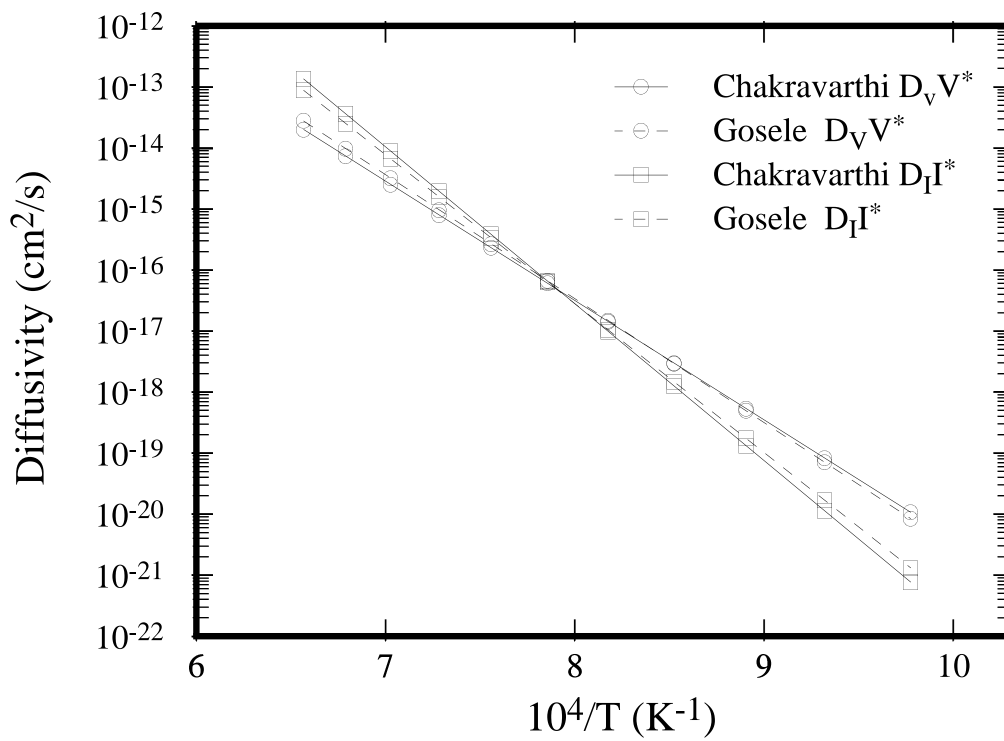

Figure 2.12: Extracted values of $D_V C_V^*/C_s$, $D_I C_I^*/C_s$ (C_s is the silicon lattice density) from fitting Zn diffusion data of Bracht *et al.* [12] and comparison to previous analysis based on metal diffusion [49].

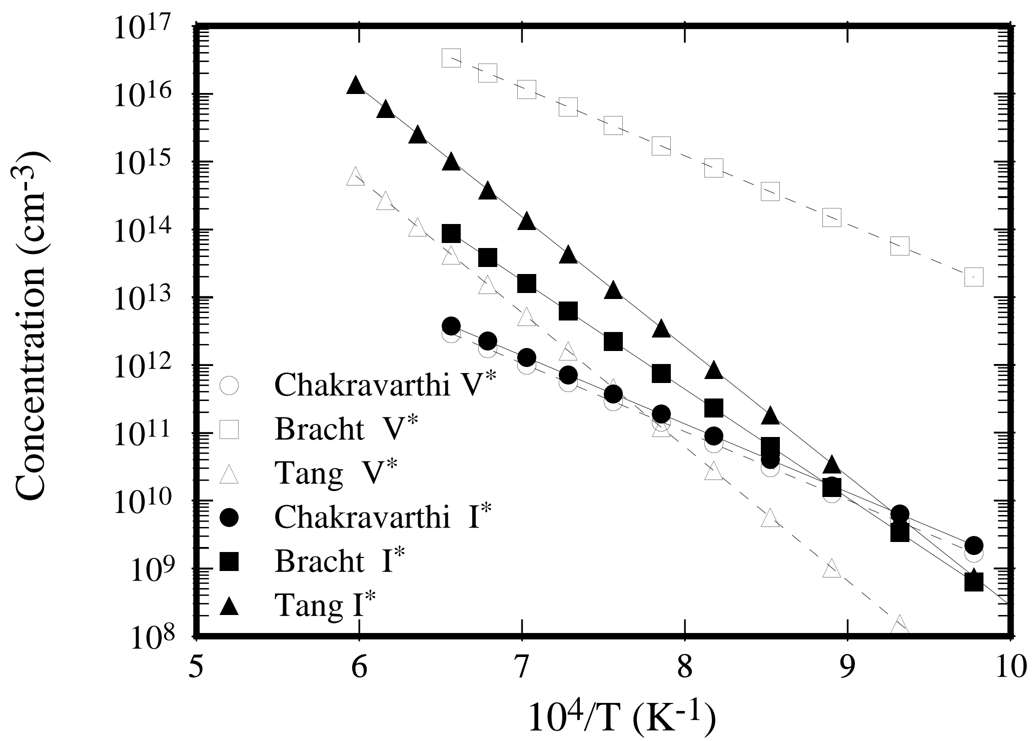

Figure 2.13: Extracted values of C_V^* and C_I^* from fitting Zn diffusion data of Bracht *et al.* [12] and comparison to previous analysis based on both metal diffusion and atomistic calculations [94].

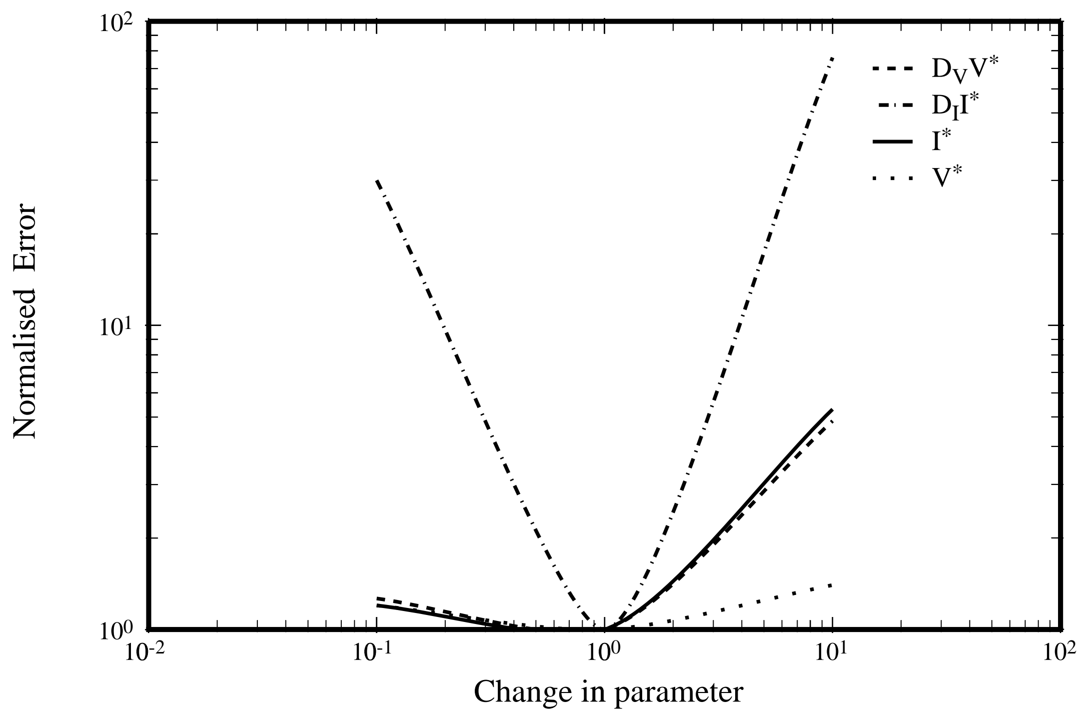

Figure 2.14: Effect of variation in a single point defect parameter and reoptimizing all the profiles. It can be seen that $D_\mathrm{I}C_\mathrm{I}^*$ is the most reliably extracted parameter and C_V^* is the least.

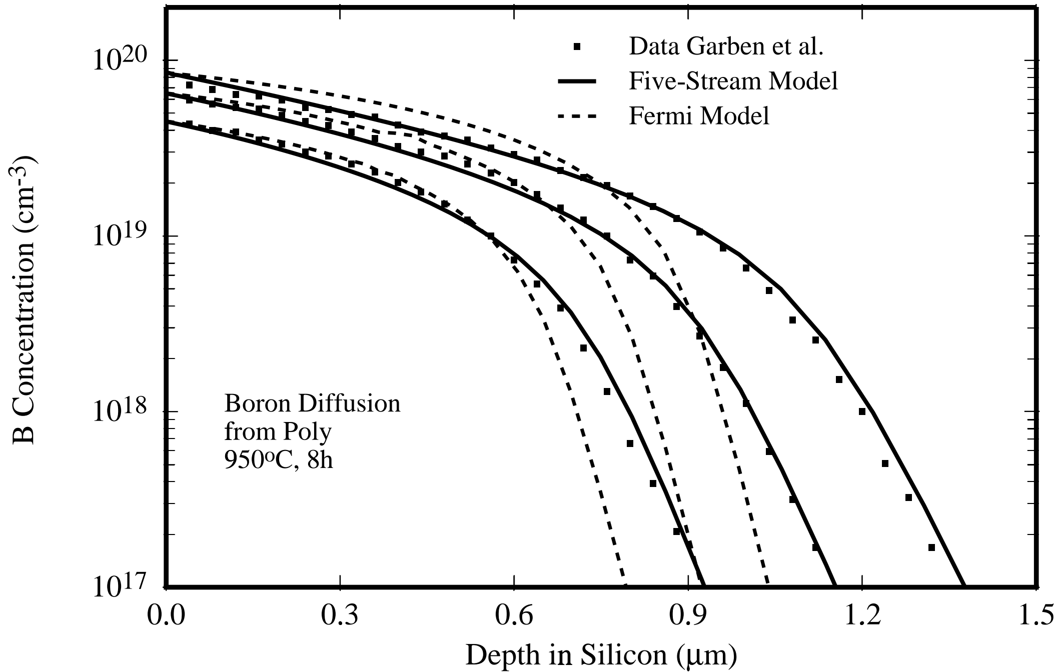

Figure 2.15: Boron diffusion from implanted polysilicon from Garben *et al.* [39] and comparison to prediction of coupled diffusion model. Also shown is prediction by Fermi model not considering point-defect mediated diffusion.

2.5 Boron indiffusion

Combining the knowledge gained from the previous sections, we can now simulate boron diffusion in silicon successfully. To demonstrate and verify our models and parameters we focus on the in-diffusion of boron. In these experiments, a boron source is deposited on the surface of silicon and the sample is annealed for various times and temperatures. Hence boron diffuses into silicon from a constant surface source. Fig. 2.15 shows such a simulation for a 950°C boron in-diffusion anneal from Garben *et al.* [39]. It is interesting to note that an increase in boron surface concentrations leads to larger fluxes of BI pairs into the substrate leading to larger tail enhancements (as shown in Fig. 2.16). This is the same coupled diffusion phenemenon which leads to phosphorus kink ans tail profiles [33].

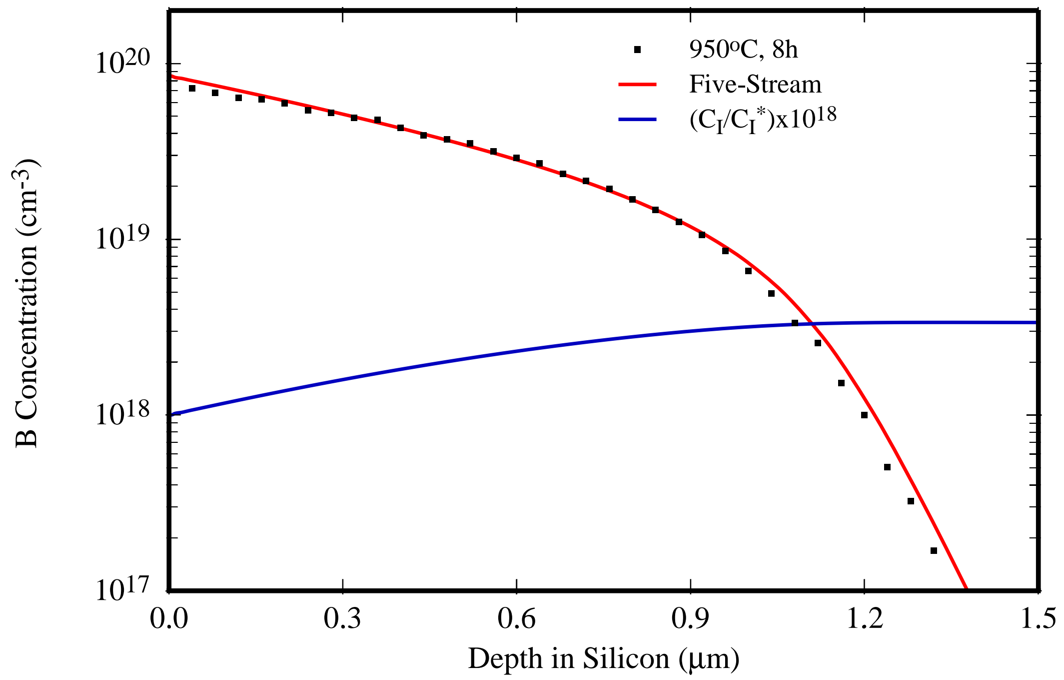

Figure 2.16: Boron indiffusion for the highest surface concentration, also plotted is $C_\mathrm{I}/C_\mathrm{I}^*$. Note that the tail diffusion is enhanced by a factor of about 3.

2.6 Summary

Thus, in this chapter we reviewed the diffusion of dopants particularly boron in silicon. We followed it by reviewing coupled diffusion models for dopant diffusion in silicon. Finally, in Section 2.4 we presented our analysis of metal diffusion experiments to re-evaluate point defect properties in silicon.

Chapter 3

Ion Implant Damage Evolution

In this chapter, we first review the different aspects of transient enhanced diffusion (TED). It is necessary to understand the different phenomena and decouple them to be able to successfully model TED. Later, in Section 3.6, we discuss our work on modeling the evolution of the initial implant cascade. Mainly we verify the validity of some of the common assumptions made for the initial conditions. These assumptions are used as a basis for our simulations in the rest of this work.

3.1 Initial damage

At first glance, the prediction of defect evolution after implantation might appear very difficult. Large numbers of point defects are created, and they can coalesce into various forms of extended defects. However, it is possible to make some simplifying assumptions. Looking at the damage created by the ion implantation process, we can see that the number of Frenkel pairs generated is much higher than the number of implanted ions (Fig. 3.1). In fact, the interstitial and vacancy curves are almost indistinguishable from each other, but there is a vacancy-rich region near the surface and an interstitial-rich region deeper in the substrate. This stems from the fact that the implantation drives some silicon atoms deeper into the substrate. Recombination of this cascade, however, would leave us with a net "$+1$" damage, where each incoming ion displaces one silicon atom, such that the net $I-V$ dose is equal to the implant dose. For light atoms such as boron, this separation between the net interstitial and vacancy profiles is minimal. Hence a "plus-one" model [46] has been very successful in predicting TED.

This picture may sound very simplified but has received strong experimental support. For sub-amorphizing implants, Chen *et al.* [22] showed that the amount of transient diffusion caused by a Si implant was independent of both dose and implant temperature. Since both factors affect the number of Frenkel pairs remaining after the implant, it supports the notion that the number of pairs created by implantation is not a primary variable in TED.

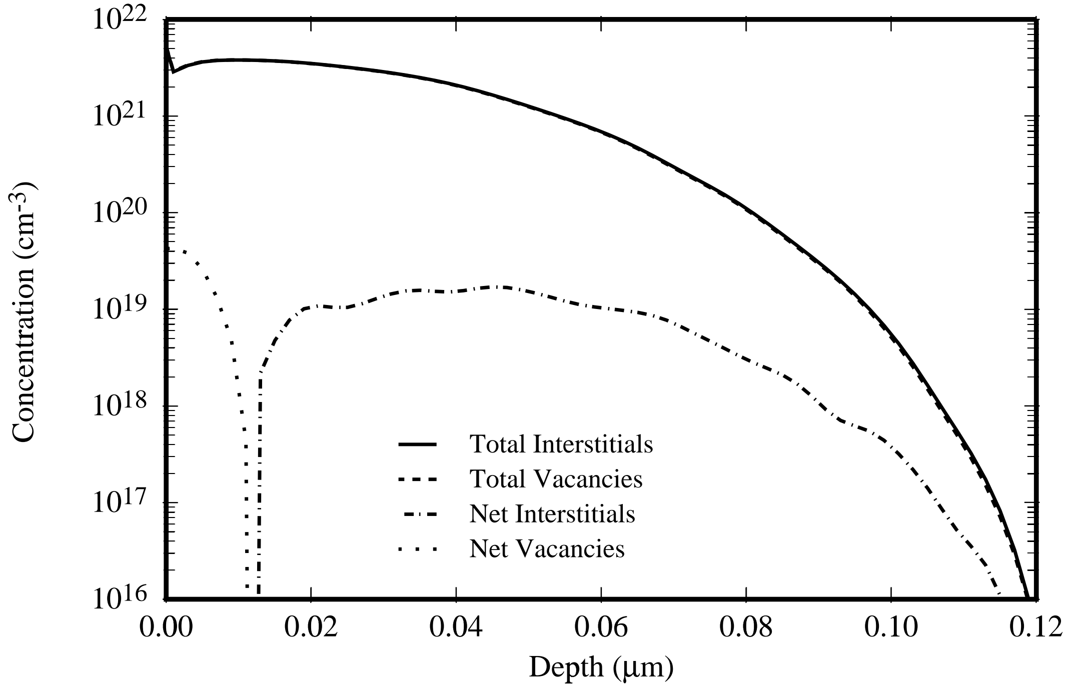

Figure 3.1: Total and net damage created by a 40 keV, $5 \times 10^{13}\,\mathrm{cm}^{-2}$ Si implant. Monte Carlo simulations with TRIM [10].

Similarly Giles *et al.* [47] implanted phosphorus at normal incidence and a high tilt angle with the energy adjusted to have similar projected range. Again the total amount of TED was the same despite the higher energy tilted implant creating more Frenkel pairs.

Hence, the conclusion from present experimental data seems to indicate that the total net damage created is insensitive to the details of the Frenkel pair generation during implantation and mainly sensitive to the distribution of implanted ions. However, this convenient scenario needs revision when considering very low dose, high mass or very high energy implants when the details of the initial damage distribution lead to deviations from the "plus-one" model. Hence it is necessary to carefully select the initial conditions depending on a particular implant. This will be discussed further in Section 3.6. For example, the situation is much different for a high energy implant, where the interstitials are kicked in deeper into the silicon leaving behind a vacancy rich region near the surface. Fig. 3.2 shows simulations from TRIM [10] a Monte Carlo ion implantation simulator of a 2 MeV Si implant. Note that there is a distinct net vacancy rich region near the surface. The vacancy rich region extends well over 1μm and has net vacancy concentrations of $\sim 10^{18}\ \mathrm{cm}^{-3}$.

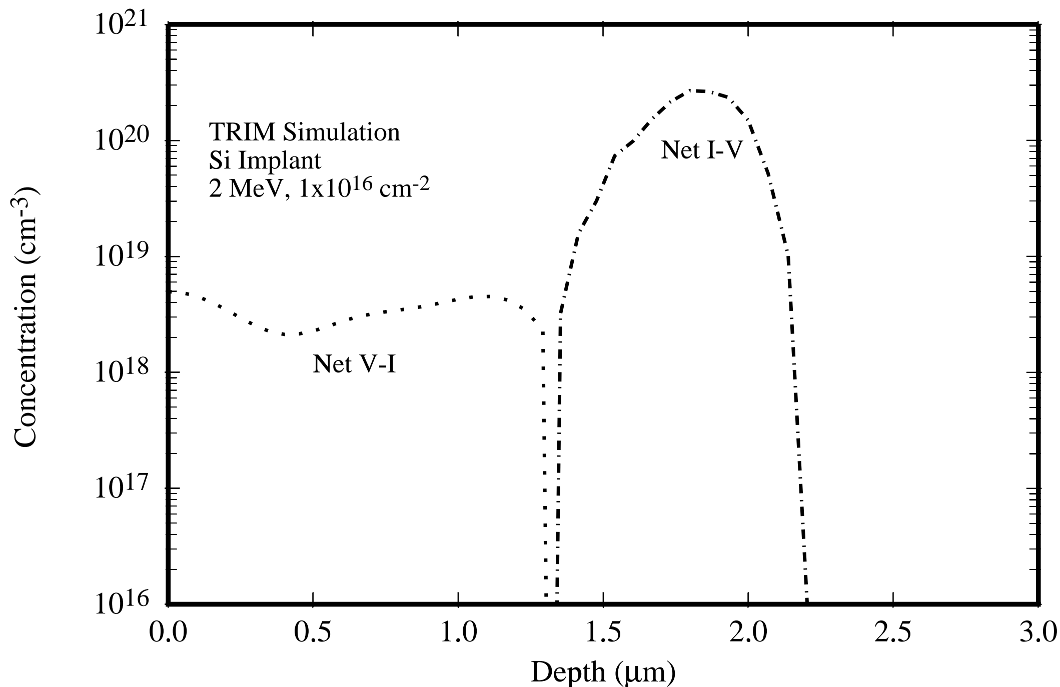

Figure 3.2: Monte Carlo simulation showing net initial distributions of interstitials and vacancies following a 2 MeV, $1 \times 10^{16}\,\mathrm{cm}^{-2}$ Si implant. The vacancy rich layer extends well over a μm.

3.2 Early work on boron deactivation and TED

Early work on Boron TED concentrated on experimental observations, measuring the extent of TED. After the invention of rapid thermal annealing (RTA), first observations of TED were reported: even for very short annealing times there was a considerable amount of dopant diffusion.

Most of the early papers [8, 73, 88] deal with dopant implants into silicon. A (high) dose of boron, phosphorus or arsenic was implanted into silicon, and after an RTA step the final profile was measured to determine the extent of TED. Angelucci *et al.* observed that boron and phosphorus show TED to a large extent, but arsenic shows little TED, and antimony shows almost no TED [8, 9]. To show this, Angelucci formed uniform layers of the dopants, patterned the sample, created damage by silicon implantation and annealed at various times and temperatures. For B and P, the Si-implanted regions showed a large increase in junction depth, whereas for As and Sb, the difference was minimal.

Combining the knowledge primary diffusion mechanisms of individual dopants with the observations on TED for different dopants, we may conclude that TED is related to

interstitial assisted diffusion. Indeed, after an ion implantation, there is a high supersaturation of interstitials due to the damage of the implant, and thus, this result is quite logical.

If we look at the time behavior of TED, we can observe that the enhancement is nearly independent of the ion-implant damage for initial times and after some period (duration of TED) the enhancement goes away [8, 79], such that we are left with normal diffusion which is many orders of magnitude smaller. This means that for early stages of TED the excess interstitial concentration is approximately fixed, and after some time it drops to its equilibrium value.

Another seemingly anomalous observation is that the amount of TED is larger at lower temperatures [73, 79]. This can be explained in the following fashion: Although the diffusion of dopants is faster at higher temperatures, the duration of TED is much shorter at higher temperatures, so that the overall junction movement gets smaller as the temperature is increased.

Hence, the following conclusions can be made:

- TED is caused by excess interstitial concentration that persists after ion implantation.
- The excess interstitial concentration remains approximately fixed during TED, and then drops to its equilibrium value.
- At higher temperatures the excess interstitial concentration disappears more rapidly, i.e. the duration of TED is shorter.

3.3 Interstitial clusters

As mentioned in Section 3.2, the excess interstitial concentration remains approximately fixed during TED, and then drops to its equilibrium value. This tells us that there must be a mechanism that stores the interstitials created by the implant damage and then releases them during TED, acting as a "source" of interstitials. In fact, if such a meta-stable state for interstitials didn't exist, they would rapidly diffuse to the surface and TED would be over in a very short time.

Experiments by Eaglesham *et al.* revealed the actual source of the interstitials during TED [28, 35]. They created damage by implanting Si into Si and then annealed the samples at various temperatures. They then performed plan-view and cross sectional Transmission Electron Microscopy (TEM) on the samples. They clearly saw the defects that store excess interstitials. These defects are the so-called "rod-like" or "$\{311\}$" defects.

The atomic structure of $\{311\}$ defects has been only recently resolved [93]. It is believed that interstitials form chains along $<110>$ direction and these chains come together

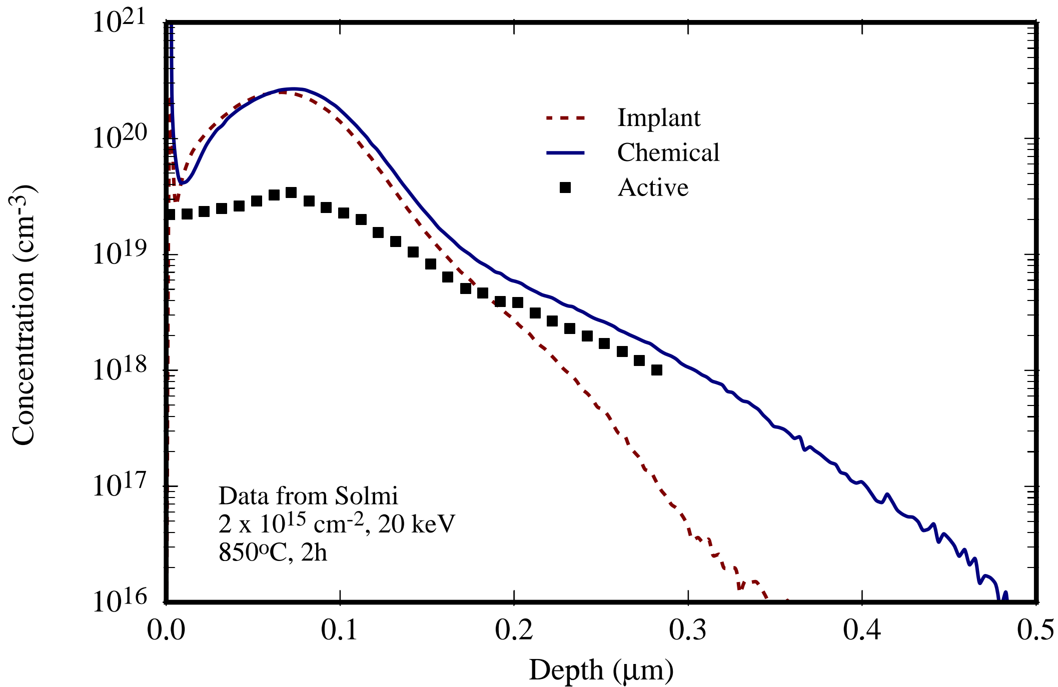

Figure 3.3: Boron chemical (SIMS) and activation (SRP) profiles after annealing of a 2×10^{15} cm^{-2} dose implant at 850°C for 2 h. The peak of the implanted boron profile is immobile and inactive to concentrations well below equilibrium solubility (from Solmi *et al.* [90]). Equilibrium boron solid solubility at 850°C $\sim 5 \times 10^{19}$ cm^{-3}.

to form a {311} plane. This defect can get very long (about 1μm) in the <110> direction, hence is given the name "rod-like" defects. The fact that the time needed for dissolution of {311} defects is equal to the duration of TED [35] is an excellent indicator that {311} defects are the source of the interstitials during TED. More recently, Cowern *et al.* have shown that at low temperatures small interstitial clusters are also important [27]. These small interstitial clusters (ICs) being less stable than {311} defects, maintain a much higher supersaturation clearly evident at lower temperatures. On further annealing, these ICs appear to transform into the more stable {311} defects by a ripening transition.

3.4 Boron interstitial clusters

A striking feature of profiles following implantation is that previously substitutional dopant may become non-substitutional, as evidenced by loss of electrical activity and inability to diffuse. Fig. 3.3 shows a typical implant profile after an anneal. It is clear that most of boron at the peak is inactive and immobile whereas the boron at the tail has undergone an

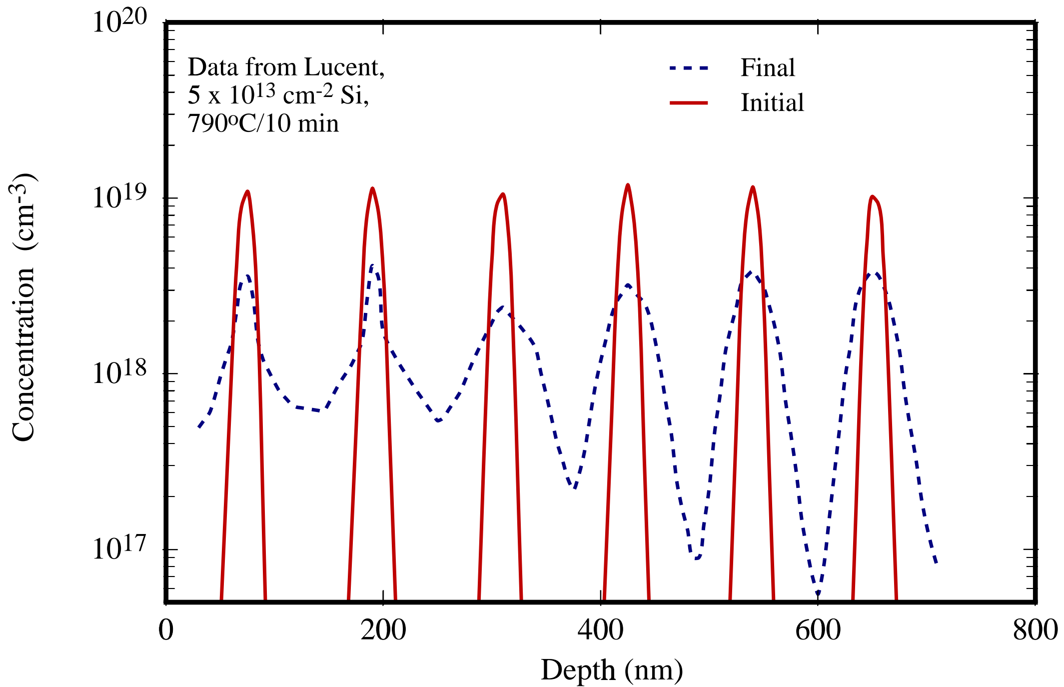

Figure 3.4: Delta doped boron marker layer after TED driven by a 5×10^{13} cm^{-2}, 40 keV Si implant and annealed at 790°C for 10 mins.

enhanced diffusion. Early work by Solmi *et al.* showed apparent solubility almost constant with dose but much lower than solid solubility.

Observations by Cowern *et al.* [26, 28] suggest that in systems where B is present in large doses, excess interstitials help boron atoms to form boron clusters and are themselves incorporated into these clusters (so-called Boron Interstitial Clusters, BICs), thereby reducing the number of mobile boron atoms. Although the BICs are not visible even with high resolution TEM, the diffusion profiles indicate that boron is becoming immobile where it is present at high doses. Boron marker layer experiments of Stolk *et al.* [91] show this effect very clearly. In these experiments marker layers were grown using molecular-beam epitaxy (MBE) and then implanted with Si. Thus, the damage dose is controlled independently from the dopant dose. Fig. 3.4 shows resdistribution after a 40 keV 5×10^{13} cm^{-2} Si implant annealed at 790°C for 10 mins. The projected range (R_p) of the Si implant is close to the first boron spike. However, interstitials from the Si implant have to diffuse into the sample to reach the deeper spikes. It was observed that a considerable part of the near surface boron spike remain immobile during annealing whereas the deeper spikes exhibit regular broadening without any immobile B. They also found that samples with lower doping only exhibit an enhanced diffusion and not an immobile peak. Further, they observed the boron peaks exist even after the dissolution of all $\{311\}$ defects. In the

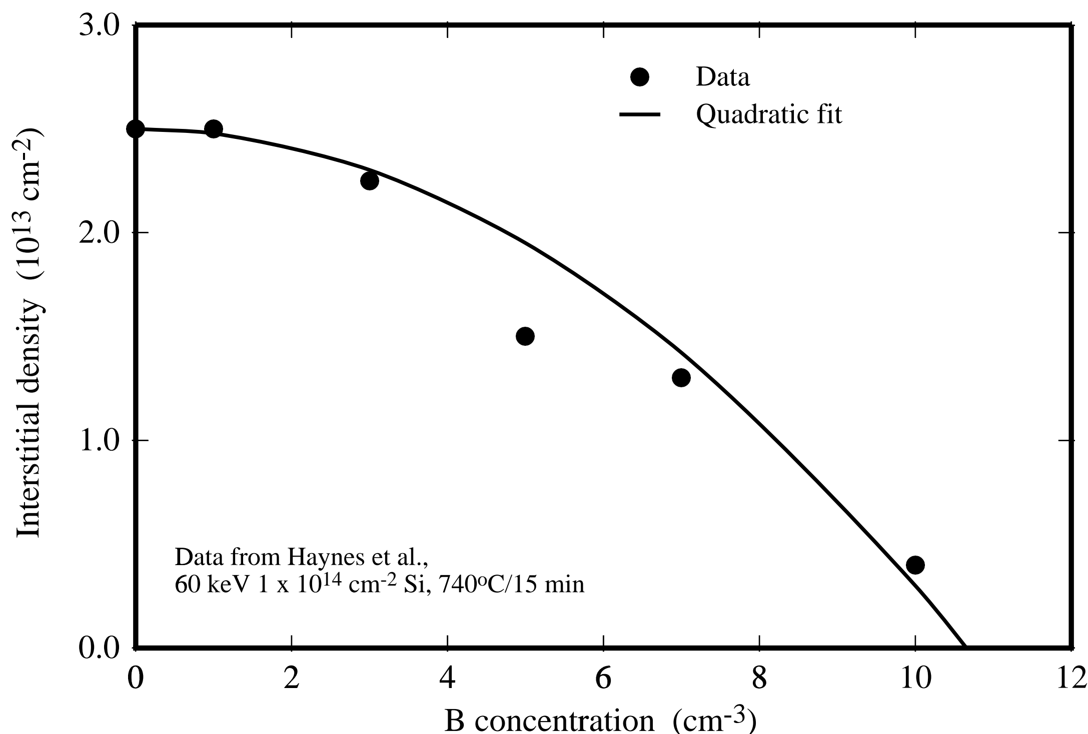

Figure 3.5: Area density of interstitials contained in {311} defects as a function of background boron concentration following anneal at 740°C for 15 mins. The solid line is a fit to the data assuming a quadratic dependence on B concentration. This would be the dependence of a cluster of type $B_{2m}I_m$.

absence of enough interstitials, the boron only shows enhanced diffusion as seen in the last peak. It can be noted that a higher dose marker layer shows considerable clustering even for the low dose Si implant. This suggests a high interstitial supersaturation is necessary for nucleation of the boron cluster precursor. Boron clusters must grow by absorbing interstitials. This would also explain the decrease in effective solid solubility with increase in interstitial super-saturations. Once formed, these clusters are fairly stable and can exist in the absence of any I super-saturations.

Haynes *et al.* [55] measured the total number of interstitials associated with {311} defects formed after Si implantation for different background boron doping. They found the fraction of excess interstitials trapped in {311} defects decreased as a function of the boron concentration, up to nearly complete disappearance of the {311} defects at high boron doping. Again, this clearly indicates the formation of boron interstitial clusters that compete with {311} defects for interstitials. From their results, it is possible to establish upper and lower bounds for the average number of B atoms that are required to effectively

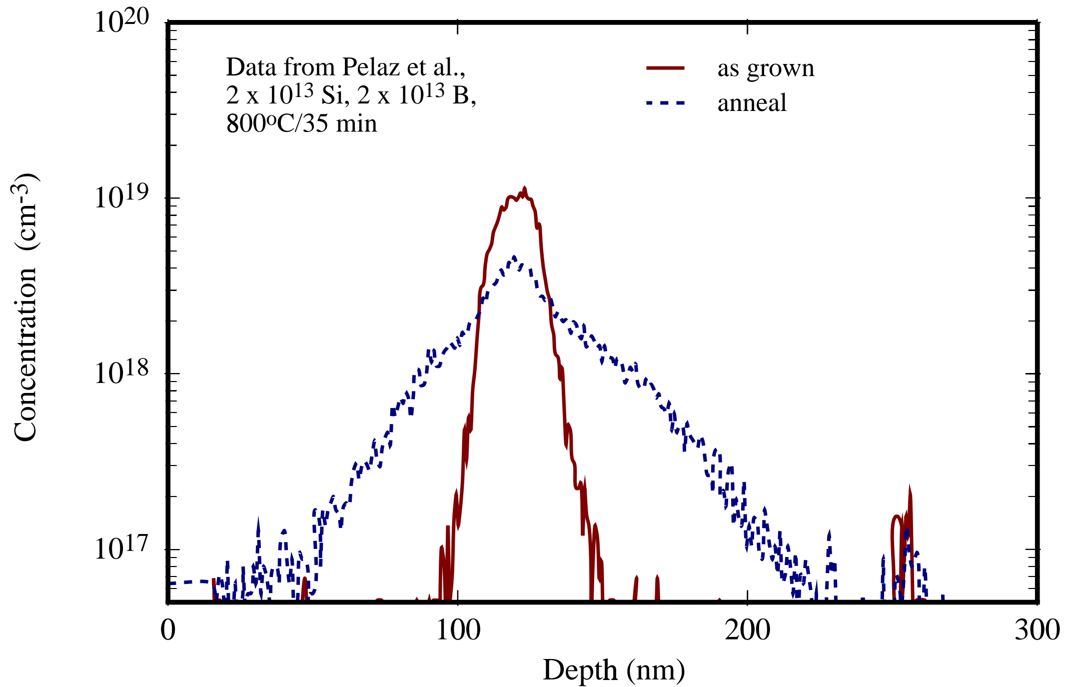

Figure 3.6: Clustering driven by a $2 \times 10^{13}\,\mathrm{cm}^{-2}$, 40 keV Si implant for a B marker layer of doses $2 \times 10^{13}\,\mathrm{cm}^{-2}$, annealed at 800°C for 35 mins.

remove one excess interstitial from the free interstitial population in Si. This was estimated to be more than 2 but less than about 25.

Pelaz *et al.* [83] performed similar experiments to Stolk *et al.* on delta doped superlattices but varied the marker layer boron dose and Si implant dose. Figs. 3.6 and 3.7 show the annealed profiles for two different B marker layer doses for a $2 \times 10^{13}\,\mathrm{cm}^{-2}$, 40keV Si implant and annealed at 800°C for 35 mins. It is apparent from Fig. 3.7 a small interstitial dose can immobilize several times its own dose of boron.

Hence, the following conclusions are in order:

- Boron apparent solubility is lowered below solid solubility because of agglomeration with interstitials.
- Formation of boron interstitial clusters also decrease interstitials bound to $\{311\}$.
- A small interstitial dose is enough to immobilize a much larger boron dose suggesting an average B/I size of around 3 – 5.
- Boron clustering occurs only under high I super-saturations.

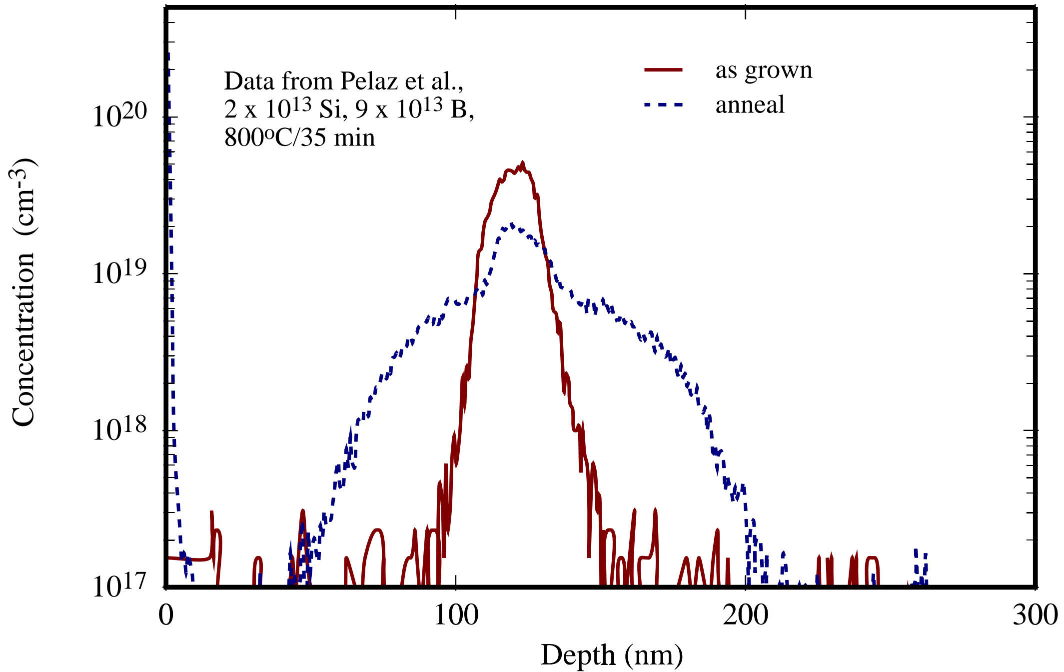

Figure 3.7: Clustering driven by a 2×10^{13} cm^{-2}, 40keV Si implant for a B marker layer of doses 9×10^{13} cm^{-2}, annealed at 800°C for 35 mins. Note that a low interstitial dose can deactivate a much larger fraction of boron.

- Boron clusters are more stable than {311} defects.

3.5 Vacancy clusters

It has been argued in Section 3.1 that most of the vacancies from the implant damage quickly recombine during the early stages of annealing. However, it was shown in Section 3.1 that during annealing of higher energy or larger mass implants it is possible vacancies may exist even after recombination.

Several experiments have indicated the presence of this vacancy rich region. Enhanced diffusion of Sb marker layers have been observed after MeV Si implants [36]. Metallic impurities getter not only at R_p the projected range of the implant but also at $R_p/2$ for high energy implants [14]. The gettering at R_p is attributed to interstitial type defects, whereas the gettering at $R_p/2$ is explained by the presence of the excess vacancies from the implant. It is also possible to create a vacancy rich region by higher mass implants. Pb implants have been found to decrease boron clustering in shallow boron marker layers [56]. This

vacancy rich layer can be used as a tool to reduce the depth and increase activation of boron or phosphorus junctions. For instance, use of MeV Si implants have been found to reduce the interstitials in end of range loops from high dose implants [85]. Since the vacancy induced effects seem to last over a period of annealing time [36], vacancies most likely grow into larger vacancy clusters or voids. Models for vacancy clustering are discussed in Chapter 6.

3.6 Simulation of initial damage

It has been pointed out in Section 3.1 that most of the recombination occurs quickly leaving a net damage very similar to a "plus one" model for light atoms like boron. However, I/V recombination is not the only process occurring during the post implant phase. Interstitials and vacancies can also diffuse and recombine at the surface. They can also agglomerate into extended defects. Here we discuss each of these effects separately.

3.6.1 Effect of surface

It is possible for a considerable fraction of the faster moving species to recombine at the surface and leave behind a net excess of the opposite type defect. This is because when the defect density is relatively small, the faster diffusing species can reach the surface before encountering the opposite type defect. As discussed in Section 2.4, calculations suggest that the diffusivity of vacancies is higher than the diffusivity of interstitials, particularly at lower temperatures. Thus we would expect a significant number of the vacancies in the vacancy-rich region near the surface to recombine at the surface. Thus, we will end up with much higher "plus" values for low dose or high atomic mass implants. Fig. 3.8 shows a simulation considering the damage annealing. TRIM simulation results are used as initial damage. It may be noted that for moderate or high implant doses I/V recombination quickly leads to a approximately "+1" distribution (particularly for lighter atoms and lower energies), thus validating the effectiveness of the "+1" approach. A more rigorous treatment of this "+n" factor involves the inclusion of correlation factors between the interstitial and vacancy cascades [15] and is beyond the scope of the present study.

Experiments have shown that TED scales non-linearly with dose and seems to almost saturate at low doses. This behavior cannot be satisfactorily explained using a "+1" model. We found that using the "+n" factor obtained from simulations of the full I and V profiles along with fast vacancy diffusion satisfactorily explains the dose dependence of boron marker layer experiments for silicon implants [80] as shown in Fig. 3.9. As shown in Fig. 3.10, using this same methodology for boron TED, we can successfully predict low dose TED, while using a "+1" model under-estimates the total amount of diffusion. Note that for low dose simulations, clustering is minimal and the model used for BICs has little or no impact.

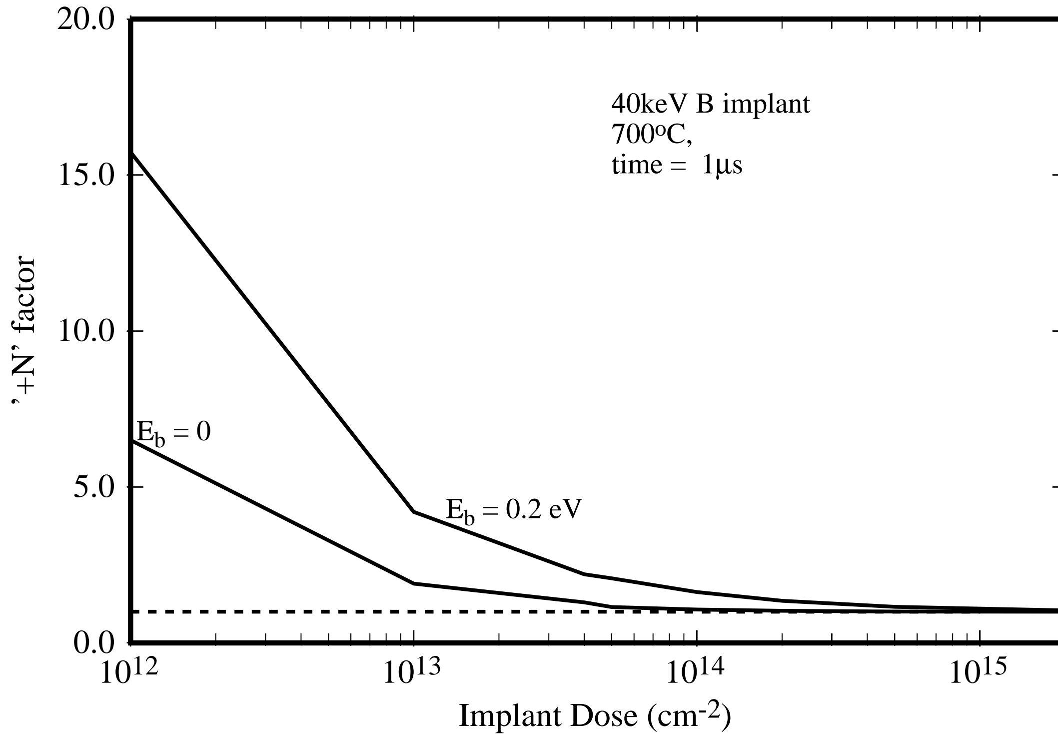

Figure 3.8: Net interstitial dose remaining after the recombination process starting from the total initial defect distributions. E_b is the barrier to I/V recombination.

3.6.2 Effect of clustering during recombination

For a accurate treatment of the damage annealing process it is necessary to also include clustering of both interstitials and vacancies as these may decrease the efficiency of the recombination process. Recent experiments of Cowern *et al.* [27] have shown that at low temperatures small interstitial clusters are the main source of interstitials. However, the validity of using a "+1" model for parameter extraction at such low temperatures is not clear [27]. For modeling interstitial clusters, we use the interstitial model derived by Cowern *et al.* [27]. Using parameters from Cowern *et al.* [27] gave good match to the experimental results using a "+1" approach. The model derived in Sec. 6 [19] is used for modeling the evolution of vacancy clusters. As seen in Fig. 3.11 using the full damage leads to a good match to the experimental data of Cowern *et al.* It can be noted that the initial supersaturation is dominated by small interstitial clusters that ripen into larger {311} defects. Also shown in Fig. 3.11 is comparison of super-saturations using the full initial cascade to using a "+1" approximation. Both models were found to yield almost identical supersaturations. However looking at the total number of vacancies and interstitials in clusters,

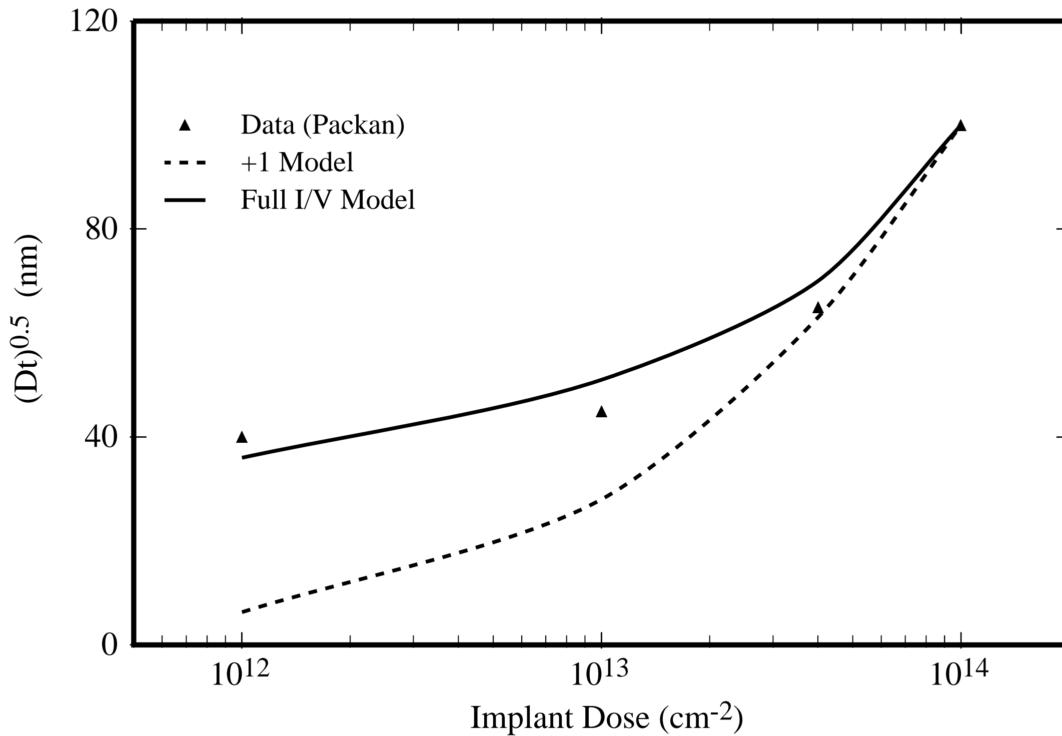

Figure 3.9: Dose dependence of TED measured for a boron marker layer following 200 keV Si implants. A “+n” model based on the full initial defect profile is able to predict diffusion behaviour.

it can be noted (Fig. 3.12) that the recombination process is not complete and significant vacancy clusters are present till around 600 sec. This does not affect the super-saturation as it is governed by the small interstitial clusters. This also confirms the validity of using a “+1” model for lower temperatures where recombination may not have been completed.

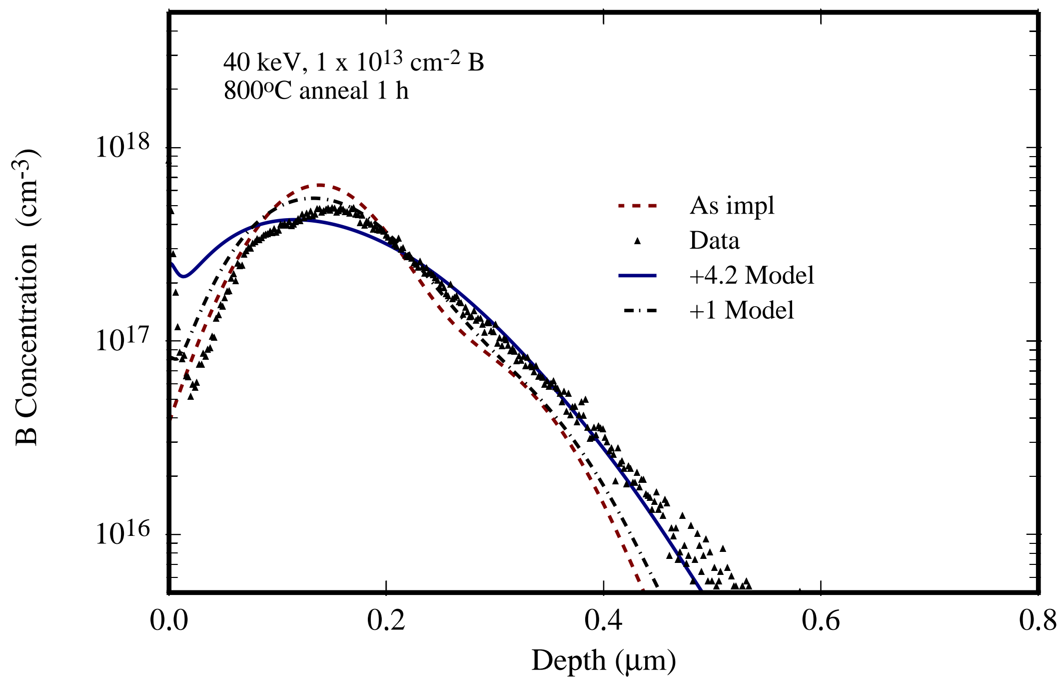

Figure 3.10: Prediction of B TED for 40 keV 10^{13}cm^{-2} B implant. A “+1” model predicts less diffusion than seen experimentally. A “+n” model based on the full initial defect profile is able to predict diffusion behaviour. Data is from Intel Corp. [44].

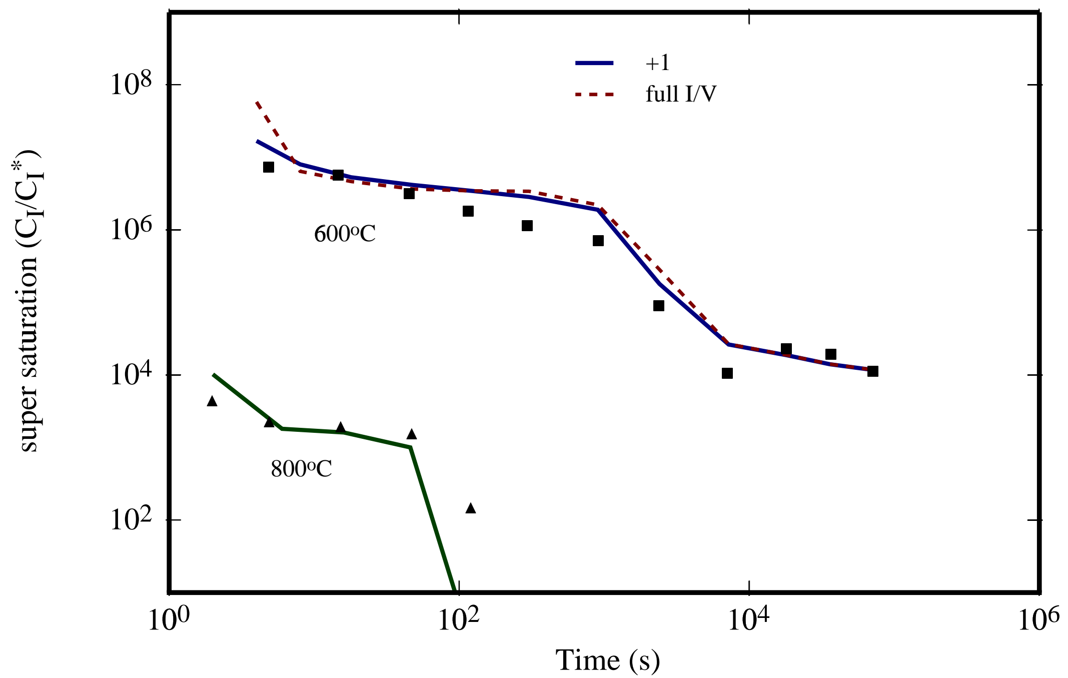

Figure 3.11: Interstitial super-saturations at 600°C and 800°C obtained using full damage (bold lines) and using a “+1” model (dashes). Note that the super-saturations obtained are almost independent of the initial conditions.

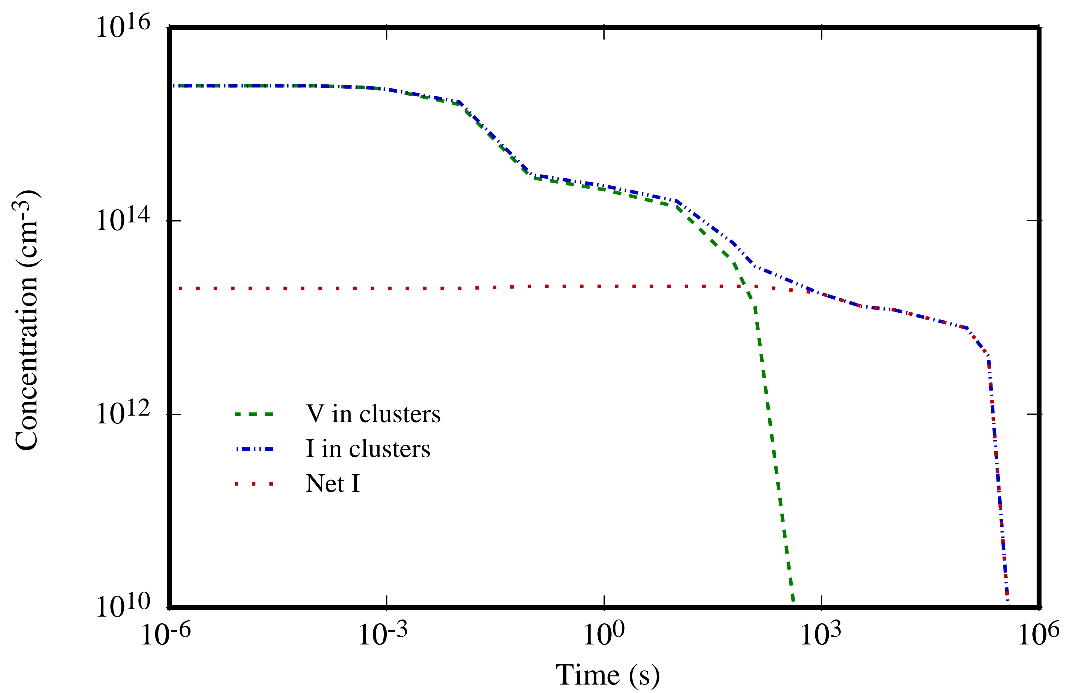

Figure 3.12: Figure shows evolution of interstitial and vacancy clusters during annealing of a $2 \times 10^{13}\mathrm{cm}^{-2}$ Si implant at 600°C. The vacancies exist till around 600 sec, after which the interstitials trapped in interstitial clusters is close to a "+1".

3.7 Summary

In this chapter, we have reviewed the experiments and models needed for simulation of the evolution of a ion implanted silicon during annealing. Particularly, we reviewed experiments that highlight the need for modeling interstial, vacancy and boron/interstitial clusters for successful process simulation. In Section 3.6 we showed our simulations to justify the use of a “+1” approach for the initial recombination process. In particular, we found in Section 3.6 deviations to the “+1” model for low dose implants where the surface plays a important role.

Chapter 4

Boron Cluster Models

In this chapter, we will describe our work on different approaches for modeling of boron interstitial clusters. As illustrated in Fig. 4.1, there is a huge array of potential cluster compositions. It is possible to model this system with a variety of approaches. Examples include either cluster-based or moment-based approaches. Cluster models consider a subset of discrete smaller sized clusters, whereas moment-based models like Kinetic Precipitation Model (KPM) [23] consider a wide range of cluster sizes but make assumption about smooth changes in properties with size, and limits the system to a narrower range of compositions.

4.1 Kinetic precipitation model

The aggregation process is driven by the minimization of the change in free energy with clustering. Here we are restating the approach of Clejan *et al.* [24, 32] using moments to describe the evolution of the size distribution. This energy can be written as the sum of a volume term which represents the change in energy upon adding either a boron or interstitial to the B_nI_m cluster, plus the excess surface energy and strain energies associated with finite size precipitates:

$$\Delta G_{n,m} = -nkT \ln\left(\frac{C_{\mathrm{B}}}{{C_{\mathrm{B}}}^{ss}}\right) - mkT \ln\left(\frac{C_{\mathrm{I}}}{{C_{\mathrm{I}}}^{*}}\right) + \Delta G_{n,m}^{\mathrm{surf}} + \Delta G_{n,m}^{\mathrm{stress}}. \tag{4.1}$$

We assume that the excess surface energy is a smooth function of size given by

$$\Delta G_{n,m}^{\mathrm{surf}} = c_1 n^{a_1} + c_2 n^{a_2}, \tag{4.2}$$

where $1 > a_1 > a_2 > \cdots$. The first term corresponds to the asymptotic behavior at large sizes, which is generally associated with the dependence of the active surface area on size (BICs are assumed to be spherical and hence $a_1 = 2/3$), and the other terms are corrections

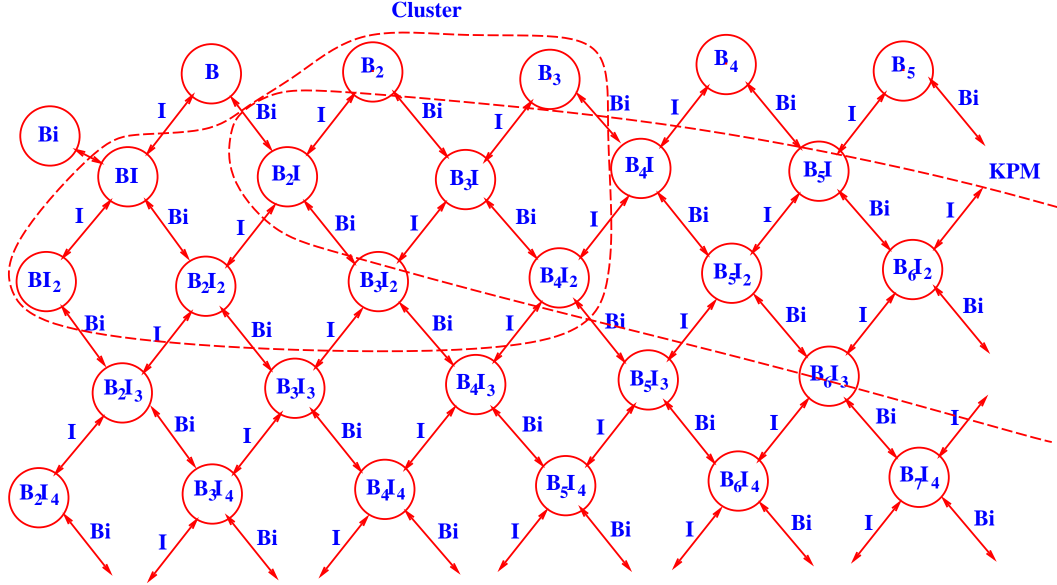

Figure 4.1: Array of possible BICs. Also indicated schematically are the range of compositions considered by cluster and KPM approaches.

for the deviation of the free energy from this asymptotic behavior at small sizes. The stress energy can be found from elasticity theory to be of the form,

$$\Delta G^{\text{stress}}_{n,m} = H_n + \frac{\alpha}{n}(m - \gamma n)^2. \tag{4.3}$$

If there were no point defect supersaturation, the optimum number of incorporated interstitials would be $m^* = \gamma n$. However, when $C_{\text{I}} > C^*_{\text{I}}$, the optimum number of point defects incorporated can be found by minimizing the free energy to be:

$$m^* = n\left(\gamma + \frac{kT}{2\alpha}\log(C_{\text{I}}/C^*_{\text{I}})\right), \tag{4.4}$$

which leads to an effective solid solubility of:

$$C^{\text{eff}}_{\text{ss}} = C_{\text{ss}}\left(\frac{C_{\text{I}}}{C^*_{\text{I}}}\right)^{-\gamma}\exp\left[-\frac{kT}{4\alpha}\left(\log(C_{\text{I}}/C^*_{\text{I}})\right)^2\right]. \tag{4.5}$$

It is evident from the above equation that the effective solubility decreases with increase in interstitial super-saturation as observed experimentally. The typical composition ranges described by this approach is shown in Fig. 4.1.

The size distribution for sizes larger than $k-1$ is represented in terms of a small number

of moments as discussed by Clejan *et al.* [23]. The moments are defined as :

$$m_i = \sum_{n=k}^{\infty} n^i f_n, \tag{4.6}$$

where $i = 0, 1, 2, \ldots$. The zeroth order moment of the distribution is simply the precipitate density, while the first moment corresponds to the density of precipitated solute atoms. Higher order moments further describe the shape of the size distribution. This transforms the system of equations to the following set [23]:

$$\frac{\partial m_i}{\partial t} = k^i R_k + \sum_{n=k}^{\infty} \left[(n+1)^i - n^i \right] R_n \tag{4.7}$$

Note that the sums over the R_n can all be written in terms of sums over f_n, nf_n, etc. Hence, they can be calculated from the moments if moments are used to describe the distribution. Since no finite number of moments can fully describe a full distribution, we need a closure assumption, which is an assumption about the form of the distribution. Since nothing is known about the distribution over size space, it is logical to use an energy minimizing closure assumption [23]. The energy minimizing closure assumption assumes that the distribution is the one that minimizes the free energy, given the moments. The resulting system is a three moment system in which the first three moments (m_0, m_1 and m_2) are solved [23, 43].

Setting $k = 2$ in Eq. 4.7 and optimizing for the energy parameters we find we can match a large amount of available data. Figs. 4.2, 4.3 and 4.4 show representative fits of this three moment model [17] to boron implant anneal data from Intel [44].

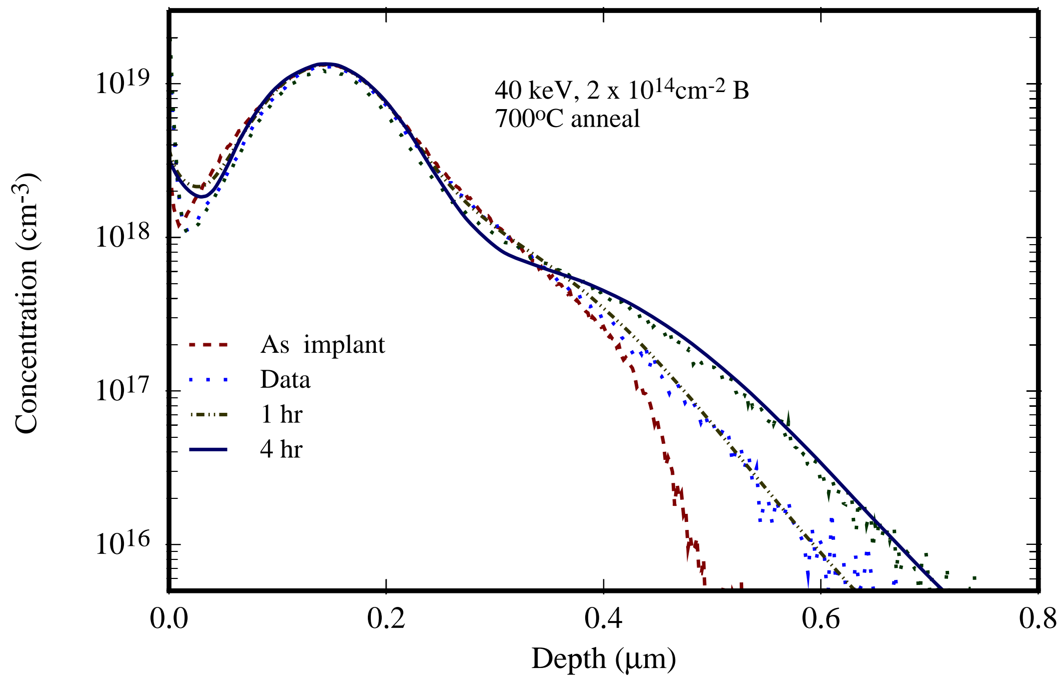

Figure 4.2: Simulations results for a 2×10^{14} cm^{-2}, 40 keV B implant annealed at 700°C using KPM model compared to data from Intel Corp. [44].

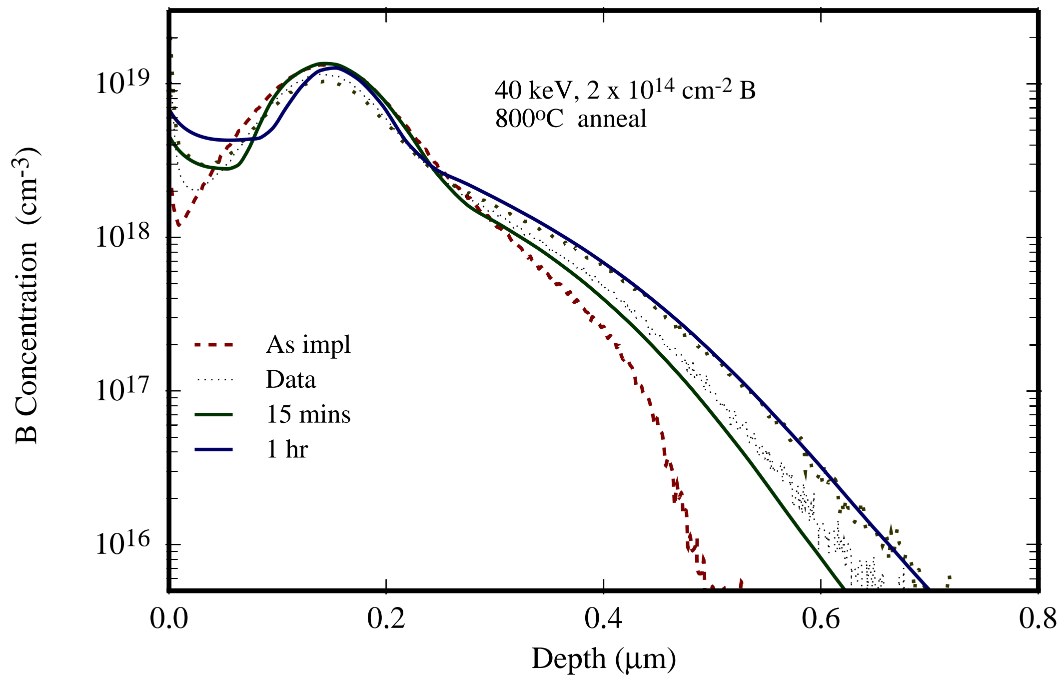

Figure 4.3: Simulations results for a 2×10^{14} cm^{-2}, 40 keV B implant annealed at 800°C using KPM model compared to data from Intel Corp. [44].

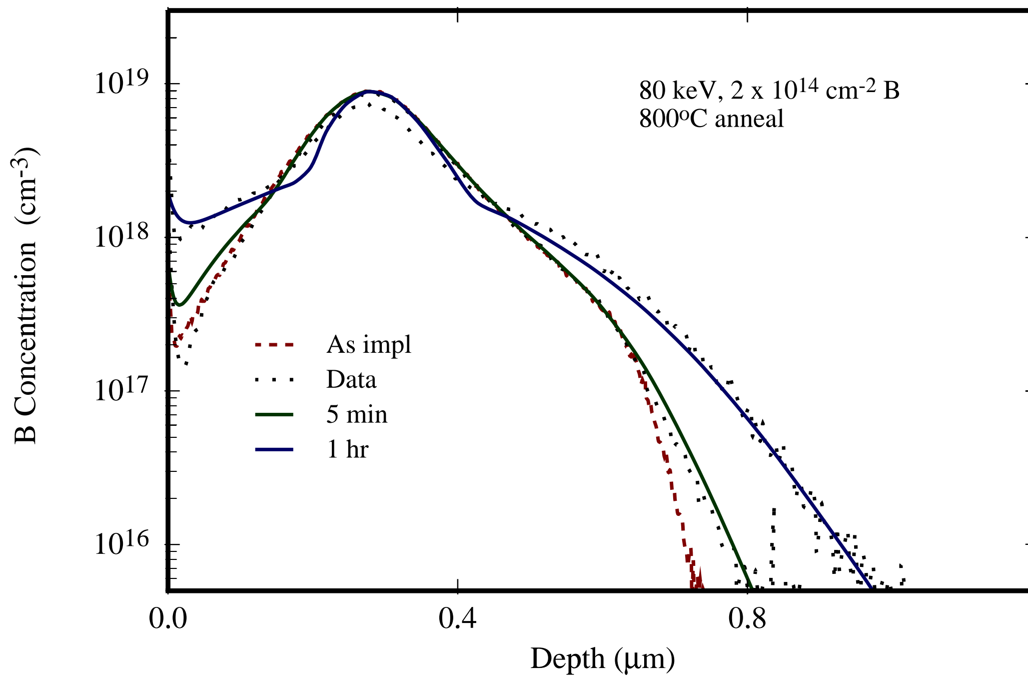

Figure 4.4: Simulations results for a $2 \times 10^{14}\text{cm}^{-2}$, 80 keV B implant annealed at 800°C using KPM model, compared to data from Intel Corp.

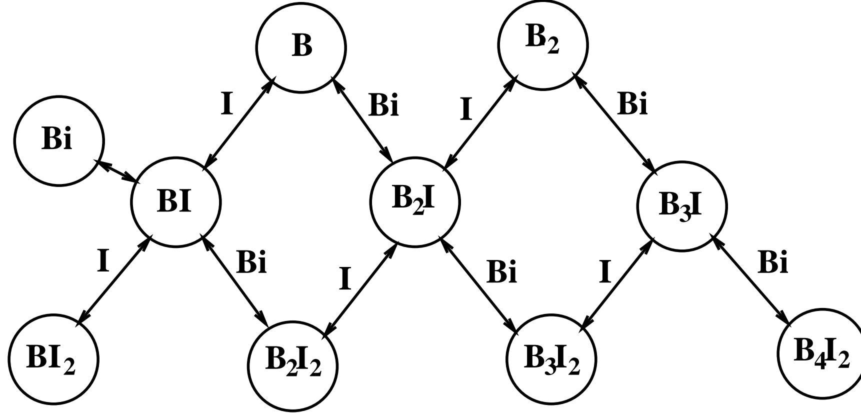

Figure 4.5: Cluster reactions considered in the full model as given by fundamental physical calculations [102].

4.2 Multi cluster models

Another approach to model BICs is to consider a finite set of discrete clusters as shown for example (dotted lines) in Fig. 4.1. Pelaz *et al.* [83] derived such a model with the cluster energetics optimized to fit data. For a more physical basis, we use cluster energies calculated by *ab-initio* methods at Lawrence Livermore National Labs [102]. In previous work, Caturla *et al.* [60] and Lilak *et al.* [67] presented boron clustering models based on the same calculations which we use in this work. In each case, they considered a large range of clusters such as shown in Fig. 4.5, with an associated large set of continuity equations and parameters. A problem with these approaches is that they lead to complicated models with associated long simulation times and large sets of non-unique parameters. Hence it is necessary to derive simpler models for effective use in Process Simulators.

As shown in Fig. 4.5 each cluster can grow/dissolve by the addition/release of a silicon self-interstial or boron interstitial. For example, a substitutional boron can react with a boron interstitial to form an immobile B_2I which can further react with another interstitial to form a B_2I_2 cluster or with a mobile interstitial boron (B_i) to give B_3I_2. There are thus two possible set of reactions:

$$\mathrm{B}_n\mathrm{I}_m + \mathrm{I} \;\Leftrightarrow\; \mathrm{B}_n\mathrm{I}_{m+1}, \tag{4.8}$$

$$\mathrm{B}_n\mathrm{I}_m + \mathrm{B}_i \;\Leftrightarrow\; \mathrm{B}_{n+1}\mathrm{I}_{m+1}. \tag{4.9}$$

with associated rates given by the equations:

$$R_{\mathrm{B}_n\mathrm{I}_m/\mathrm{I}} = 4\pi a D_\mathrm{I}\left(C_{\mathrm{B}_n\mathrm{I}_m}C_\mathrm{I} - \frac{C_{\mathrm{B}_n\mathrm{I}_{m+1}}}{K_{\mathrm{B}_n\mathrm{I}_m/\mathrm{I}}}\right), \tag{4.10}$$

Table 4.1: Cluster energetics based on atomistic calculations [60] used for the full system.

Reaction	Binding Energy (eV)
$B + I \Leftrightarrow BI$	1.0
$B + I \Leftrightarrow B_i$	0.7
$B_i + B \Leftrightarrow B_2I$	1.3
$B_2 + I \Leftrightarrow B_2I$	1.6
$B_2I + I \Leftrightarrow B_2I_2$	1.2
$BI + B_i \Leftrightarrow B_2I_2$	1.5
$BI + I \Leftrightarrow BI_2$	1.4
$B_3 + I \Leftrightarrow B_3I$	3.3
$B_2 + B_i \Leftrightarrow B_3I$	2.8
$B_2I + B_i \Leftrightarrow B_3I_2$	−0.1
$B_3I + I \Leftrightarrow B_3I_2$	−1.3
$B_3I + B_i \Leftrightarrow B_4I_2$	1.5

$$R_{\mathrm{B}_n\mathrm{I}_m/\mathrm{B_i}} = 4\pi a D_{\mathrm{B_i}} \left(C_{\mathrm{B}_n\mathrm{I}_m} C_{\mathrm{B_i}} - \frac{C_{\mathrm{B}_{n+1}\mathrm{I}_{m+1}}}{K_{\mathrm{B}_n\mathrm{I}_m/\mathrm{B_i}}} \right). \tag{4.11}$$

Cluster energetics calculations from Caturla *et al.* [60] were used as the basis for the simulations, with 10 different clusters considered: BI, BI_2, B_2I, B_2I_2, B_3I, B_3I_2, B_4I_2, B_2, B_3. The cluster energies used in the simulation are tabulated in Table 4.1. It should be noted that using dissociation energies from Caturla *et al.* [60] and following different pathways for the formation of B_2I and B_2I_2 from B and I yields different binding energies. Hence, an intermediate energy was chosen. This choice does not change the relative stability of clusters.

4.2.1 Analysis of model

We now try to derive a simple model from this multi cluster model. The large binding energies for the formation of B_3I suggests the importance of B_3I clusters. However, it is necessary to look at the kinetics and energetics of all these processes to identify the number of equations and cluster concentrations that need to be solved to model this system. For example, interstitial rich clusters may be more important in the presence of the higher interstitial supersaturations typical of the very early stages of annealing.

We first look at the kinetics of the different processes. Concentrations of clusters that are in dynamic equilibrium with the free interstitial and boron concentrations can be expressed as simple analytic expressions (e.g. $C_{\mathrm{B}_n\mathrm{I}_m} = K_{\mathrm{B}_n\mathrm{I}_m} C_{\mathrm{B}}^n C_{\mathrm{I}}^m$). Fig. 4.6 shows the time evolution of cluster concentrations normalized by their equilibrium value ($C_{\mathrm{B}_n\mathrm{I}_m}/K_{\mathrm{B}_n\mathrm{I}_m} C_{\mathrm{B}}^n C_{\mathrm{I}}^m$)

for each cluster species. A value of '1' indicates that the system is in dynamic equilibrium with the free B and I. These normalized values are calculated at the peak of the implant profile. Our analysis of this system find that most of the clusters rapidly achieve dynamic equilibrium with the free boron and interstitial concentrations, suggesting the possibility of reducing the number of equations and parameters needed to describe the system. As shown in Fig. 4.6, except for B_3I and B_4I_2, all the clusters reach dynamic equilibrium with the B and I concentrations within 0.1 sec. B_3I and B_4I_2 are also in local dynamic equilibrium with each other as demonstrated by their overlapping curves in Fig. 4.6.

We next identify the most stable clusters for interstitial supersaturations characteristic of different annealing times. Fig. 4.7 shows the equilibrium concentrations of the clusters under conditions typical of the period before $\{311\}$ defects form. For high interstitial supersaturations representative of very short times (< 1 sec), BI_2 can be present in significant numbers. This helps to immobilize boron atoms initially. Note that the strong clustering keeps the free B and thus the B_2I_2 concentration low, and at such short times the B_3I and B_4I_2 concentrations are far below their equilibrium values due to the slower formation rate of B_3I (Fig. 4.6). Once $\{311\}$ defects form, the interstitial concentration drops. For typical TED supersaturations ($C_I/C_I^* \sim 10^3$), the dominant species is B_3I, as shown in Fig. 4.8.

At the same time, only a small subset of the clusters are ever present in significant numbers. Fig. 4.7 shows the equilibrium concentrations of the clusters before the formation of $\{311\}$ defects. Under high interstitial super-saturations representative of very short times (~ 1 sec), BI_2 can be present in significant numbers. This helps to immobilize boron atoms initially. At such short times the B_3I and B_4I_2 concentrations are far below their equilibrium values due to the slower formation of B_3I. Once $\{311\}$ defects form, the interstitial concentration drops. From the equilibrium diagram for typical TED super-saturations ($C_I/C_I^* \sim 10^3$) as shown in Fig. 4.8, the dominant species is B_3I.

4.3 Simple cluster model

The following conclusions can be made from the above analysis:
(i) The concentration of all the small clusters rapidly equilibrate with the free B and I concentrations.
(ii) At short times, BI_2 is the dominant cluster.
(iii) At longer times, B_3I is the dominant cluster and needs to be solved numerically since it is present in non-equilibrium quantities.

Based on the above observations, we can simplify the system of immobile clusters from ten to that of just B_3I. Since B_3I forms via the unstable cluster B_3I_2 [60] the reactions,

$$B_2I + B_i \underset{k_1^r}{\overset{k_1^f}{\rightleftharpoons}} B_3I_2 \tag{4.12}$$

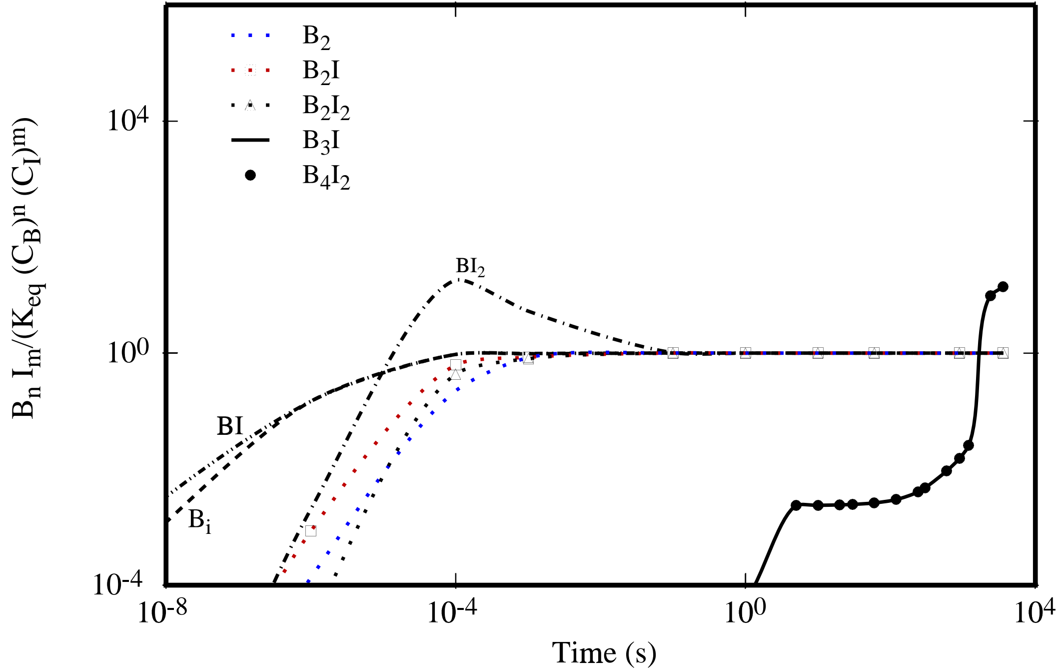

Figure 4.6: Simulations using the full cluster model of normalized cluster concentrations (relative to their equilibrium value) versus time for an 800°C anneal.

$$B_3I_2 \underset{k_2^r}{\overset{k_2^f}{\rightleftharpoons}} B_3I + I \tag{4.13}$$

can be combined to give a net formation rate for B_3I:

$$R_{B_3I} = k_{B_3I}^{\text{eff}} \left(C_{B_2I} C_{B_i} - \frac{C_{B_3I} C_I}{K_{B_3I}} \right). \tag{4.14}$$

$$K_{B_3I} = \frac{k_1^f k_2^f}{k_1^r k_2^r} = \exp\left(\frac{-0.1 \text{ eV} + 1.3 \text{ eV}}{kT} \right), \tag{4.15}$$

using values from Table 1.

$$k_{B_3I}^{\text{eff}} = k_1^f \left(\frac{k_2^f}{k_1^r + k_2^f} \right) = \left[\frac{k_1^f}{1 + k_1^f / (k_2^r K_{B_3I})} \right], \tag{4.16}$$

where $k_2^f / (k_1^r + k_2^f)$ represents the probability that B_3I_2 will dissociate into $B_3I + I$ rather

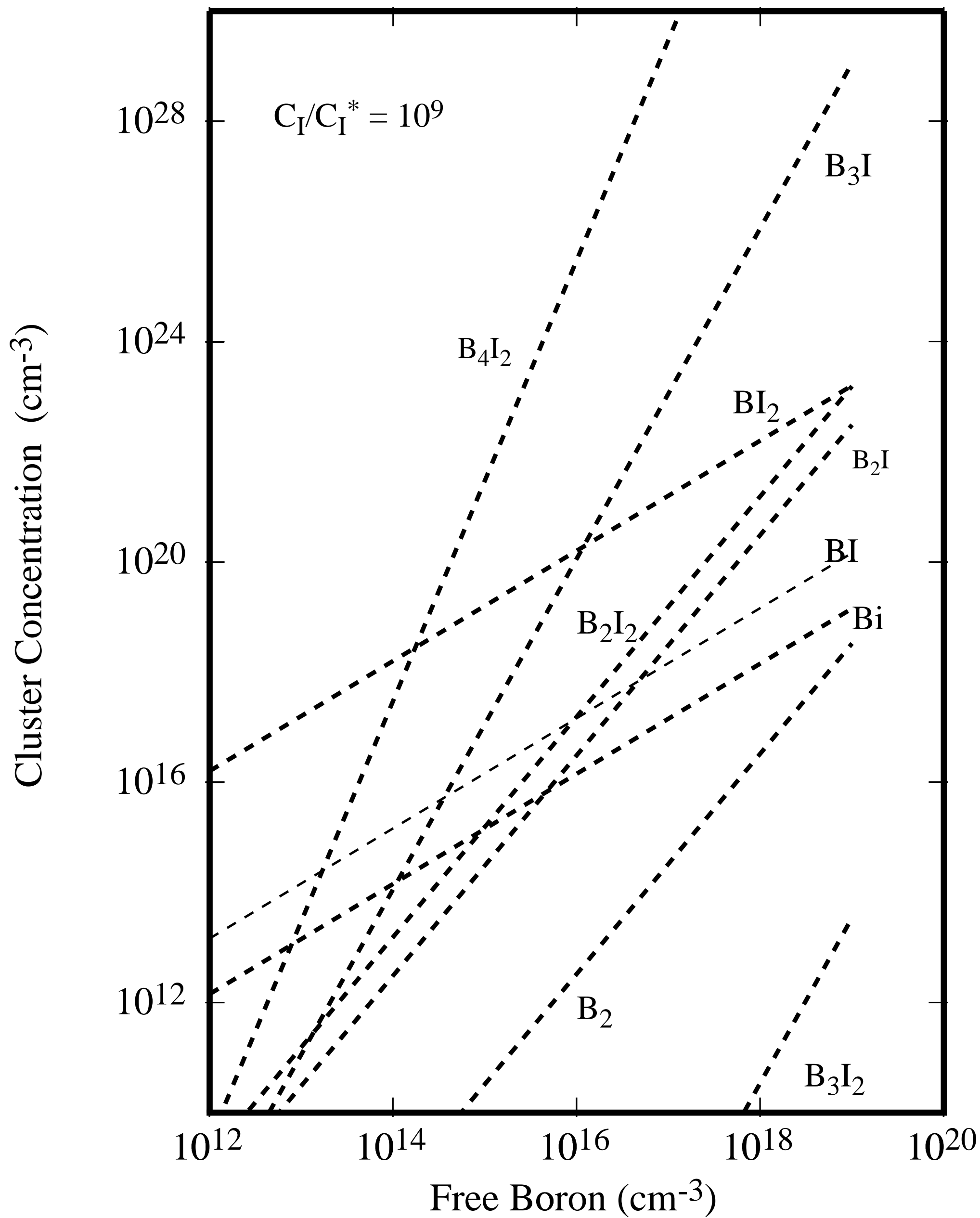

Figure 4.7: Equilibrium cluster concentrations versus free boron concentration at 800°C for free interstitial concentrations of $10^9 C_I^*$ characteristic of very early stages of TED. Initially, BI_2 is the primary cluster and helps immobilize the boron as noted by Pelaz *et al.* [83]

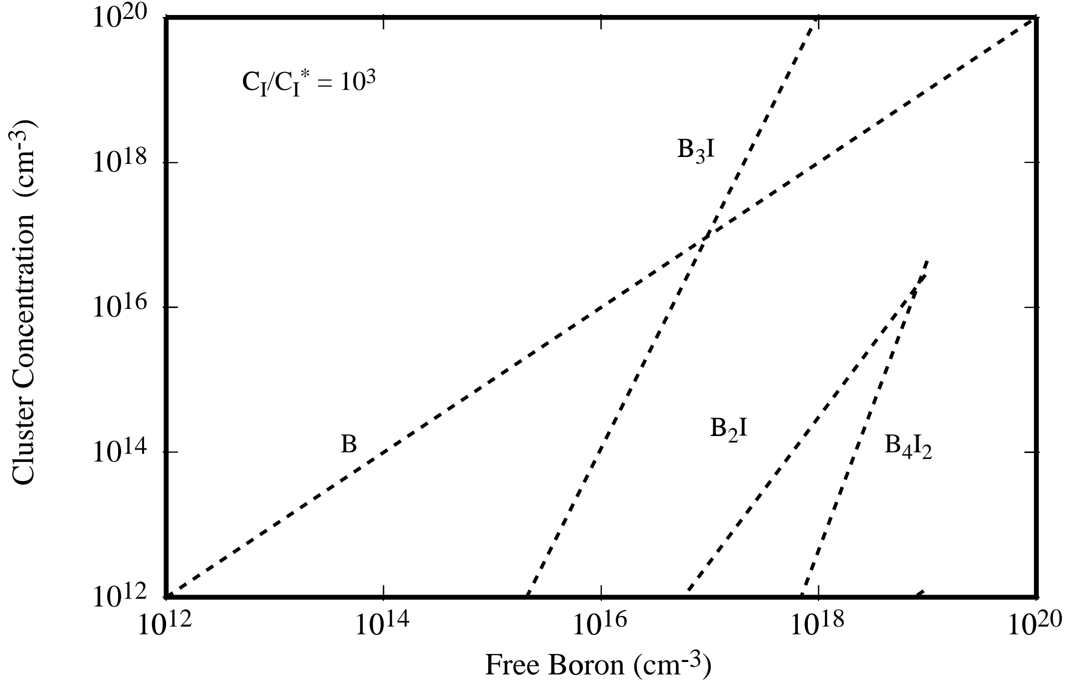

Figure 4.8: Equilibrium cluster concentrations versus free boron concentration at 800°C for free interstitial concentrations of $10^3 C_I^*$ typical of TED conditions in the presence of {311} defects. B_3I is the primary cluster during most of the anneal.

than $B_2I + B_i$. Since the small clusters are in dynamic equilibrium,

$$C_{B_2I} = K_{B_2I} C_B C_{B_i}. \tag{4.17}$$

k_1^f and k_2^r are assumed to be diffusion limited and are hence,

$$k_1^f = 4\pi a_0 D_{B_i}, \tag{4.18}$$
$$k_2^r = 4\pi a_0 D_I. \tag{4.19}$$

As BI_2 is the dominant cluster at short times (see Fig. 4.7), we can neglect the other small clusters. Since the BI_2 reaches local equilibrium quickly (see Fig. 4.6), we can approximate the BI_2 concentration by solving the equations:

$$C_B^{tot} = C_B + K_{BI_2} C_B C_I^2, \tag{4.20}$$
$$C_I^{tot} = C_I + K_{BI_2} C_B C_I^2. \tag{4.21}$$

We can thus use an analytic function for BI_2 as a function of the total B and I concen-

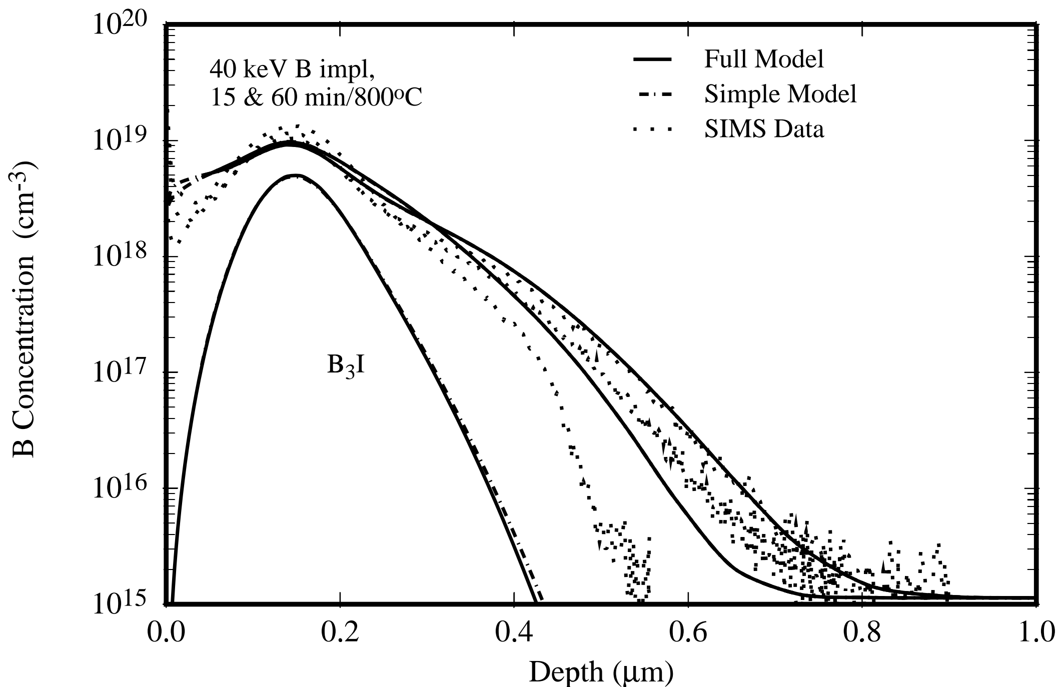

Figure 4.9: Comparison of full model with the simplified model for a 40 keV $2\times10^{14}\,\mathrm{cm}^{-2}$ B implants annealed at 800°C for various times. Also shown for comparison are SIMS data from Intel [44]. Note that the full model and simple model show indistinguishable final profiles. The B_3I concentrations for the two models (shown after a 1 h anneal) are also nearly identical.

trations. However, the rate equation for BI_2 is actually easier to incorporate and requires minimal computational overhead.

We compared our simplified model to the full system and found that the results are virtually indistinguishable. A moment-based model characterized based on TEM results was used for interstitial defects ({311} defects and dislocation loops) [41, 42, 43]. Fig. 4.9 show an example of this comparison as well as to data from Intel [44] for TED at 800°C. Similar agreement was obtained at higher and lower temperatures (700 and 900°C) as well as for other implant doses.

4.4 Extension to charge states

The cluster models considered in earlier sections did not include charge states for the various clusters. However, since clustering involves deactivation and formation of clusters of

different charges, it is necessary to include cluster charge states to be physically consistent. We have extended our model based on charged defect calculations from Lenosky *et al.* [64] which conclude that the dominant charge states of the clusters we have identified as critical to modeling are $(BI_2)^+$, $(B_2I)^0$ and $(B_3I)^-$. Clustering proceeds as:

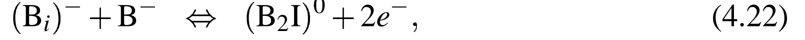

$$(B_i)^- + B^- \Leftrightarrow (B_2I)^0 + 2e^-, \tag{4.22}$$

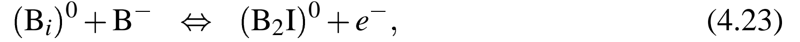

$$(B_i)^0 + B^- \Leftrightarrow (B_2I)^0 + e^-, \tag{4.23}$$

Since $(B_2I)^0$ quickly reaches dynamic equilibrium with B and B_i,

$$C_{(B_2I)^0} = K^{eq}_{(B_2I)^0} C_{B^-} C_{(B_i)^-} \left(\frac{p}{n_i}\right)^2. \tag{4.24}$$

$(B_3I)^-$ formation can proceed by a reaction with B_i which has either a net negative $(B_i)^-$ or neutral $(B_i)^0$ charge. Hence we can write:

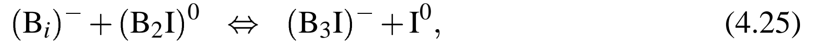

$$(B_i)^- + (B_2I)^0 \Leftrightarrow (B_3I)^- + I^0, \tag{4.25}$$

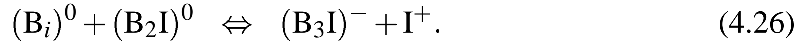

$$(B_i)^0 + (B_2I)^0 \Leftrightarrow (B_3I)^- + I^+. \tag{4.26}$$

It should be noted that under extrinsic conditions, diffusion via $(B_i)^0$ dominates ($D_B \propto p/n_i$), so Eq. 4.26 is the dominant pathway. The reaction rates given by Eqs. 4.25 and 4.26 are:

$$R_{(B_i)^-/B_2I} = k_{B_i^-/B_2I}\left[C_{(B_i)^-}C_{(B_2I)^0} - \frac{C_{(B_3I)^-}C_{I^0}}{K_{(B_i)^-/B_2I}}\right], \tag{4.27}$$

$$R_{(B_i)^0/B_2I} = k_{B_i^0/B_2I}\left[C_{(B_i)^0}C_{(B_2I)^0} - \frac{C_{(B_3I)^-}C_{I^+}}{K_{(B_i)^0/B_2I}}\right]. \tag{4.28}$$

Assuming ionization reactions are fast and that diffusivities are independent of charge state ($D_{(B_i)^-} = D_{(B_i)^0}$ and $D_{I^0} = D_{I^+}$), we can write the equilibrium constants for Eqs. 4.27 and 4.28 in terms of the Fermi level dependent boron diffusivities available from equilibrium experiments[99] (D_B^+ and D_B^0):

$$\frac{K_{(B_i)^-/B_2I}}{K_{(B_i)^0/B_2I}} = \frac{C_{(B_i)^0}}{C_{(B_i)^-}}\frac{C_{I^0}}{C_{I^+}} = \frac{D_B^+}{D_B^0 K_{I^+}}. \tag{4.29}$$

K_{I^+} accounts for the Fermi level dependence of interstitial concentration [45]. It is defined as discussed in Sec. 2.2 (Eq. 2.18) to be:

$$C_I^+ = K_{I^+} C_I^0 \left(\frac{p}{n_i}\right). \tag{4.30}$$

The total rate of formation of $(B_3I)^-$ is then

$$R_{(B_i)/B_2I} = (k^{eff}_{B_i^-/B_2I} + k^{eff}_{B_i^0/B_2I}) \times \left[C_{(B_i)^-} C_{(B_2I)^0} - \frac{C_{(B_3I)^-} C_{I^0}}{K_{(B_i)^-/B_2I}} \right], \quad (4.31)$$

where, $K_{(B_i)^-/B_2I}$ is the equilibrium constant defined for Eq. 4.27 with,

$$k^{eff}_{B_i^-/B_2I} = \left(\frac{4\pi r_{cap} D_{B^0}}{K_{B_i^-/B_2I} C^*_{I^0} \left(1 + \gamma^{eff}_{B_i^-/B_2I}\right)} \right), \quad (4.32)$$

$$k^{eff}_{B_i^0/B_2I} = \left(\frac{4\pi r_{cap} D_{B^+} (p/n_i)}{K_{B_i^-/B_2I} C^*_{I^0} \left(1 + \gamma^{eff}_{B_i^0/B_2I}\right)} \right), \quad (4.33)$$

$$\gamma^{eff}_{B_i^-/B_2I} = D_{B^0} / (D_{I^0} C^*_{I^0} K_{I^0/(B_i)^-} K_{B_i^-/B_2I}), \quad (4.34)$$

$$\gamma^{eff}_{B_i^0/B_2I} = D_{B^+} / (D_{I^0} C^*_{I^0} K_{I^+} K_{I^0/(B_i)^-} K_{B_i^-/B_2I}). \quad (4.35)$$

The formation of $(BI_2)^+$ can proceed by these reactions,

$$(B_i)^0 + I^+ \Leftrightarrow (BI_2)^+, \quad (4.36)$$

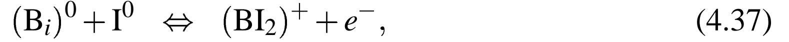

$$(B_i)^0 + I^0 \Leftrightarrow (BI_2)^+ + e^-, \quad (4.37)$$

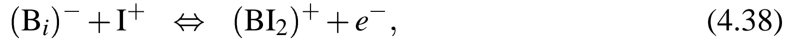

$$(B_i)^- + I^+ \Leftrightarrow (BI_2)^+ + e^-, \quad (4.38)$$

$$(B_i)^0 + I^0 \Leftrightarrow (BI_2)^+ + 2e^-. \quad (4.39)$$

The overall net reaction rate is thus:

$$R_{BI_2} = k_{BI_2} \left[C_{(B_i)^0} C_{I^+} - \frac{C_{BI_2}}{K_{(B_i)^0/I^+}} \right], \quad (4.40)$$

$$k_{BI_2} = 4\pi a_0 \left(D_{B_i} + D_I\right) \times \left(1 + \frac{1}{K_{I^+}} \frac{n}{n_i}\right) \left(1 + \frac{D^0_B}{D^+_B} \frac{n}{n_i}\right). \quad (4.41)$$

4.5 Comparison to chemical data

The extended boron cluster model was found to give good match to the TED data shown in the previous section. The model parameters were further optimized to fit a wide range of data. Shown in Fig. 4.10 is comparison to data from Intel [44]. Similarly Fig. 4.11 shows comparison to data from Solmi *et al.* [90]. We find the boron cluster model also can predict the TED profiles for higher boron doses by including a loop model for interstitials. Shown in Figs. 4.12 and 4.13 is comparison to data [44, 90] for a 2×10^{15} cm^{-2}, 40 and 20 keV B implant annealed at 800°C. However, it should be noted that this model does not predict high dose, high temperature anneals. For these cases, experiments show sharp boron peaks suggestive of larger sized clusters. Hence it would be necessary to include larger size clusters to model such data.

4.6 Solid Solubility Model

The simplest model to include the effect of larger sized clusters is to use a solid solubility model. The rate equations for the solid solubility model can be formulated as follows [43]:

$$\begin{aligned} \frac{\partial m_1}{\partial t} &= D_{\mathrm{B}}\lambda m_1(C_{\mathrm{B}} - C_{\mathrm{ss}}) + \begin{cases} D_{\mathrm{B}}\lambda(C_{\mathrm{B}} - C_{\mathrm{ss}})^2 & \text{for } C_{\mathrm{B}} > C_{\mathrm{ss}} \\ 0 & \text{for } C_{\mathrm{B}} \leq C_{\mathrm{ss}} \end{cases} \\ \frac{\partial C_{\mathrm{B}}}{\partial t} &= -\frac{\partial m_1}{\partial t} \end{aligned} \tag{4.42}$$

where C_{ss} is the boron equilibrium solid solubility, λ is an effective capture distance and m_1 tracks the total number of boron atoms in precipitates. The first term in the above equation is for growth/dissolution of the precipitates, whereas the second term is for nucleation of precipitates when $C_{\mathrm{B}} > C_{\mathrm{ss}}$. This model is used for modeling annealing of ultra low energy implants as discussed in Chapter 5.

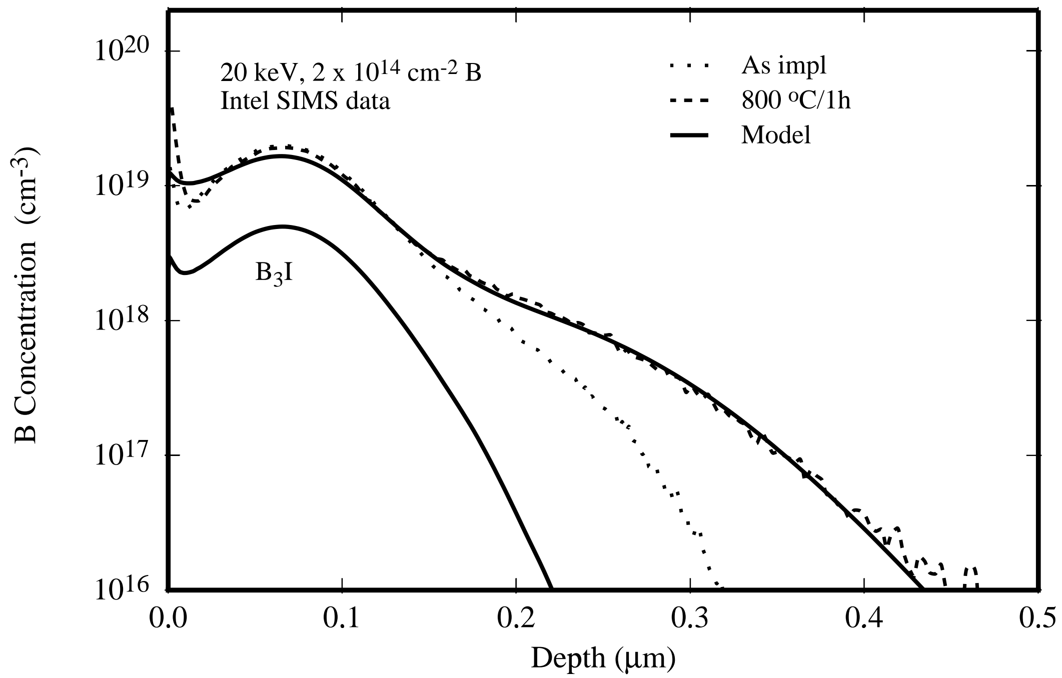

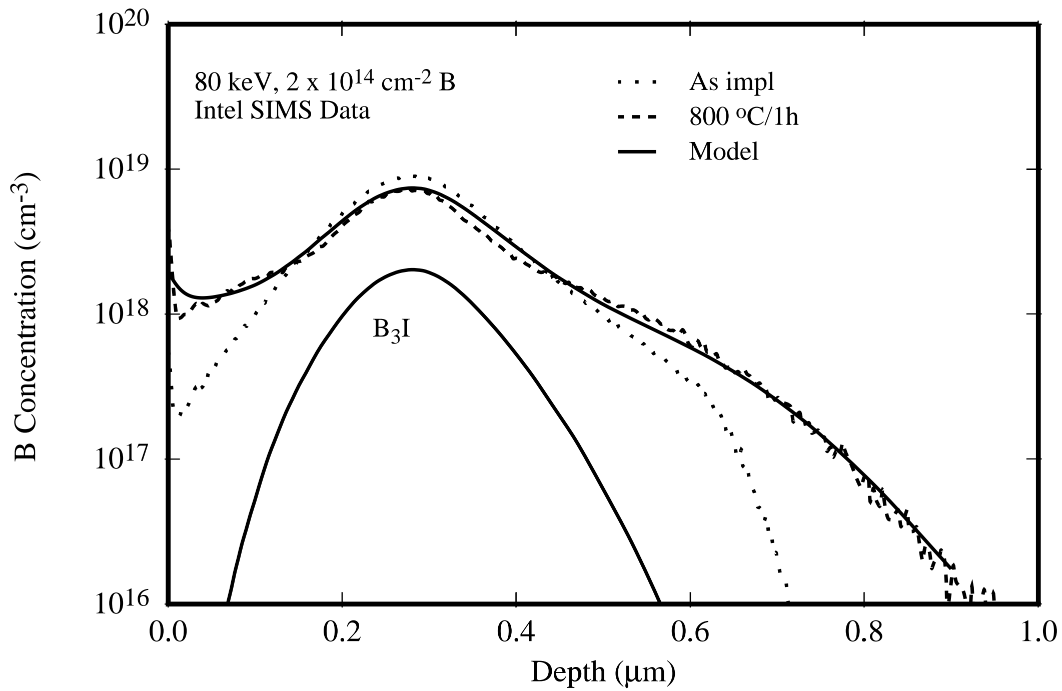

Figure 4.10: Comparison of simulation to experimental data [44] for 2×10^{14} cm^{-2} (a) 20 keV (b) 80 keV boron implants after 1 hr anneals at 800°C.

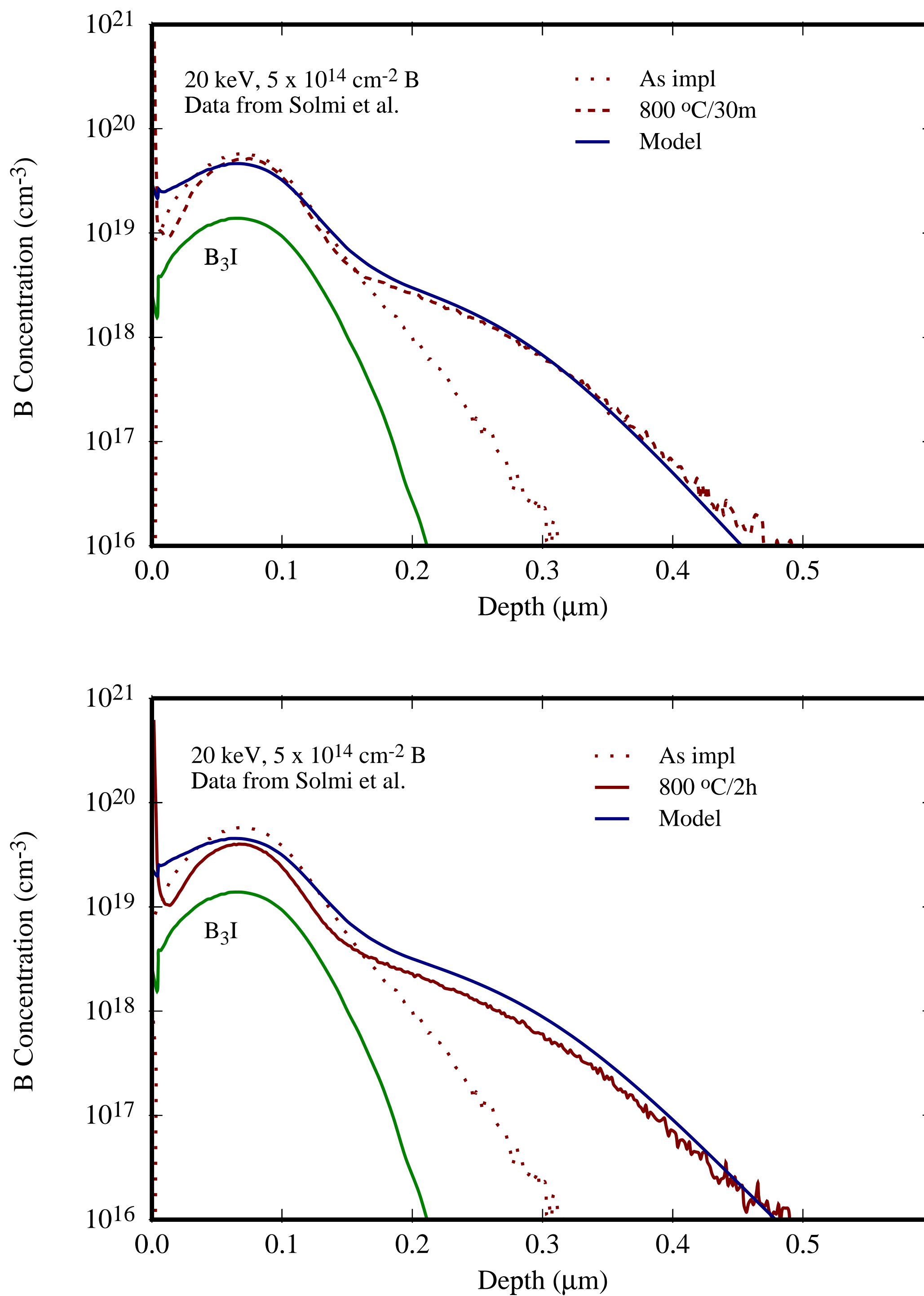

Figure 4.11: Comparison of simple model to data from Solmi *et al.* [90] for a 5×10^{14} cm^{-2} 20 keV B implant annealed at 800°C for (a) 30 min (b) 2 hr.

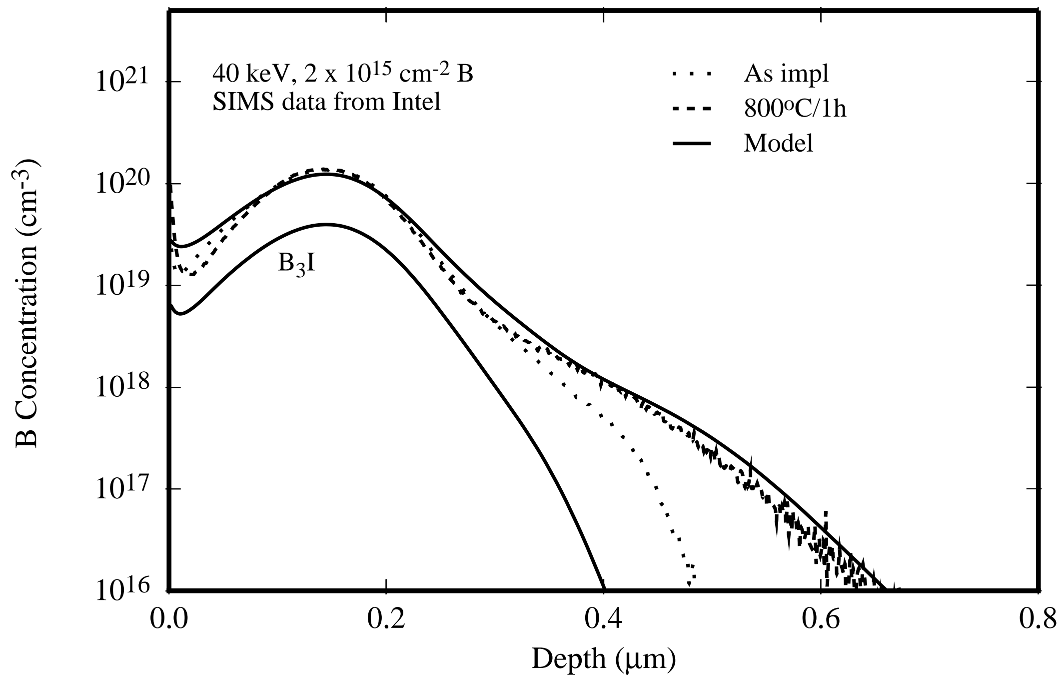

Figure 4.12: Comparison of model to experimental data [44] for a $2 \times 10^{15}\ \mathrm{cm}^{-2}$ 40 keV boron implant after a 60 min anneal at 800°C.

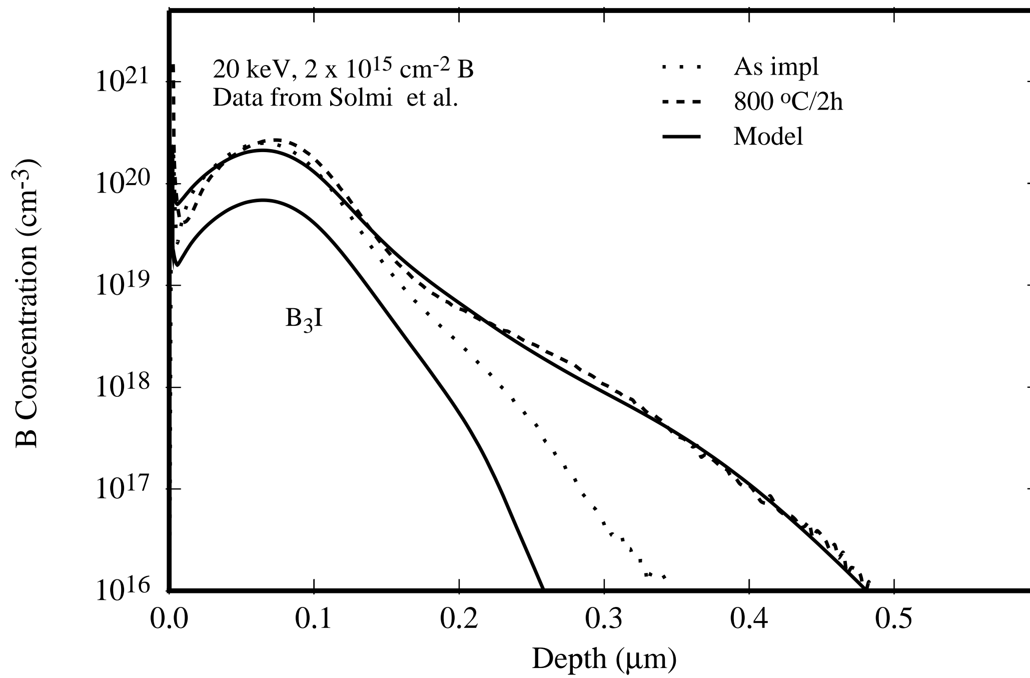

Figure 4.13: Comparison of model to experimental data for a $2 \times 10^{15}\,\text{cm}^{-2}$, 20 keV B implant annealed at 800°C for 2 hrs. SIMS data is from Solmi *et al.* [90]

4.7 Comparison to marker layer experiments

Dopant marker layer experiments have emerged as a very powerful method to probe the underlying mechanisms of dopant/defect interactions. Recently, a unique experiment was performed by Mannino *et al.* [27, 68] to understand the formation of boron interstitial clusters. We first describe their experiment and results in detail. In the next sub-section (4.7.2), we present modeling of this data.

4.7.1 Experimental background

Mannino *et al.* [68] compare post-implant marker layer diffusion data in wafers with and without an additional boron layer closer to the surface. Wafer A contains two boron doped marker layers, located at depths of 900 and 1300 nm, well beyond the implant damage distribution. Wafer B contains in addition a boron box profile located in the depth range 200–500 nm. Both wafers were implanted with 40 keV Si ions to a dose of $2 \times 10^{13}\text{cm}^{-2}$. The damage from this implant evolves into a band of intrinsic interstitial defects-interstitial clusters (ICs) and $\{311\}$ defects close to the projected range of the Si implant, during subsequent annealing as discussed in Sec. 3.3 [27]. For convenience we will refer to this defect band as the "IC band". The boron layer in wafer B was fabricated such that the deep tail of the Si implant damage overlaps with the boron doped box profile (see for example Fig. 4.14). Mannino *et al.* [68] suggest that this overlap causes nucleation of a band of boron interstitial clusters (BICs) at the left-hand box edge, located between the IC band and the diffusion markers. A comparison of marker-layer diffusion in wafers A and B then provides information on the relative stability of BICs and ICs.

Fig. 4.14 shows SIMS profiles obtained by annealing at 600°C for various times. Three major phases of annealing are observed [68]:

- After 1 s anneal, fast diffusion of the left side of the box profile was observed in wafer B. According to Mannino *et al.* [68], "This diffusion evidently takes place at a very early stage of annealing, before the interstitials have had time to diffuse through the doping structure." They suggest it is associated with the displacement of B atoms at low temperature due to capture of free interstitials from the ion collision cascade. "This diffusion phase is accompanied by immobilization (clustering) of a significant fraction of B atoms near the top left side of the box profile." This is noted because of the low boron solubility on the left side ($C_{\mathrm{B}}^{ss} \sim 2 \times 10^{17}\,\text{cm}^{-3}$). "Note that BIC nucleation seems to occur chiefly on the left side of the region (compare with the significant diffusion at the top right corner of the box profile). The narrow band of BICs is stable enough to persist for at least 2 h of further annealing."
- "Rapid marker-layer diffusion occurs in the period 1 s – 15 min, indicating that interstitials diffuse through the entire doping profile within 1 s, and that a very high

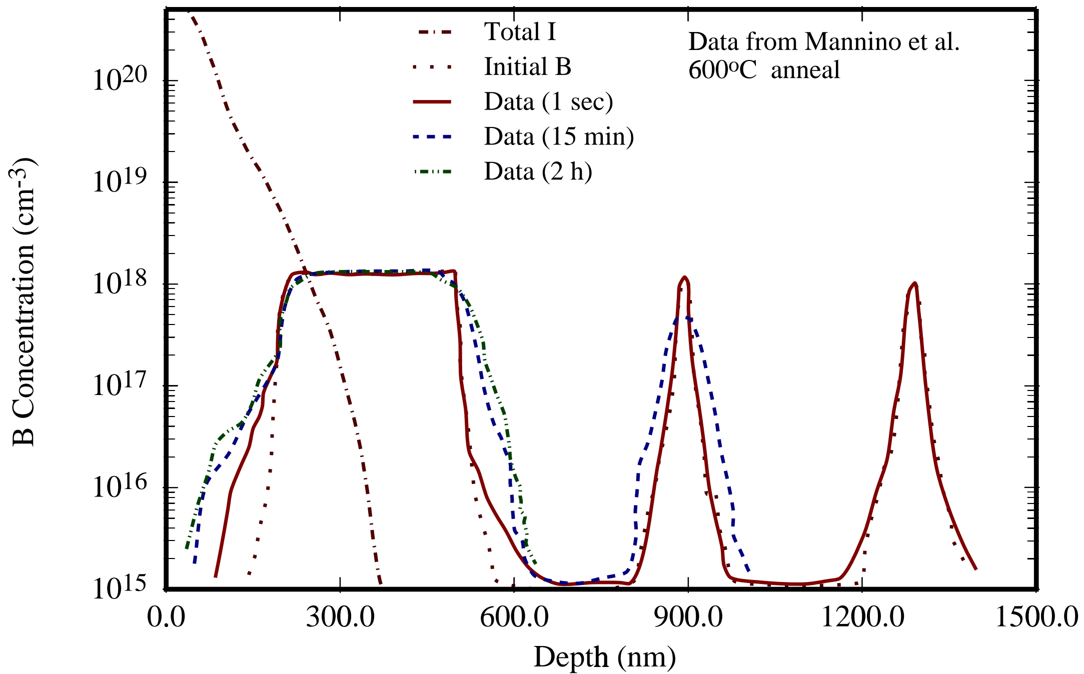

Figure 4.14: SIMS profiles of boron before and after annealing for a range of times at 600°C. Data from Mannino *et al.* [68]. Also plotted is the total damage from the Si implant as calculated by UTMARLOWE [62].

interstitial supersaturation is present during this period. After 1 s the broadening of the shallow and deep marker layers is essentially the same, indicating that there is no longer a significant gradient (and thus no significant flux) of interstitials into the bulk of the wafer. This confirmed that the density of interstitial traps in the material was negligible. The measured marker-layer diffusion in wafer A therefore reflects the interstitial supersaturation, $S_{\rm IC}(t)$, in the region of the IC band. During this time period, the TED measured in wafer B is clearly much lower than in wafer A, but is still extremely high."

- "During the period 15 min – 2 hr the rates of diffusion in wafers A and B are much reduced and appear to have converged to approximately the same value."

Fig. 4.15 shows the supersaturations $S(t)$ for wafers A and B for annealing at 600°C as reported by Mannino *et al.* [68]. "The supersaturation decreases as a function of time in both wafers, but there are obvious differences at short times and low temperatures. For example, at 600°C, the supersaturation in wafer A falls gradually during the period up to 15 min, then drops rapidly. This drop is caused by a ripening transition in the IC band, at

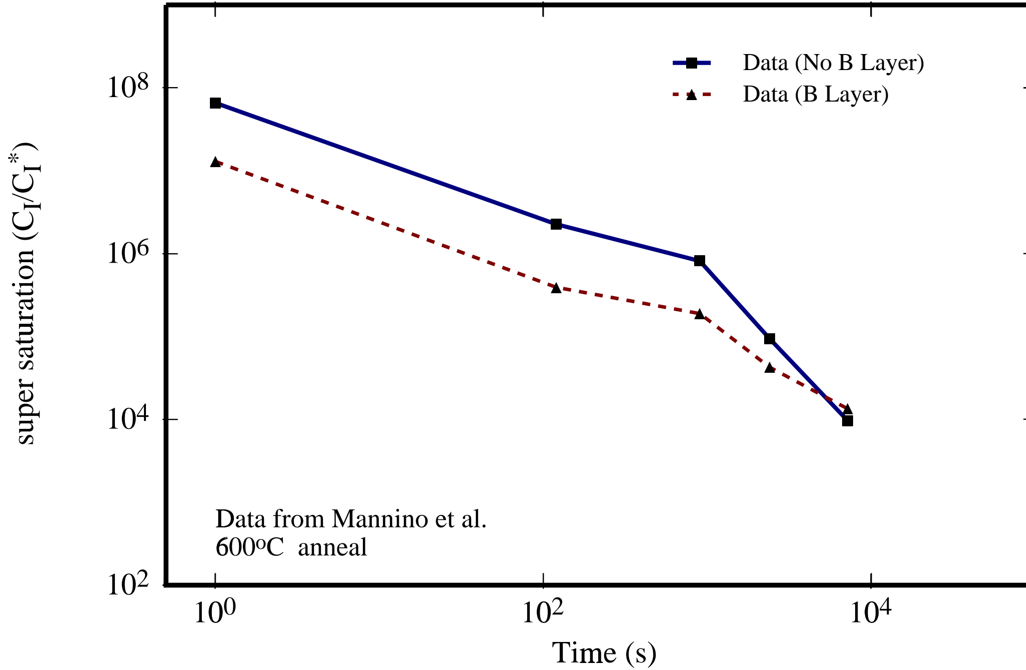

Figure 4.15: Supersaturations observed by the deeper marker layers for Wafer A (No B layer) and Wafer B (B layer) shown with time at 600°C. Data from Mannino *et al.* [68].

a characteristic time τ ($\sim$15 min at 600°C), from small ICs to more stable {311} defects [27]. In wafer B, $S_B(t)$ starts at lower values, the IC-{311} transition appears to be blurred, and at long times $S_B(t)$ converges towards the value in wafer A."

This behavior was explained as follows by Mannino *et al.* [68]. "After IC nucleation and initial growth, S_{IC} rapidly reaches a local equilibrium within the IC band as described in Ref. [27]. Because the intercluster distance within the IC band is orders of magnitude smaller than the distance to the BIC band, this local equilibrium value is unaffected by the existence of the BIC band. Consequently the values of S_{IC} in wafers A and B are the same, and the difference $S_A - S_B$ as observed in Fig. 4.15 can be taken as a direct measure of the decrease in the supersaturation $S(x,t)$ with depth in wafer B. Since, during the diffusion phases, the B-doped regions are transparent to interstitials, the spatial decrease in $S(x,t)$ can only arise from trapping of interstitials in the BIC band." Based on these arguments, they identify $S = S_{IC}$ and $S = S_{BIC}$ where S_{BIC} is the supersaturation at the BIC band. After time $t = \tau$, the value of S_{IC} falls by 1-2 orders of magnitude, to a value lower than that previously existing in the BIC band. The BIC band no longer acts as an interstitial sink, and may even become a weak source. The behavior of $S(x,t)$ before the IC-{311} defect transition is summarized in Fig. 4.16. The change in BIC behavior as a function of S_{IC} shows that once formed the BICs are more stable than the ICs which control TED

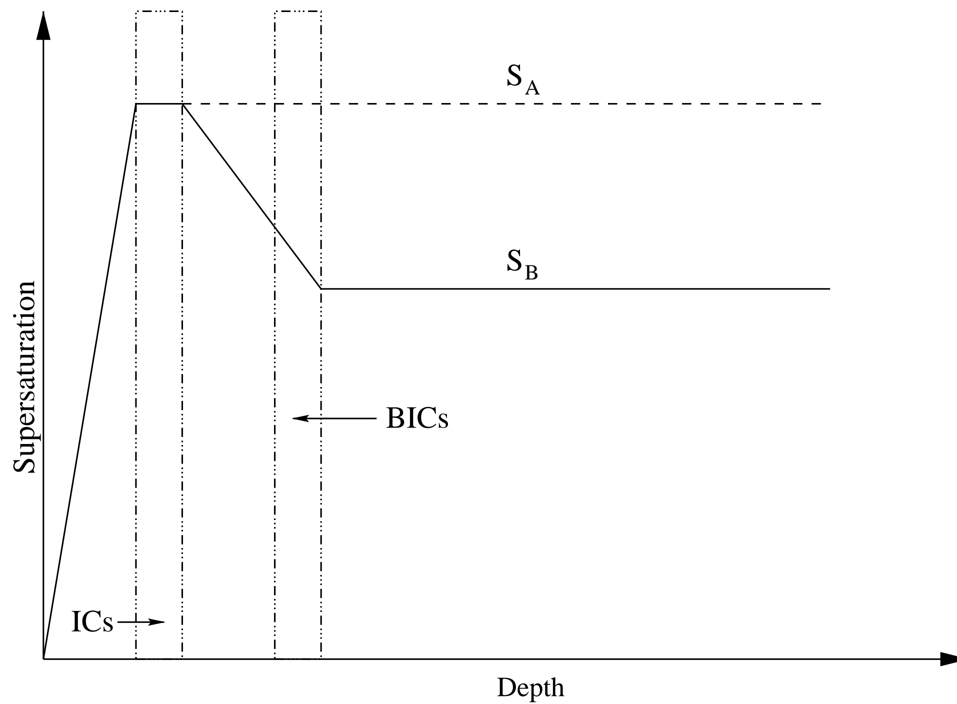

Figure 4.16: The figure sketches the depth and time variation of $S(x,t)$ in wafers A and B after the initial BIC nucleation phase (after Mannino *et al.* [68]).

at short times, and are in fact of comparable stability to $\{311\}$ defects despite their much smaller size.

Since there is no evidence of a formation of a shoulder on the right side of the boron box profile, Mannino *et al.* [68] suggest that the number of clustered B atoms remains roughly constant and the BICs simply become enriched in interstitials. Hence, they support Pelaz's idea that BIC evolution follows an I-rich pathway during TED [82].

4.7.2 Model results

Although, Mannino *et al.* [68] suggest that the interstitials added to the BIC layer may be just getting attached to already nucleated boron clusters, a careful analysis of the phenomenon indicates that this is not the only possibility. These experiments can be explained based on either one or a combination of the following mechanisms:

(i) The decrease in interstitial supersaturation maybe caused by the addition of interstitials to existing clusters to form large interstitial rich clusters (e.g. BI $+$ $(n-1)$I $\Leftrightarrow$ BI_n). Hence during the course of TED these interstitial rich clusters will dissolve and release the trapped interstitials. The dissolution of these interstitial rich boron clusters will control the supersaturation S_B and thus measuring the supersaturation S_B and duration of the

enhancement will yield the stability of these clusters.

(ii) Another possible explanation may be due to the formation large boron clusters like B_4I_4. These are formed by attaching mobile B_i to the existing BI cluster formed during the initial stages of annealing of the implant. This mechanism can be considered as gettering of B_i atoms by the existing BI clusters. If the stability of B_4I_4 is similar to $\{311\}$ defects, then once again the trapped interstitials would be released during the dissolution of $\{311\}$ defects (due to formation of B_4I from B_4I_4).

(iii) It is also possible that new boron clusters are nucleated due to the high interstitial supersaturations prevalent under these conditions. Under this mechanism, boron rich clusters (e.g. B_3I) are formed to trap interstitials. These boron clusters can exist even after the $\{311\}$ defects dissolve, and hence the trapped interstitials may take much longer to be released back into system.

The model by Pelaz *et al.* [82] seems to suggest pathway (ii) as the possible mechanism. However, both (i) and (ii) appear to contradict boron clustering data (see Section. 3.4), which indicated that the ratio of B to I in clusters (at least at 800°C) is greater than 2 to 1. The simpler explanation is to allow nucleation of new boron clusters (pathway (iii)) rather than addition of interstitials to existing clusters. The only limiting criterion is that the number of boron clusters nucleated during the annealing process be relatively low and hence cannot be observed by SIMS on the right side of the box profile. If we now apply our existing model for nucleation of boron clusters via the boron rich path suggested by ab-initio calculations and described in Section 4.2, we observe it is possible to obtain similar results. For these simulations, the full implant cascade from UTMARLOWE [62] is used as initial conditions. Comparison to SIMS is shown in Figs. 4.17 – 4.19. It may be noted that although new boron clusters are nucleated there is no observable shoulder on the right side of the B box profile, whereas there is substantial nucleation on the left side of the box profile. Fig. 4.20 shows comparison to simulated and observed supersaturations. With the exception of underestimating diffusion for the very short times (1s), the model does a good job of predicting the observed behavior, thus establishing it as a plausible mechanism for formation of boron interstitial clusters. Of course, in the absence of long time experimental data probing the stability of the nucleated boron clusters, any combination of the listed pathways can lead to a decrease in the observed experimental supersaturation $S_A - S_B$.

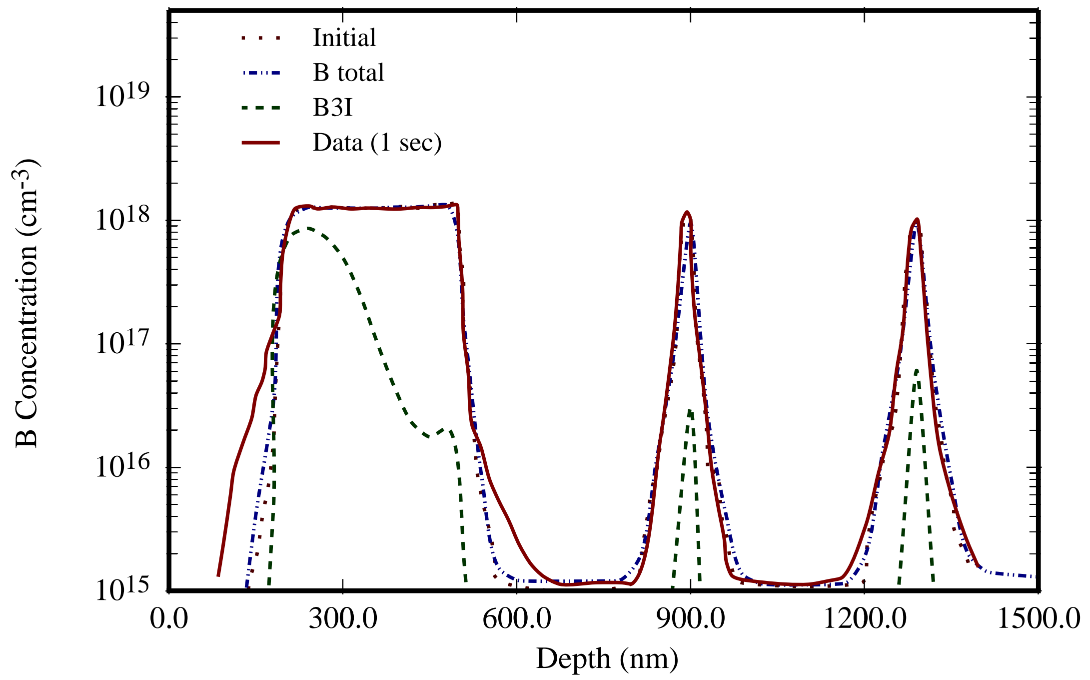

Figure 4.17: SIMS profiles of boron before and after annealing at 600°C for 1 sec compared to experimental SIMS data. Experimental data from Mannino *et al.* [68].

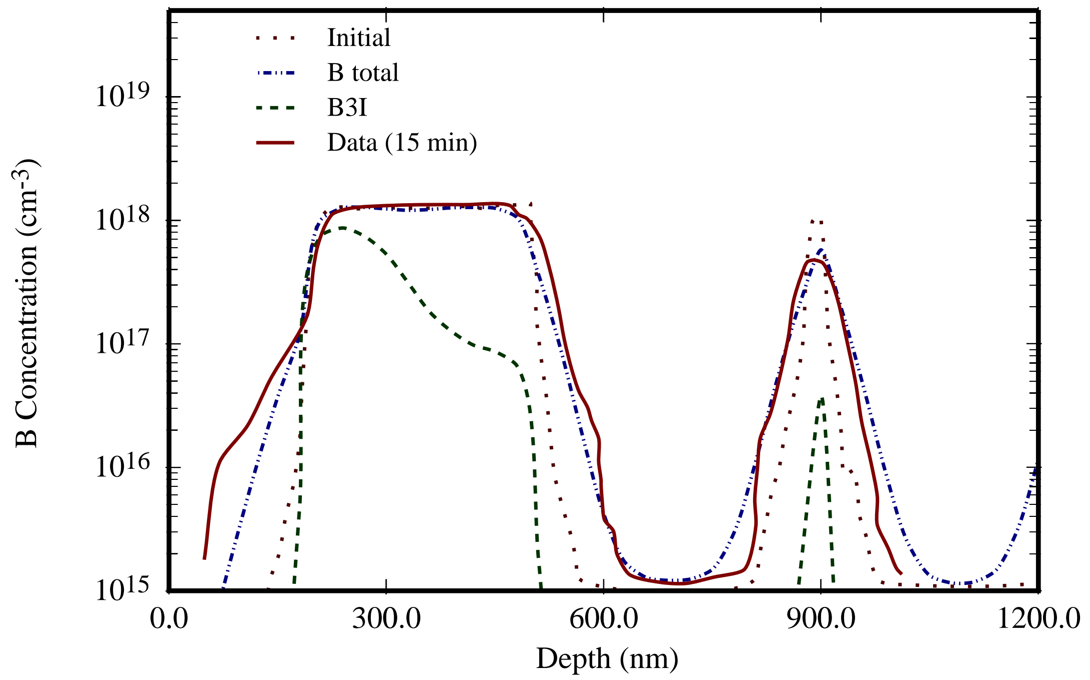

Figure 4.18: SIMS profiles of boron before and after annealing at 600°C for 15 min compared to experimental SIMS data. Experimental data from Mannino *et al.* [68].

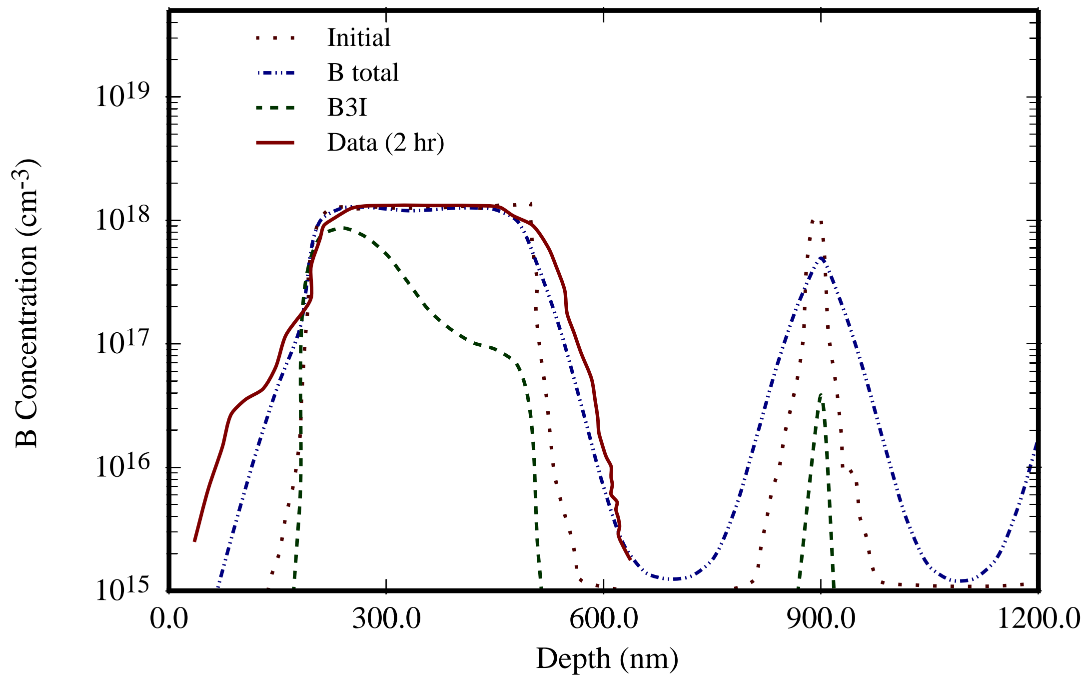

Figure 4.19: SIMS profiles of boron before and after annealing at 600°C for 2 h compared to experimental SIMS data. Experimental data from Mannino *et al.* [68].

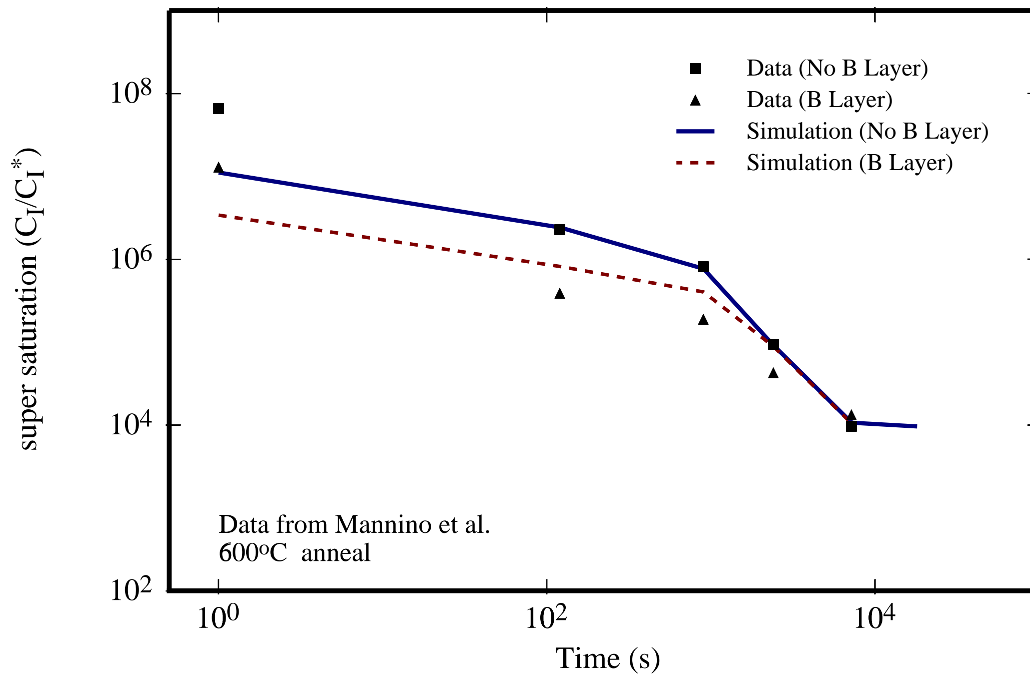

Figure 4.20: Simulated supersaturations compared to experimentally observed values at 600°C. Experimental data from Mannino *et al.* [68].

4.8 Comparison to electrical activation data

In previous sections, we were concerned mostly with matching the chemical concentration profiles. However, predicting electrical activation is essential for the effectiveness of process modeling. Thus, we now look at modeling of boron electrical activation.

For modeling boron deactivation, we consider the clusters BI_2, B_2I_2, B_2I, B_3I [18, 20]. As discussed in Section 4.4, based on charged defect calculations, Lenosky *et al.* [64] conclude that the dominant charge states for these clusters are $(BI_2)^+$, $(B_2I_2)^0$, $(B_2I)^0$ and $(B_3I)^-$. However, since electrical activation data indicates dominant clusters are neutral at room temperature, we assume the dominant cluster B_3I to be neutral $(B_3I)^0$.

A temperature ramp-up of 50°C/s for the RTA and 1°C/s for the furnace anneals was used for the simulations. We compare our model to isochronal annealing results from Seidel *et al.* [87]. In these experiments, the active fraction of boron is measured as a function of temperature for a fixed annealing time. Shown in Fig. 4.21 is a match to reverse annealing profiles from Seidel *et al.* [87] for two different implant doses. In these experiments, boron was implanted at 150 keV and furnace annealed for 30 mins. At low temperatures (500 – 700°C, as shown in Fig. 4.21), boron clusters are stable and thus most of the boron is inactive. The activation initially decreases with temperatures as these clusters form. At higher temperatures ($>$ 750°C), these boron clusters dissolve, and thus the active fraction increases as a function of temperature. As shown in Fig. 4.21, our model captures the main features of the deactivation/activation process for different doses. This is also exhibited for higher doses, where the clustering behavior is stronger, leading to lower activation.

We further compare our model to SRP and SIMS data from Pelaz *et al.* Fig. 4.22 shows the evolution of the active fraction compared to experimental data [84]. Clusters form during the ramp-up to 800°C, reducing the active fraction quickly. During further annealing, interstitial supersaturation drops rapidly subsequent to dissolution of interstitial defects. This reduces the stability of boron interstitial clusters and leads to an increase in active boron fraction with time as shown in Fig. 4.22. Note that the dissolution process needs free interstitials for the formation of the intermediate species B_3I_2, while dissolving from B_3I to B_2I. Thus activation of boron as seen in Fig. 4.22 is a slow process once these clusters are formed. Shown in Fig. 4.23 is comparison to a 2×10^{14} cm^{-2} B implant data from Pelaz *et al.* [84] spike annealed at 800°C. Similarly we find good match to experimental data for longer anneal times as shown in Fig. 4.24.

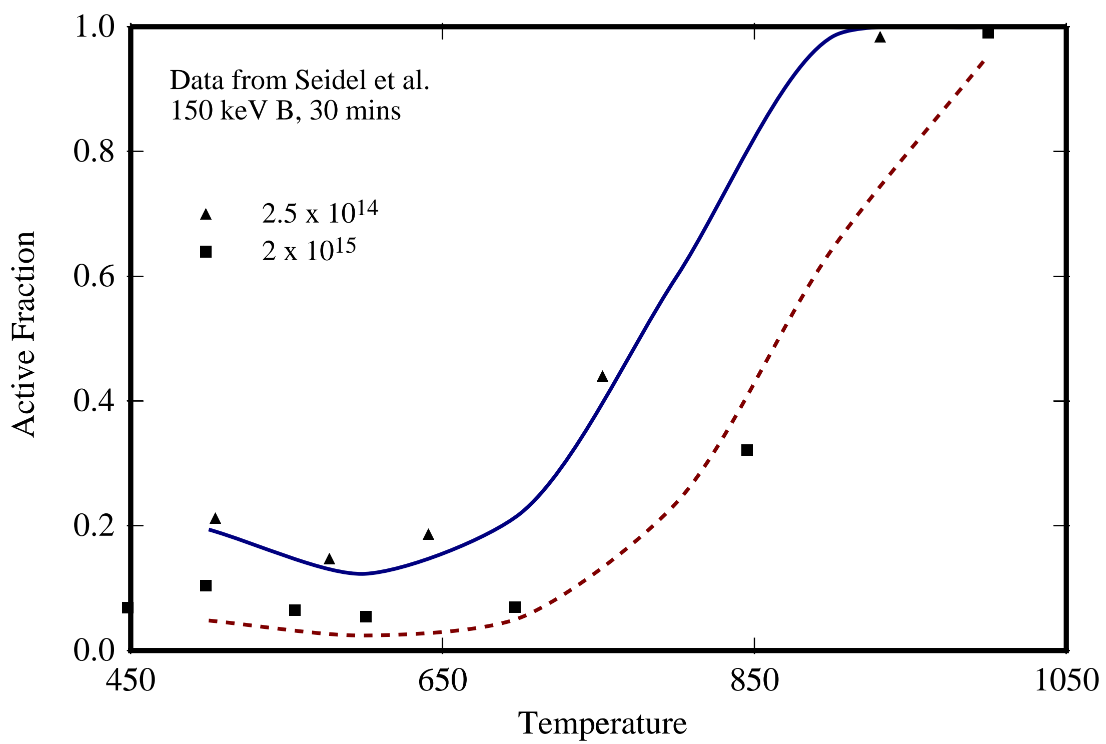

Figure 4.21: Comparison of experimentally-measured active fraction [87] to model for 150 keV, 2×10^{14} cm^{-2} and 2×10^{15} cm^{-2} boron implants annealed for 30 min. at various temperatures. Lines represent model predictions, and symbols represent data.

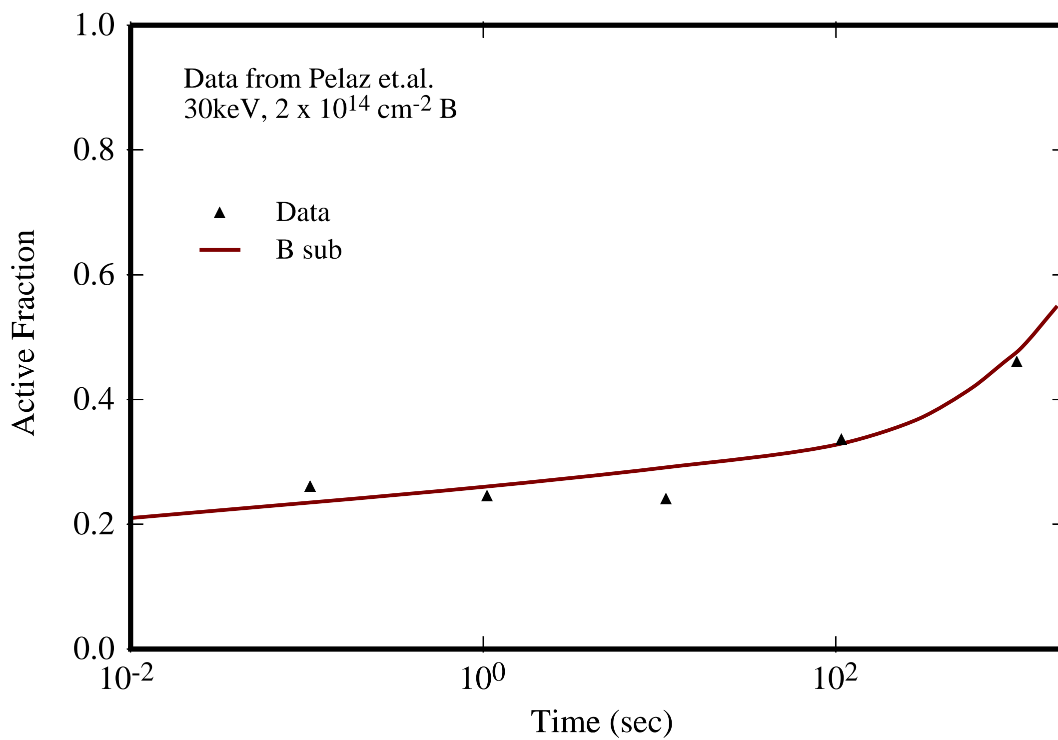

Figure 4.22: Comparison of simulated and experimentally measured active fraction for a 2×10^{14} cm^{-2} boron implant annealed at 800°C. Data from Pelaz *et al.* [84].

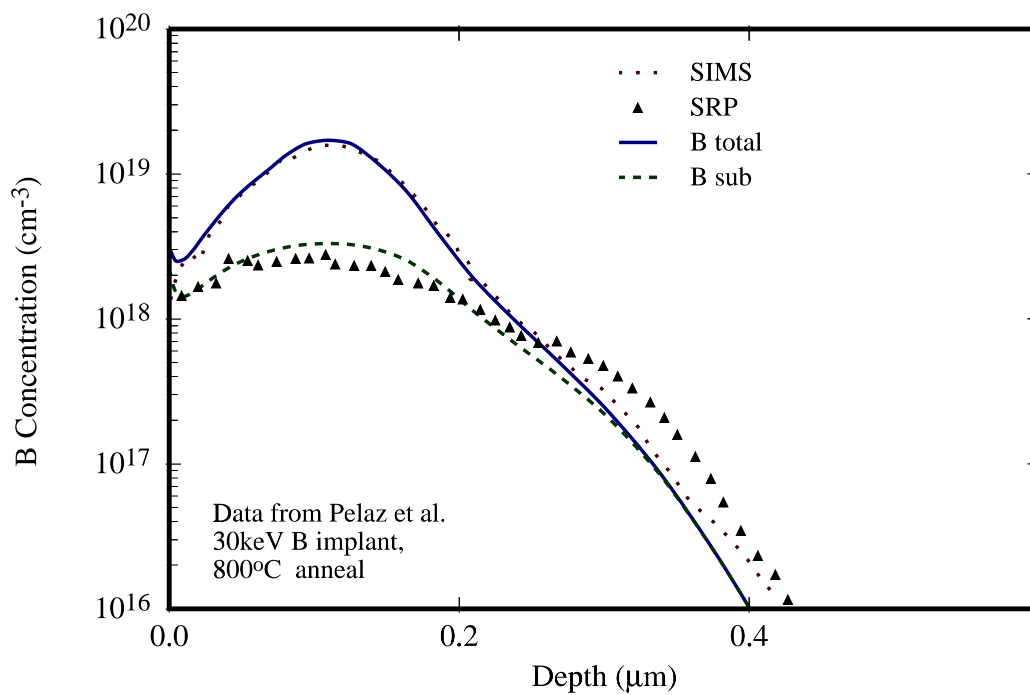

Figure 4.23: Comparison of simulation with SIMS and SRP data from Pelaz *et al.* [84] for a 2×10^{14} cm^{-2} implant annealed at 800°C for 1 s. Note that most of the boron is already in clusters.

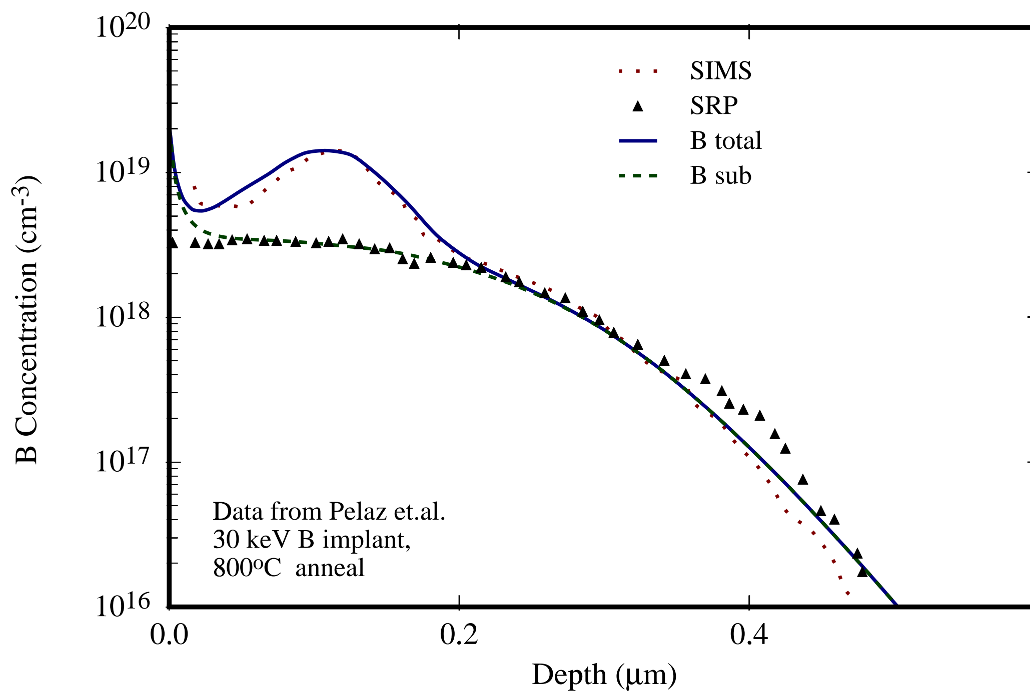

Figure 4.24: Comparison of simulation with SIMS and SRP data from Pelaz *et al.* [84] for a 2×10^{14} cm^{-2} implant annealed at 800°C for 1000 s.

4.9 Summary

We have found that consideration of either a finite set of discrete clusters or a moment-based model such as KPM can match experimental data satisfactorily for medium doses. For medium and low energy boron implants, we have developed a simple cluster model for modeling boron interstitial clusters. This system was derived from a multi-cluster model based on *ab-initio* calculations performed at Lawrence Livermore National Labs [102]. Based on analysis of cluster kinetics and energetics, we are able to match the results of the full multi-cluster model, while reducing the number of cluster continuity equations from ten to just two. The resulting model clearly illuminates the critical processes involved in boron clustering. Despite its simplicity, the model accurately describes boron clustering and anomalous diffusion over a range of experimental conditions. This model also yielded correct qualitative behavior in matching boron marker layer experiments.

We also found that we can model boron deactivation kinetics during low and moderate temperature annealing after implantation. The model is able to capture the kinetics of the deactivation and activation processes and thus predict electrical activation during annealing over a wide range of temperatures and times.

Chapter 5

Ultra Shallow Boron Junctions

According to the International Technology Roadmap for Semiconductors [1], it is necessary to produce highly activated and shallow junctions for continued device scaling. For example, it is estimated that devices produced in the year 2006 with gate lengths of 100 nm will have sub-40 nm junction depths. However, apparently new phenomena have been observed under the far from equilibrium conditions necessary for forming these junctions. In this chapter, we show that by careful consideration of models developed in Chapter 4 for much deeper junctions, the dependence of junction depth on processing conditions can be understood for ultra-shallow junctions as well.

5.1 Rapid thermal soak anneals

Transient enhanced diffusion (TED) has been the dominant effect in determining junction depths for the past decade and will continue to be important. However, the use of ultra-low energy implants and short time, high temperature RTP annealing has greatly diminished the importance of TED in ultra-shallow boron junctions. Reducing the implant energy is particularly effective as it puts the damage closer to the surface where it can be more readily annihilated, thus reducing the time period over which TED is present. Recent work [2, 3, 7] shows that TED can be nearly eliminated for implant energies below about 1 keV. However, the reduction in TED has revealed other effects controlling boron diffusivity (and thus junction depth) for ultra-shallow profiles. This section focuses on understanding and modeling of these effects.

Agarwal *et al.* [2, 3, 7] found that although silicon implants at 1 keV and below resulted in normal marker layer diffusion, boron implants with similar doses and ranges led to significantly ($\sim 4\times$) enhanced diffusion. They termed this effect BED (boron enhanced diffusion) and associated it with the formation of a boron-rich phase near the surface. However, applying the models developed in earlier sections to this data we find a good match to this data as shown in Fig. 5.1. The solid solubility as evident in the data and

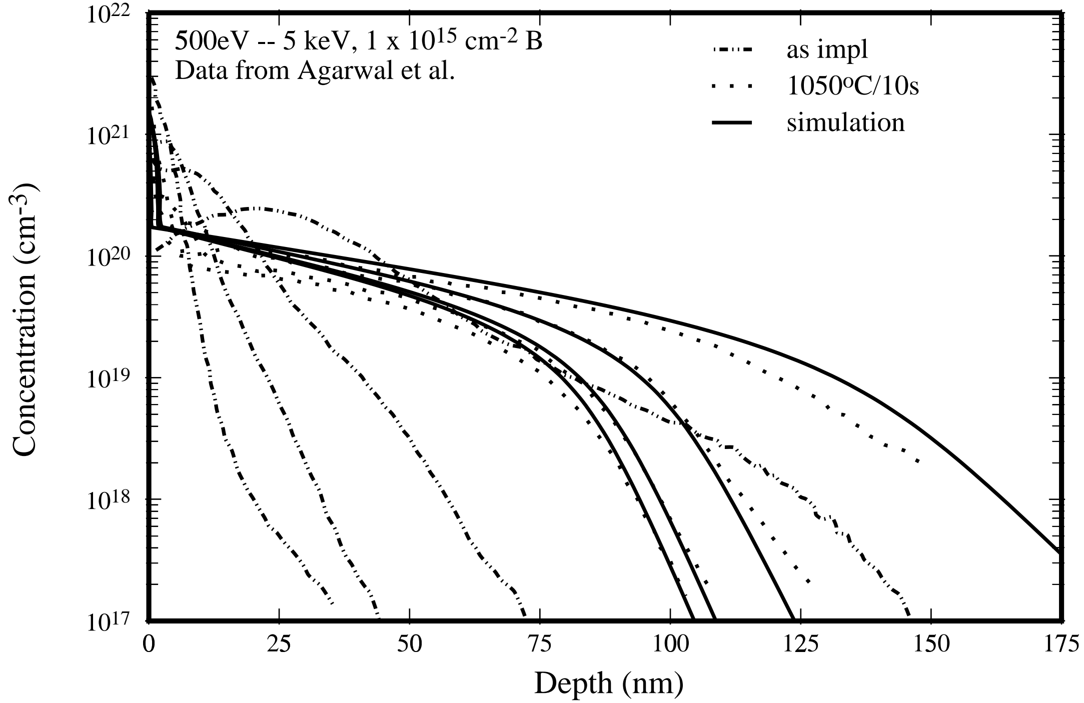

Figure 5.1: Simulated and measured boron profiles following 10^{15}cm^{-3} boron implants at 0.5 to 5 keV. Data from Agarwal *et al.* [3].

simulations was modeled using a solid solubility model as discussed in Section 4.6. As can be seen, the simulations accurately predict the observed boron junction depths and/or marker layer broadening, not only for implants, but also for boron deposited on the surface via MBE (Figs. 5.2, 5.3). There is indeed significantly enhanced diffusion in this system (Fig. 5.4), driven by the same pair injection process which leads to enhanced tail diffusion as discussed in Section 2.5.

It was noted by Agarwal *et al.* [2, 3, 7] that there was a slightly greater diffusion enhancement for higher temperatures (e.g., factor of 3 at 950°C versus 4 at 1050°C), while coupled diffusion effects give smaller enhancements at higher temperatures. For coupled diffusion effects, the interstitial super-saturation (and thus diffusion enhancement) in the tail region depends on the balance between interstitial injection, which is proportional to boron diffusion, and interstitial diffusion back to the surface, which is proportional to the self-diffusion coefficient. Since boron diffusion has a smaller activation energy (and thus smaller increase with temperature) than the self-diffusion, smaller super-saturations are expected at higher temperatures for the same boron surface concentration. However, for the high boron concentrations in these experiments, the surface concentration is not constant due to the changes in the solubility with temperature. We find from our simulations that

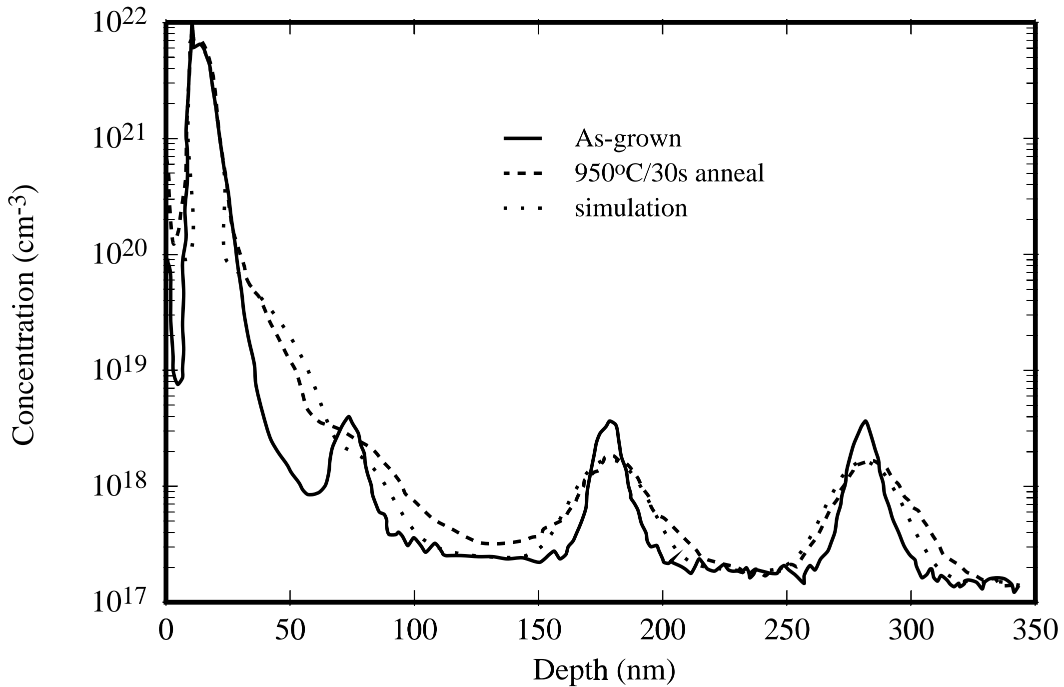

Figure 5.2: Comparison between simulated and measured broadening of boron delta-doped super-lattices in the presence of an MBE-deposited boron layer and annealing at 950°C for 10 sec. Data from Agarwal *et al.* [3].

the increased solubility at higher temperatures approximately compensates for the changes in the boron diffusion to self-diffusion ratio, leading to very little change in enhancement with temperature. As can be seen from Figs. 5.1–5.4, our simulations accurately predict the experimental behavior. Fig. 5.4 shows the change in diffusion enhancement versus implant dose. Agarwal *et al.* [2, 3, 7] suggested that the rather abrupt increase in diffusion enhancement with dose might be due to the formation of a boride phase. However, it can be seen that the dose dependence is reasonably predicted simply based on coupled diffusion as the increased boron concentration with dose leads to larger fluxes of BI pairs into the substrate.

More recently, Agarwal *et al.* presented new experimental results on the temperature and time dependence of BED, again using an MBE deposited layer [6]. They found that isochronal 10 s anneals show a B marker layer diffusion enhancement that increases with temperature to a peak value and then decreases. Samples annealed at 800°C do not show any measurable enhancement while samples preannealed at 1050°C and then annealed at 800°C show a pronounced enhancement. As they agree, such behavior cannot be explained based only on coupled diffusion effects. This is because coupled diffusion enhancements increase with decreasing temperature. For example, the diffusion enhancement (S) from

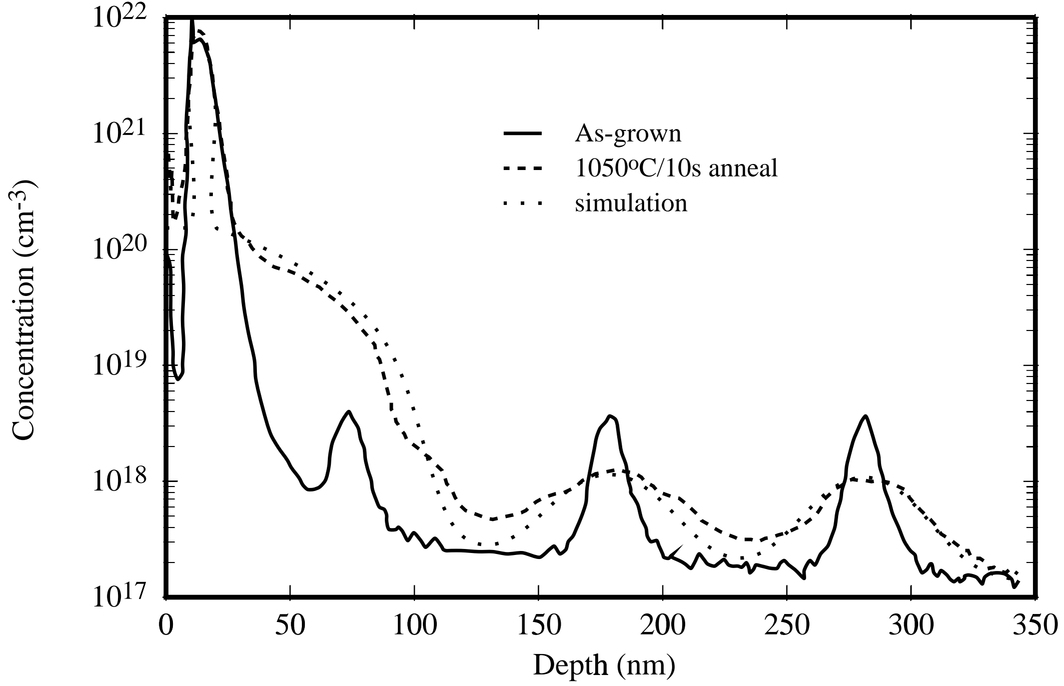

Figure 5.3: Comparison between simulated and measured broadening of boron delta-doped super-lattices in the presence of an MBE-deposited boron layer and annealing at 1050°C for 10 sec. Data from Agarwal *et al.* [3].

coupled diffusion can be estimated to be around:

$$S = \frac{D_{\mathrm{B}} C_{\mathrm{ss}}^{\mathrm{B}} (p/n_i)}{D_{\mathrm{I}} C_{\mathrm{I}}^*} \propto \exp\left(\frac{0.7}{kT}\right) \tag{5.1}$$

The observations can, however, be explained by including the formation of boron clusters at the lower temperatures. For example, using the boron interstitial cluster model from previous chapter, we find small clusters (such as B_3I) form at lower temperatures, thus reducing the effective solubility of boron. This decreases the measured enhancements at lower temperatures. Increasing the temperature leads to dissolution of these clusters and hence more pronounced coupled diffusion effects. Thus, as shown in Fig. 5.5, it is possible to explain the behavior observed by Agarwal *et al.* [6], at least qualitatively. The high temperature preanneal leads to formation of larger boron precipitates (solubility phase). It will also dissolve any of the as-grown smaller clusters. Hence during the subsquent 800°C anneal the driving force for the formation of smaller clusters is much lower (since solubility is now governed by the solubility phase), while much more enhancement is observed in the sample with the 1050°C preanneal in agreement with experiments.

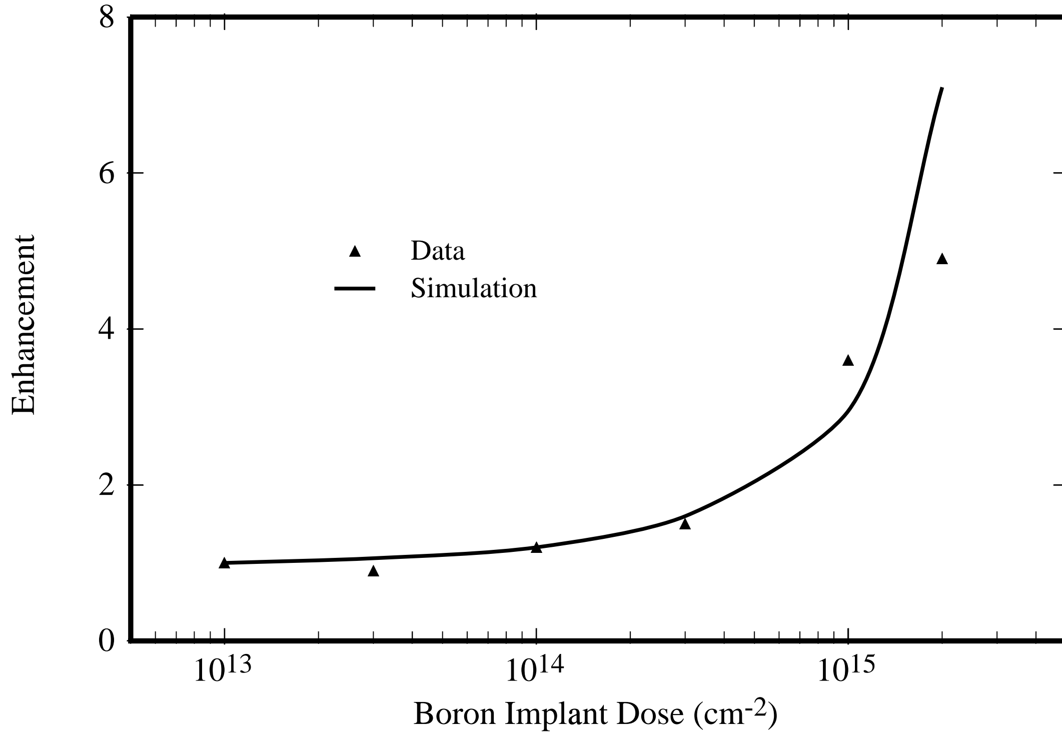

Figure 5.4: Predicted and measured diffusivity enhancement of boron marker layers for various 0.5 keV boron implant doses and annealing at 1050°C for 10 sec. Data from Agarwal *et al.* [2].

Agarwal *et al.* [6] also presented the time dependence of these enhancements. They found the diffusivity enhancement lasts for over 100 s at 950 and 1000°C and increases for up to 30 s at 1050°C (e.g. 3× at 3 s to 5.5× at 30 s during a 1050°C anneal). Although our simulations predict roughly constant enhancements over time at lower temperatures consistent with the experimental observations, we find it is not possible to predict the increasing enhancement observed at 1050°C. Note that the overall enhancement observed at 1050°C is also significantly higher than the prediction of our model (Fig. 5.5). This suggests that the point defect concentrations may be affected by changes in the boride phase at higher temperatures. The implications of the formation and subsequent dissolution of the boride phase is thus not fully understood and remain under active research.

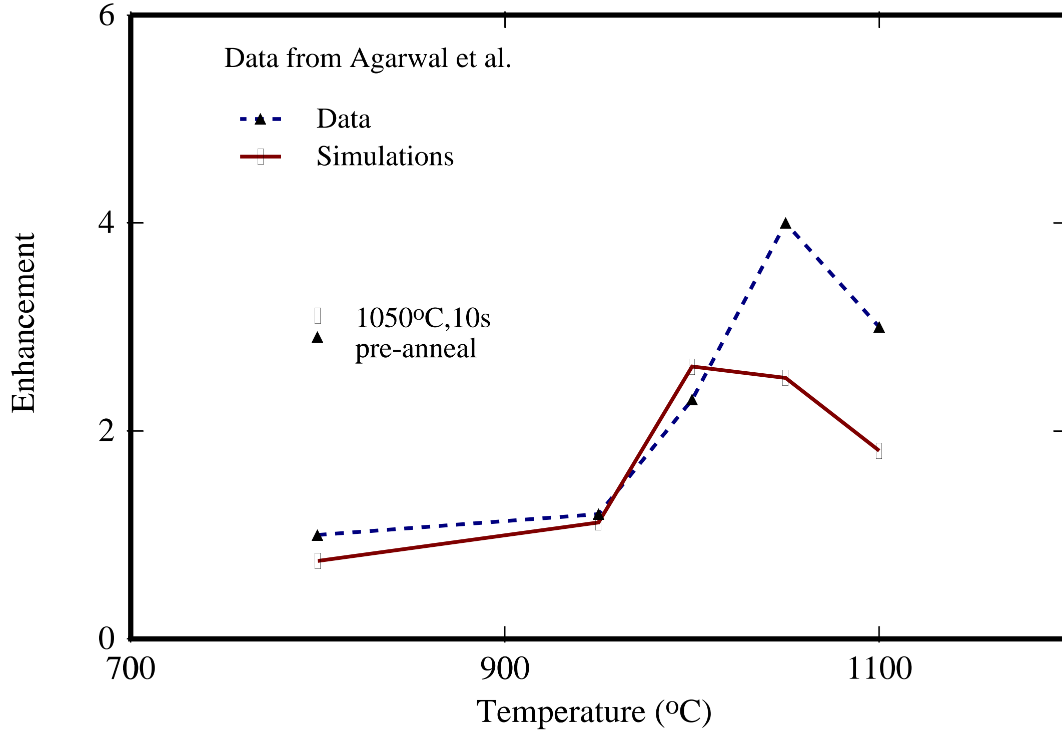

Figure 5.5: Temperature dependence of MBE marker layers as reported by Agarwal *et al.* [6] and compared to simulations. As observed at 800°C there is no enhancement, however a preanneal at 1050°C maintains an enhancement. The enhancements at higher temperature are plotted for 10 s.

5.2 Spike anneals

The achievement of sub-40nm ultra-shallow source/drain extensions requires low energy implants along with fast spike anneals to minimize diffusion. The advantage of using faster ramp-up rate can be understood from a simple analysis of Transient Enhanced Diffusion (TED). Based on the experimental observations discussed in Section 3.3, it is possible to come up with a simple model for the estimation of TED effects. If the formation of $\{311\}$ defects is associated with an effective interstitial solubility C_{I}^{311} which is maintained throughout the growth/dissolution of these defects, then the flux of interstitials to the surface can be approximated by:

$$J_{\mathrm{I}}^{\mathrm{TED}} \cong D_{\mathrm{I}} C_{\mathrm{I}}^{311} / R_p, \tag{5.2}$$

where R_p is the average depth of net interstitial distribution (approximately the implant range). The period over which TED lasts then is just:

$$\tau_{\text{TED}} = \frac{Q_{\text{I}}}{J_{\text{I}}^{\text{TED}}} = \frac{Q_{\text{I}} R_p}{D_{\text{I}} C_{\text{I}}^{311}}, \tag{5.3}$$

where the net excess implant dose $Q_{\text{I}} = NQ_{\text{implant}}$ based on a "$+N$" model. During TED, the interstitial supersaturation is $C_{\text{I}}^{311}/C_{\text{I}}^{*}$, so the amount of excess diffusion expected during TED is given by:

$$(Dt)_{\text{TED}} = D_{\text{A}}^{*} \tau_{\text{TED}} f_{\text{I}} \frac{C_{\text{I}}^{311}}{C_{\text{I}}^{*}} = \frac{D_{\text{A}}^{*} f_{\text{I}} Q_{\text{I}} R_p}{D_{\text{I}} C_{\text{I}}^{*}}, \tag{5.4}$$

where D_{A}^{*} is the dopant diffusivity under equilibrium conditions. Note that the activation energy of boron diffusion ($\sim$ 3.6 eV) is less than that of self-diffusion via interstitials ($D_{\text{I}} C_{\text{I}}^{*} \sim 4.8$ eV), so that diffusion due to TED is actually decreased as the annealing temperature is increased (as long as sufficient time is allowed for completion of TED). It is also notable that TED depends primarily on the $D_{\text{I}} C_{\text{I}}^{*}$ product rather than the individual terms. Hence, using a higher ramp-up rate is more effective in producing shallower junctions. Thus it is tempting to produce faster and faster ramp-up furnaces to minimize diffusion while maintaining good activation.

Although TED effects reduce with implant energy, the achievable reduction in junction depth with increasing ramp-up rate has been found to decrease with increasing implant energy [4, 30]. Sub-1keV implants show a more pronounced decrease in junction depth with increase in ramp rates, while the reduction in junction depth for higher energy implants has been found to saturate for larger ramp rates. In this section, we apply the models developed in earlier chapters to understand and model the effect of RTP annealing cycle on junction behavior so that RTP processes can be optimized for shallow, low resistance junctions.

Fig. 5.6 shows a schematic illustration of the temperature versus time profile during a ramp-up. For the simulations, a linear ramp-up is assumed. After the lamps are turned off, it is assumed that the wafer temperature drops chiefly by radiating heat to the furnace walls, and hence the ramp-down rate decreases at lower temperatures. During the cool down, the heat loss is proportional to T^4, so:

$$T = T_f \left(1 - \frac{3tR_{\text{cool}}}{T_f}\right)^{-0.33} \tag{5.5}$$

where, T_f is the maximum attained temperature, R_{cool} is the cooling rate (K/s) at T_f (K) and t is time elapsed after reaching T_f.

Since the experiments considered were performed under low ambient oxygen levels, oxidation enhanced and retarded diffusion was modeled as in previous work [34]. For low oxygen partial pressures, diffusion is retarded rather than enhanced [31]. At 1050°C, a

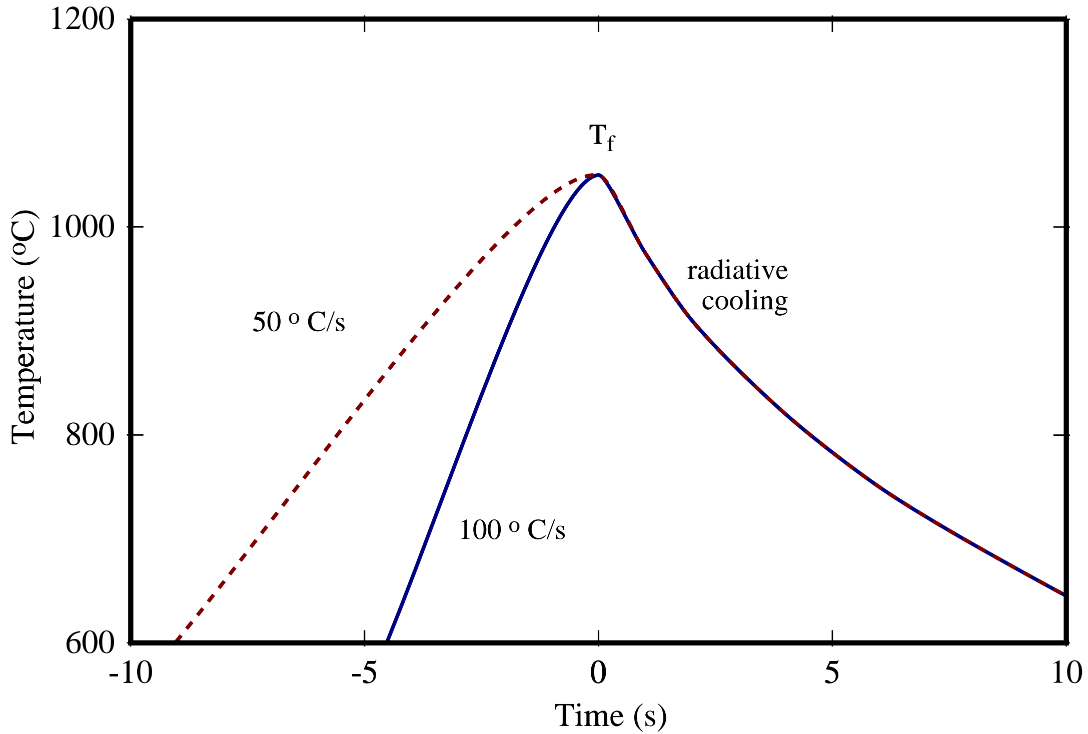

Figure 5.6: Temperature versus time profiles used for the simulations. Ramp-up is modeled as linear whereas cool down is radiative.

33ppm oxygen partial pressure and 16 Å initial oxide film results in C_I at the interface equal to about $0.2C_\mathrm{I}^*$. Simulations of the model thus including the ORD effect is compared to data from Lerch *et al.* [65] in Fig. 5.7.

First we look at the qualitative behavior of junction movement due to spike anneals for ultra low energy B implants. The simulations predict a reduced effect of ramp rate on x_j (as seen experimentally) [5, 30] and saturation in the junction depth with increasing ramp-up rates (Fig. 5.8). This saturation occurs at larger ramp rates for lower energy implants. For higher energies, the faster ramp-ups retain more of the interstitial clusters and more of the TED actually occurs during the ramp-down, thus negating any reduction possible due to the faster ramp-up. In fact, for higher energies, junction depth increases slightly with increased ramp rates, as TED persists to lower temperatures during the ramp-down. For very fast ramp-up rates, the ramp-up is only a small fraction of the total thermal budget, and hence the cooling rate dominates the total junction movement. Thus, as shown in Fig. 5.9, higher ramp-down rates are effective in reducing junction depth, if the ramp-up rate is fast enough that TED is not completed. Figs. 5.10 – 5.12 shows comparison to RTP anneals from Downey *et al.* [30] using two different ramp-up rate for three different

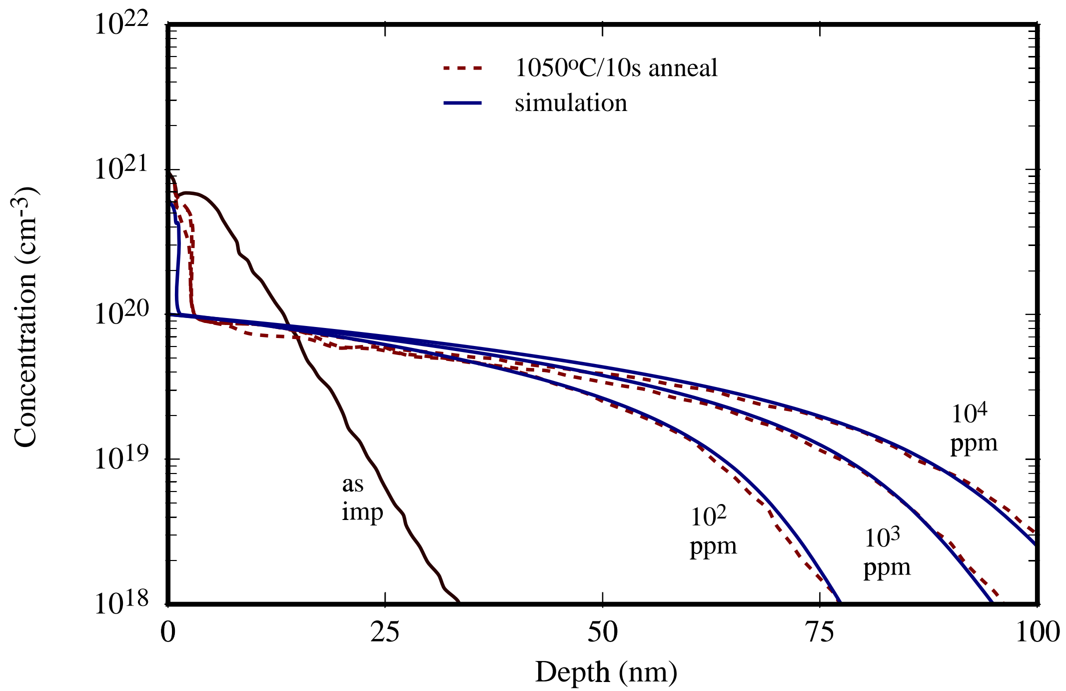

Figure 5.7: Boron profiles versus oxygen partial pressure for 1keV, 10^{15}cm^{-2} boron implants annealed 10 s at 1050°C (Lerch *et al.* [65]) are shown along with simulations matched to these profiles by varying the surface interstitial concentration.

implant energies. The simulations give a good match to the observed boron junction depths across the spectrum of conditions [21].

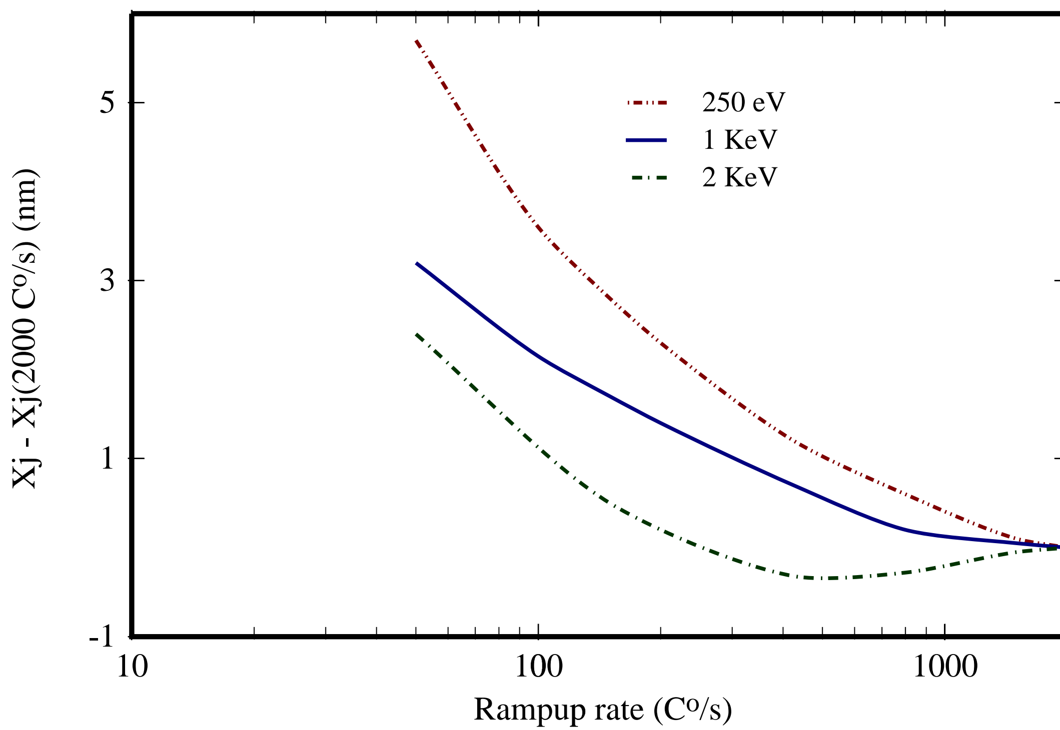

Figure 5.8: The effect of ramp rate on reduction in junction depth for $1 \times 10^{15}\text{cm}^{-2}$ B implants following 1050°C spike anneals. The difference in junction depth (x_j@5×10^{18} cm^{-3}) relative to a ramp-up rate of 2000°C/s is shown for various implant energies.

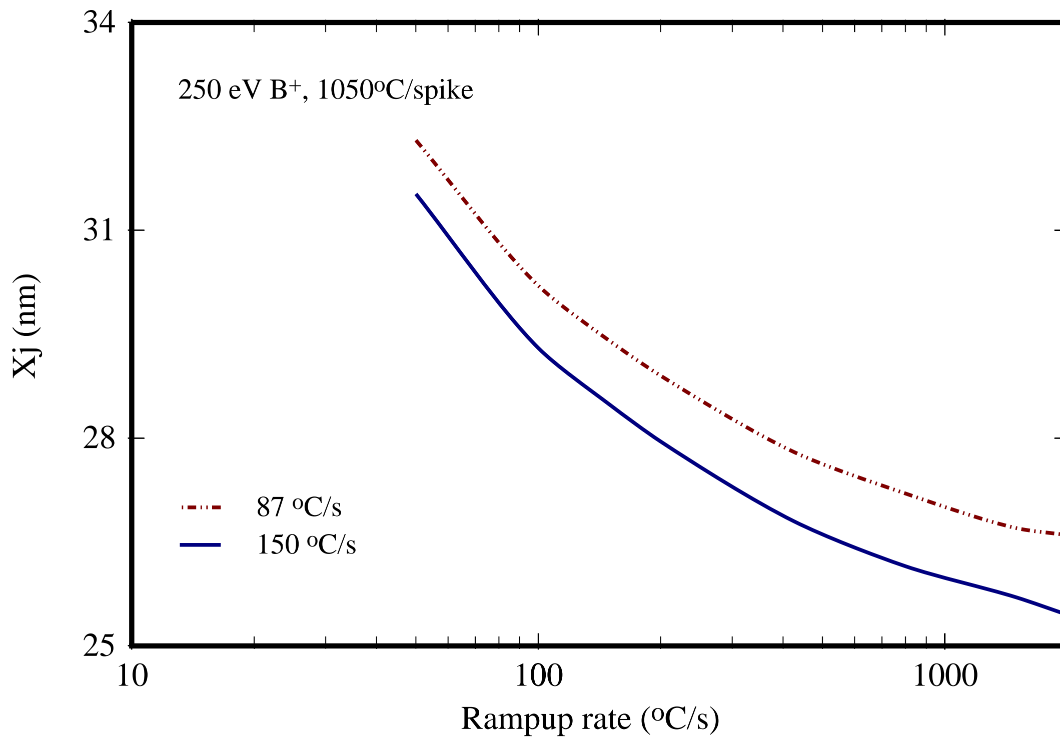

Figure 5.9: The effect of ramp rate on reduction in junction depth for 1×10^{15}cm^{-2} B implants following 1050°C spike anneals. The effect of changing the cooling rate is shown. Note that increasing the ramp-down rate gives a greater junction depth reduction for higher ramp-up rates, since more of the TED then occurs during ramp-down.

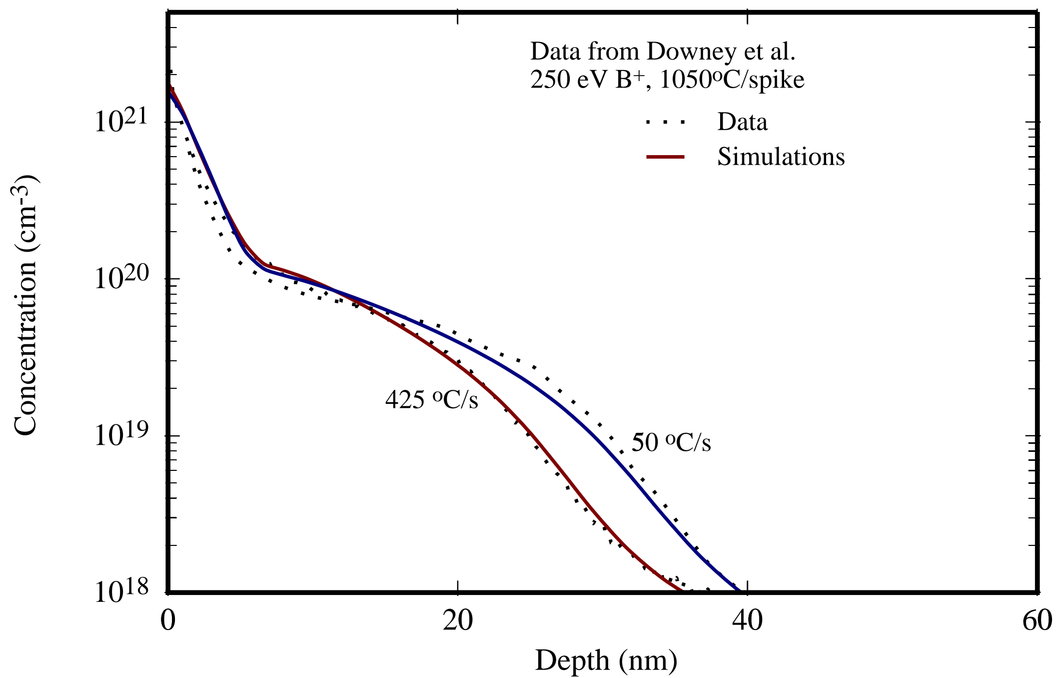

Figure 5.10: Comparison of simulation and experiment for a $1 \times 10^{15}\mathrm{cm}^{-2}$ 250 eV B^+ implant for a 1050°C spike anneal in 33 ppm O_2 in N_2 ambient. Ramp-up rates are 50°C/s and 425°C/s, and initial ramp-down rate is 87°C/s. Data from Downey *et al.* [30].

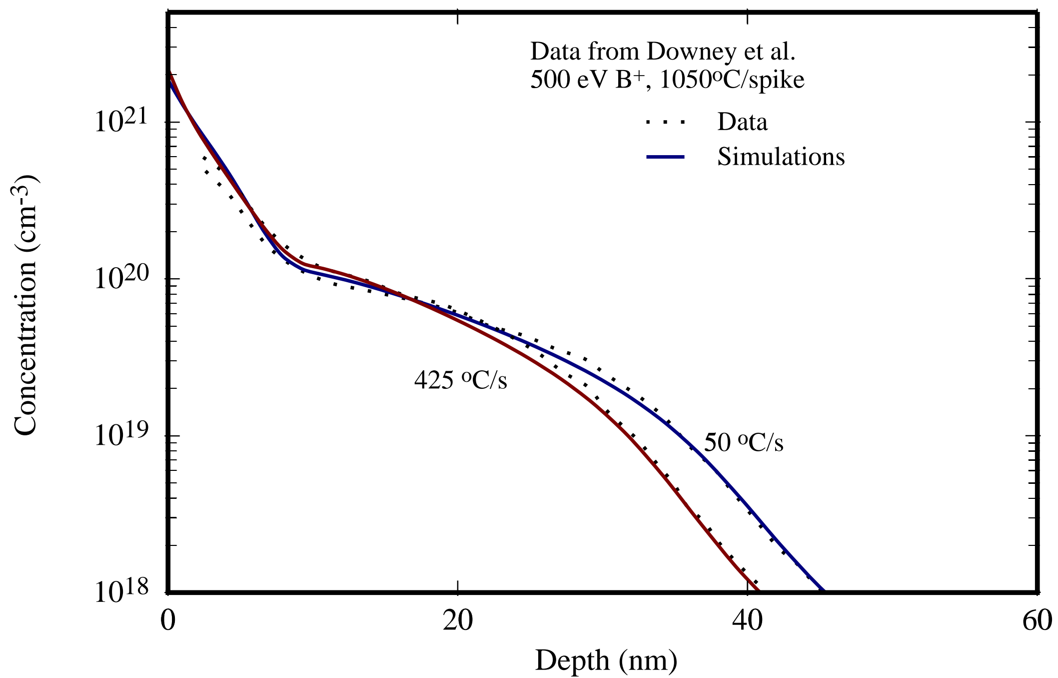

Figure 5.11: Comparison of simulation and experiment for a 1×10^{15}cm^{-2} 500 eV B^+ implant for a 1050°C spike anneal in 33 ppm O_2 in N_2 ambient. Ramp-up rates are 50°C/s and 425°C/s, and initial ramp-down rate is 87°C/s. Data from Downey *et al.* [30].

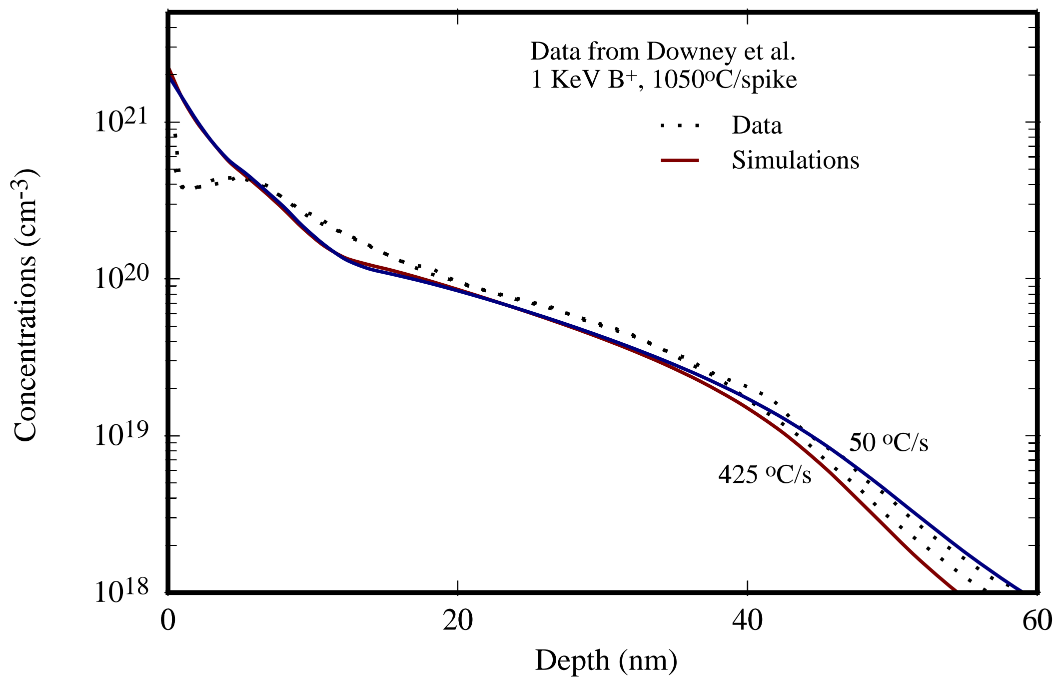

Figure 5.12: Comparison of simulation and experiment for a $1 \times 10^{15}\text{cm}^{-2}$ 1 keV and implant for a 1050°C spike anneal in 33 ppm O_2 in N_2 ambient. Ramp-up rates are 50°C/s and 425°C/s, and initial ramp-down rate is 87°C/s. Data from Downey *et al.* [30].

5.3 Summary

In summary, we have investigated the phenomena which control junction depth for ultra-low energy boron implants. We find it is possible to model the extent of diffusion during both soak and spike RTA (rapid thermal anneals) with varying ramp rates by considering the full thermal cycle with models developed in previous sections. These models allow the optimization of RTP annealing cycles considering the trade-offs between junction depth and sheet resistance. For example, with 1050°C spike anneals, the active dose (and thus sheet conductivity) varies approximately linearly with junction depth. However, faster ramp rates allow the use of higher spike temperatures, with associated higher activation and reduced sheet resistance for the same junction depth.

Chapter 6

High Energy Implants and Vacancy Clustering

Understanding and modeling vacancy clusters is essential to modeling diffusion following well formation and exploring the novel use of vacancies in the formation of next generation devices. For example, use of higher energy sub-amorphizing Si implants has been found to reduce transient enhanced diffusion for medium dose boron implants [92]. Fig. 6.1 shows experiments by Sultan *et al.* [92] in which a Si pre-implant was used to obtain shallower boron junctions. In this chapter, we model the formation and subsequent annealing of the vacancy rich layer produced from high energy implants.

6.1 Vacancy cluster model

Bongiorno *et al.* performed tight binding molecular dynamics (TBMD) calculations to obtain formation and thus binding energies for vacancy clusters in silicon for $n \leq 35$ [11]. Their results show that different growth patterns for cluster formation exist. The binding energy $E_{\mathrm{b}}(n)$ for adding a vacancy to a $n-1$ size cluster is not a smooth function of size but rather it is non-monotonic. As shown in Fig. 6.2 for small cluster sizes ($n < 24$), Hexagonal Ring Clusters (HRC, clusters grown by removing Si atoms from the 6-membered rings present in the Si crystal structure) are more energetically favorable with respect to Spheroidal Clusters (SPC, clusters grown removing Si atoms from successive shells of neighbors of given atoms). Hence, we use values for SPC for larger clusters and HRC for smaller clusters. In the absence of TBMD calculations for clusters larger than 35, we use a functional form for the binding energy from Jaraiz *et al.* [59]. Discrete reactions are solved at each cluster size. Clusters can grow or dissolve with addition or release of a vacancy,

$$\mathrm{V}_{n-1} + \mathrm{V} \Leftrightarrow \mathrm{V}_n. \tag{6.1}$$

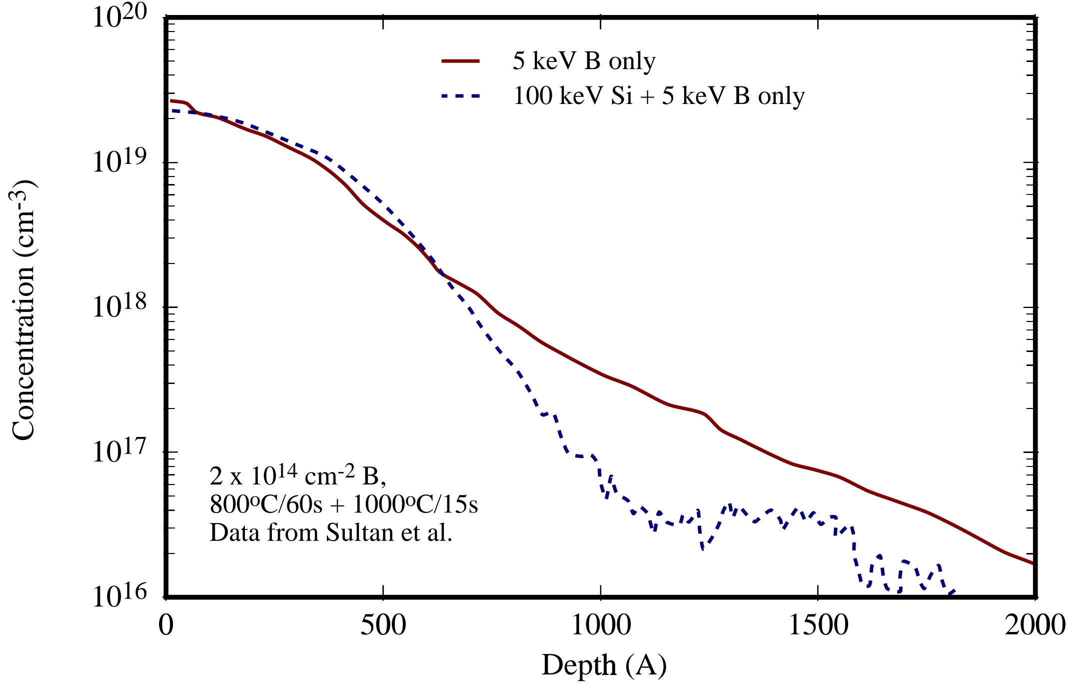

Figure 6.1: Boron profiles formed from a 2×10^{14} cm^{-2}, 5 keV B implant after a two-step anneal at 800°C/60sec and then 1000°C/15sec. A shallower junction is formed if a 100 keV Si pre-implant is used prior to the boron implantation.

Vacancy clusters can also dissolve by annihilation with interstitials,

$$\mathrm{V}_n + \mathrm{I} \Leftrightarrow \mathrm{V}_{n-1}. \tag{6.2}$$

The net rate of formation of size n cluster from size $n-1$ is given by the sum of the rates of Eqs. 6.1 and 6.2 as:

$$R_n = R_{\mathrm{V}_n}^{V/V_{n-1}} - R_{\mathrm{V}_n}^{I/V_n}. \tag{6.3}$$

All reaction kinetics are assumed diffusion limited, and hence the rate of formation $R_{\mathrm{V}_n}^{V/V_{n-1}}$ of V_n from Eq. 6.1 is given by,

$$R_{\mathrm{V}_n}^{V/V_{n-1}} = 4\pi\sigma_{n-1}^{\mathrm{V/V_{n-1}}} D_{\mathrm{V}} \left(C_{\mathrm{V}_{n-1}} C_{\mathrm{V}} - \frac{C_{\mathrm{V}_n}}{K_{\mathrm{V}_n}^{\mathrm{V/V_{n-1}}}} \right), \tag{6.4}$$

where D_{V} is the vacancy diffusivity and $\sigma_{n-1}^{\mathrm{V/V_{n-1}}}$ is the capture radius of the reaction and

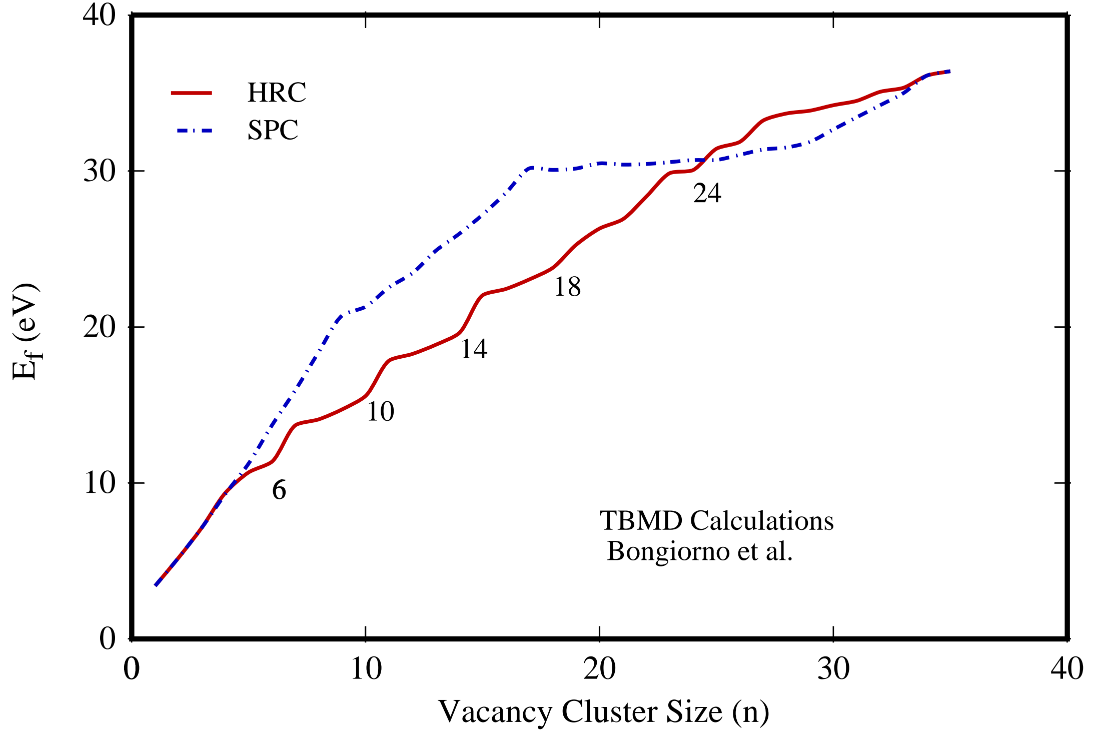

Figure 6.2: Cluster energetics calculations from Bongiorno *et al.* [11]. It can be noted that for small clusters ($n < 24$), Hexagonal Ring Clusters are more energetically favorable with respect to Spheroidal Clusters.

is defined as

$$\sigma_n^{\mathrm{V/V_{n-1}}} = \frac{A_{cap}^{\mathrm{V/V_{n-1}}}}{4\pi a_{hop}}. \tag{6.5}$$

a_{hop} is the hop distance and is taken to be equal to a_o, the lattice constant of silicon. A^n_{cap} is the capture cross-section and is given by,

$$A_{cap}^{\mathrm{V/V_{n-1}}} = \pi (r_{cap}^{\mathrm{V/V_{n-1}}})^2 = 4\pi (n-1)^{2/3} a_0^2. \tag{6.6}$$

$K_{\mathrm{V}_n}^{\mathrm{V/V_{n-1}}}$ is the equilibrium constant for Eq. 6.1 and is given as,

$$K_{\mathrm{V}_n}^{\mathrm{V/V_{n-1}}} = \left(\frac{1}{5 \times 10^{22}\ \mathrm{cm}^{-3}} \right) \exp\left[\frac{E_{\mathrm{b}}(n)}{kT} \right] \tag{6.7}$$

The reaction rate for Eq. 6.2 is given as,

$$R_{\mathrm{V}_n}^{I/V_n} = \sigma_n^{\mathrm{I/V_n}} D_{\mathrm{I}} \left(C_{\mathrm{V}_n} C_{\mathrm{I}} - \frac{C_{\mathrm{V}_{n-1}}}{K_{\mathrm{V}_n}^{\mathrm{I/V_n}}} \right). \tag{6.8}$$

The equilibrium constant for this reaction can be obtained as,

$$K_{\mathrm{V}_{n-1}}^{\mathrm{I/V_n}} = \frac{1}{K_{\mathrm{V}_n}^{\mathrm{V/V_{n-1}}} C_{\mathrm{I}}^* C_{\mathrm{V}}^*}. \tag{6.9}$$

We assume a small barrier $E_{\mathrm{I/V}}$ of 0.2 eV to I/V recombination [33] and hence

$$\sigma_n^{\mathrm{I/V_n}} = \frac{A_{cap}^{\mathrm{I/V_n}}}{a_{hop}} \exp\left[-\frac{E_{\mathrm{I/V}}}{kT}\right] \tag{6.10}$$

$$= 4\pi(n)^{2/3} a_0 \exp\left[-\frac{E_{\mathrm{I/V}}}{kT}\right]. \tag{6.11}$$

The vacancy cluster energies from Bongiorno *et al*. [11] are shown in Table 6.1. For larger sized vacancies the binding energy used from Jaraiz *et al*. [59] is

$$E_{\mathrm{b}}(n) = 3.65 - 5.15\left[n^{(2/3)} - (n-1)^{(2/3)}\right] \tag{6.12}$$

Net I and Net V concentrations from TRIM [10] are used as initial conditions. We use an analytical model for interstitial type extended defects from previous work by Gencer *et al*. [40, 41, 42, 43] As per this model, interstitials agglomerate into {311} defects and further transform into loops. The {311} and loop models are calibrated to transmission electron microscopy (TEM) data [35, 81].

6.2 Comparison to Au-labeling experiments

One of the primary problems associated with modeling vacancy clusters is the difficulty of directly observing the defects. Most of the available experiments provide indirect evidence of the presence of vacancy clusters. In this paper, we use Au in-diffusion data [96] from MeV Si implants. In the experiments [96] considered, Si was implanted to a dose of $10^{16}\mathrm{cm}^{-2}$ at different MeV energies. The implants were performed at 300°C to promote recombination of point defects and thus avoid amorphization. The samples were then annealed at different temperatures and times. Finally, they were implanted with Au and annealed at a lower temperature (750°C). Au from the implant was found to getter around $\mathrm{R}_p/2$ and was measured by RBS. The final Au concentration was reported to be relatively insensitive to the time of Au drive-in diffusion and is much higher than its equilibrium

Table 6.1: Parameters from Bongiorno *et al.* [11] used for the simulations. $E_\mathrm{f}(n)$ is the formation energy and $E_\mathrm{b}(n)$ is the binding energy in eV. We use SPC formation energies for $n > 24$ and HRC for the clusters smaller than 25.

Size	1	2	3	4	5	6	7	8	9	10
$E_\mathrm{f}(n)$	3.40	5.20	7.14	9.36	10.68	11.37	13.7	14.08	14.72	15.58
$E_\mathrm{b}(n)$	-	1.60	1.46	1.18	2.08	2.71	1.07	3.02	2.76	2.54

Size	11	12	13	14	15	16	17	18	19
$E_\mathrm{f}(n)$	17.84	18.27	18.86	19.61	22.03	22.44	23.05	23.79	25.27
$E_\mathrm{b}(n)$	1.14	2.97	2.81	2.65	0.98	2.99	2.79	2.66	1.92

Size	20	21	22	23	24	25	26	27	28
$E_\mathrm{f}(n)$	26.31	26.91	28.36	29.86	30.06	30.71	31.04	31.38	31.51
$E_\mathrm{b}(n)$	2.36	2.80	1.95	1.90	3.20	2.75	3.07	3.06	3.27

Size	29	30	31	32	33	34	35
$E_\mathrm{f}(n)$	31.87	32.67	33.45	34.22	35.00	36.12	36.4
$E_\mathrm{b}(n)$	3.04	2.6	2.62	2.63	2.62	2.28	3.12

solubility in silicon. TEM images reveal Au related precipitates approximately 150 Å in diameter distributed over a depth similar to that indicated by the RBS profiles. Au diffuses rapidly in Si via an interstitial mechanism. Hence, an increase in vacancy concentration moves Au_i more strongly onto substitutional sites, either via $\mathrm{Au}_i + \mathrm{V} \rightarrow \mathrm{Au}_s$ or by decoration of vacancies cluster/voids. The total Au concentration is dependent on the interaction of the Au_i with vacancies and vacancy clusters. Since the exact nature of the kinetics of Au precipitation is not clear, we cannot quantitatively determine the vacancy cluster concentrations using these experiments. Recent results indicate that the ratio of gold to vacancies is infact close to 1 [61].

Simulations show that vacancy clusters are fairly stable in the vacancy rich layer and can lead to enhancement of vacancy diffusers like Sb. For example, we obtain a time averaged vacancy supersaturation ($< C_\mathrm{V}/C_\mathrm{V}^* >$) of ~ 20 after a 950°C/600 s anneal of a 2 MeV 10^{16} cm^{-2} Si implant. Fig. 6.3 shows a typical size distribution after a short time anneal at 750°C. As shown here, the most stable clusters are of cluster sizes $n = 6$, 10, 14, 18 and 24. Also shown in the same plot is the distribution at 950°C. It is clear that larger clusters play a more important role at higher temperatures for which there is a rapid growth to larger sizes. Fig. 6.4 shows a 2 MeV 10^{16} cm^{-2} Si implant annealed at 750°C for varying times and compared to experimental data [96]. We obtain a very good prediction of the depth distribution of the clustered vacancies. At 750°C, the clusters are very stable and almost no change in total clustered vacancy concentration is seen between 10 min and

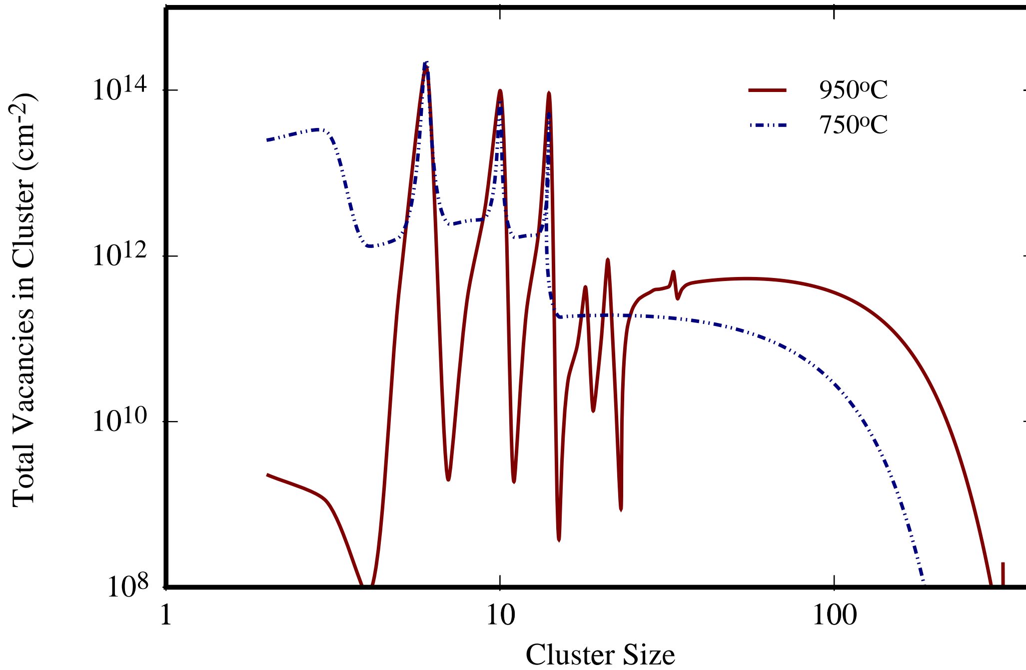

Figure 6.3: Simulated size distribution of clusters after a short time anneal at 750°C and 950°C. Clusters are ripening into larger clusters more predominantly at the higher temperature. This also shows the most stable small cluster sizes to be around 6, 10, 14, 18 and 24 due to the non-monotonic binding energy.

1 h anneals, consistent with experimental observations [96]. Fig. 6.5 shows comparisons to data at 950°C. Note that the simulations agree well with the time dependence of the data. At higher temperatures, vacancy clusters are annihilated by an increased dissolution of interstitial defects from the bulk and surface annihilation of vacancies. Shown in Fig. 6.6 is the comparison to 1000°C data. The clusters around $R_p/2$ are the largest and therefore the most stable. Hence, there is a peak in cluster concentration at $R_p/2$ in the simulations similar to that observed in the experimental data [96]. We can further analyze our results to see the fraction of vacancies in smaller sized clusters ($n < 36$). Note that these were the clusters for which we used TBMD results from Bongiorno *et al*. [11]. Figs. 6.7 and 6.8 shows the significance of the addition of larger sized clusters. At 750°C, a significant fraction of smaller sized clusters are present. However, at 950°C most of the clusters, especially around $R_p/2$ have ripened into larger clusters ($n > 35$).

An important factor in matching the vacancy clustering is related to the interstitial clustering model used. Since these simulations involve a high implant dose of 10^{16} cm^{-2}, we can expect to see considerable transformation to loops. Indeed, in all the simulations most of the {311} defects transform into loops. If we use only a {311} model and do not

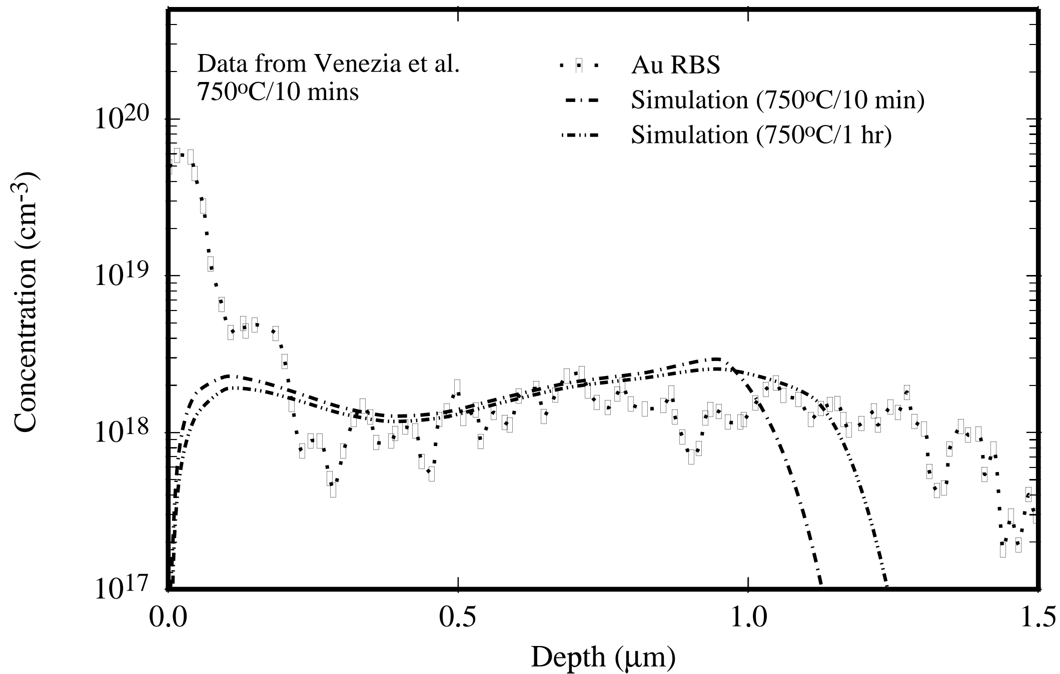

Figure 6.4: Simulated clustered vacancy concentrations compared to Au RBS data for 750°C anneals of 10 min and 1 h. Simulation show that there is very litle change in the clustered vacancy concentration between 10 min and 1 h. This is in agreement with results from Venezia *et al*. [96] who also report that Au concentrations are nearly constant for longer anneals up to 8 h at 750°C. Note that the surface peak in the data is because of the Au implant used for the in-diffusion.

consider loop formation, the vacancy clusters are quickly annihilated by the interstitials from the bulk at the higher temperatures. As seen in Fig. 6.9, using only a {311} model without any loop formation leads to dissolution of all the clusters in a time span of less than 60 s, contrary to the experimental observations.

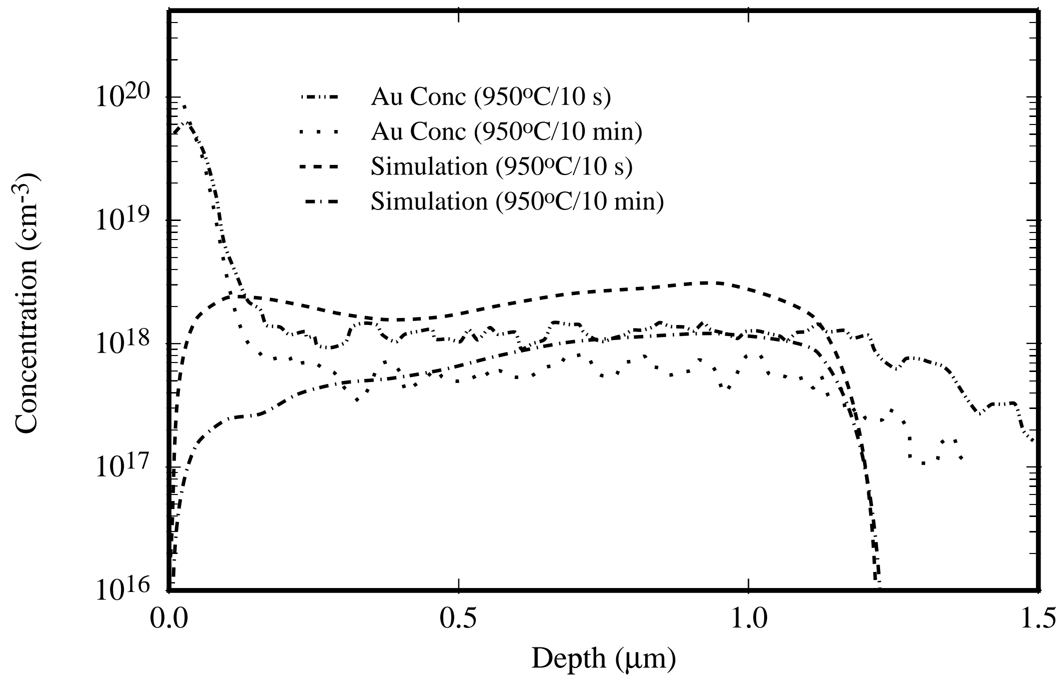

Figure 6.5: Simulated and clustered vacancy concentrations compared to Au RBS data after 950°C anneal of 10 s and 10 min. At 950°C, vacancy clusters are annihilated by an increased dissolution of interstitial defects from the bulk and loss to the surface. Note that the simulations agree well with the time dependence of the data.

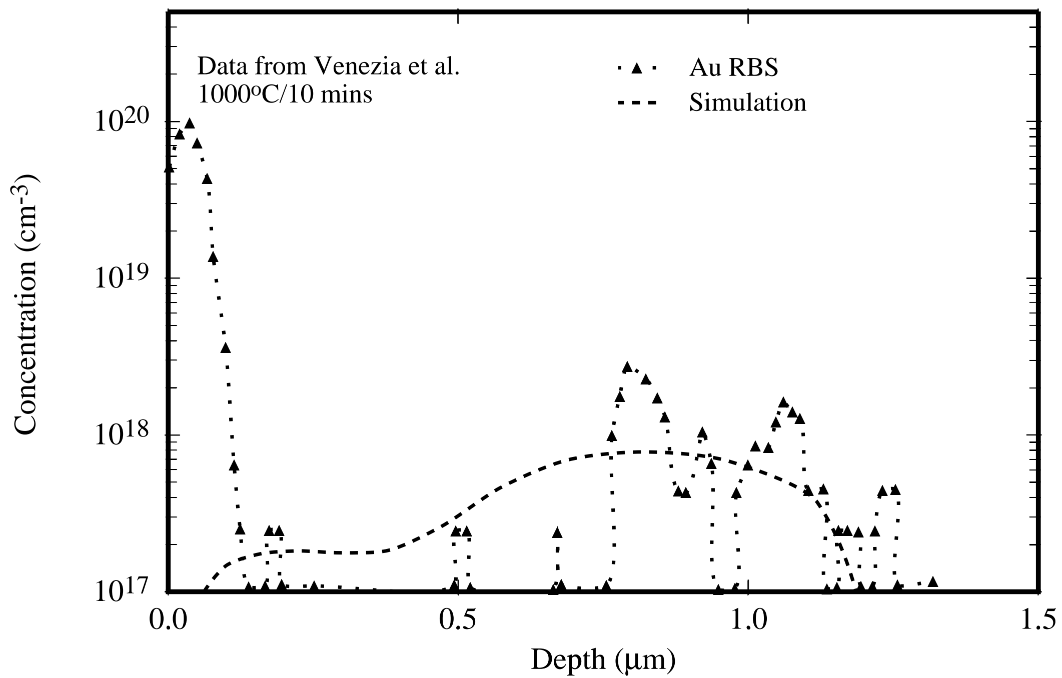

Figure 6.6: Simulation and clustered vacancy concentrations compared to Au RBS data after a 1000°C anneal of 10 min. At 1000°C, the vacancy clusters are increasingly annihilated from the surface and the dissolution of interstitial defects from the bulk. The clusters around $R_p/2$ are the largest and therefore the most stable. Hence there is a peak in cluster concentration at $R_p/2$ (0.9 μm) in the simulations similar to that observed in the experimental data [96].

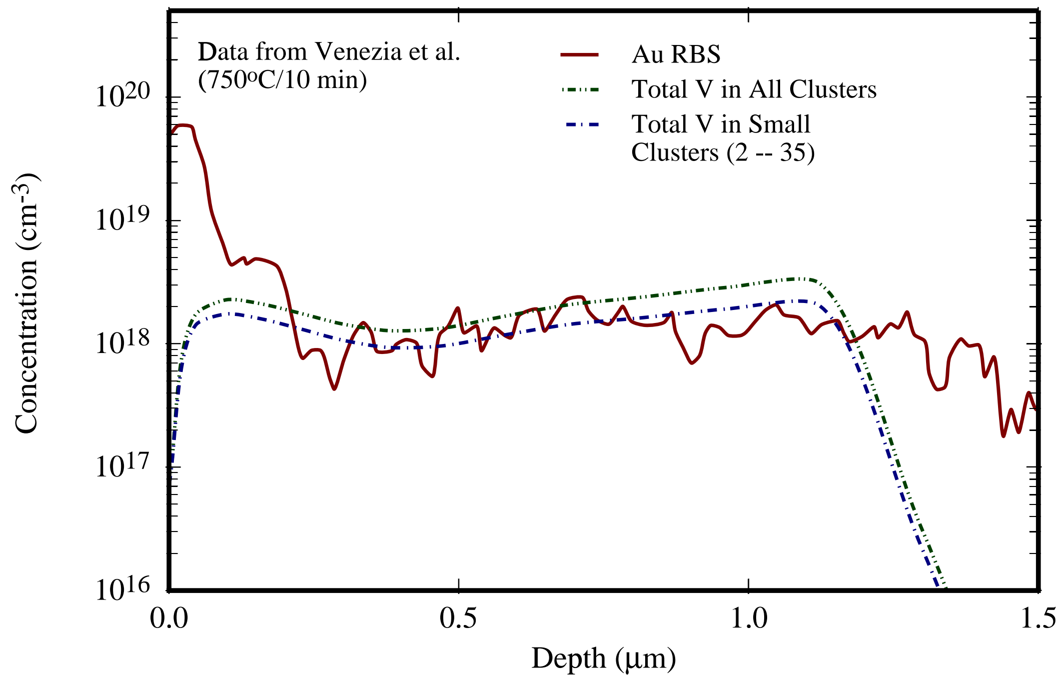

Figure 6.7: At 750°C, a considerable fraction of the vacancies are in smaller sized clusters.

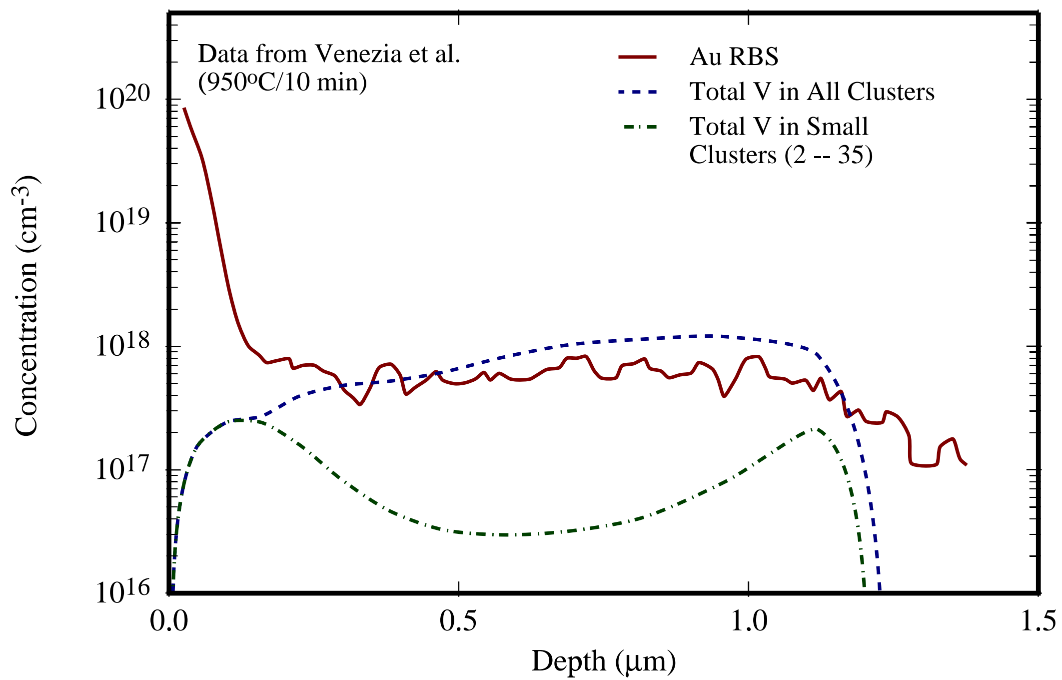

Figure 6.8: The above figure shows the significance of the addition of larger sized clusters. At 950°C most of the clusters especially around $R_p/2$ have ripened into larger clusters ($n > 35$).

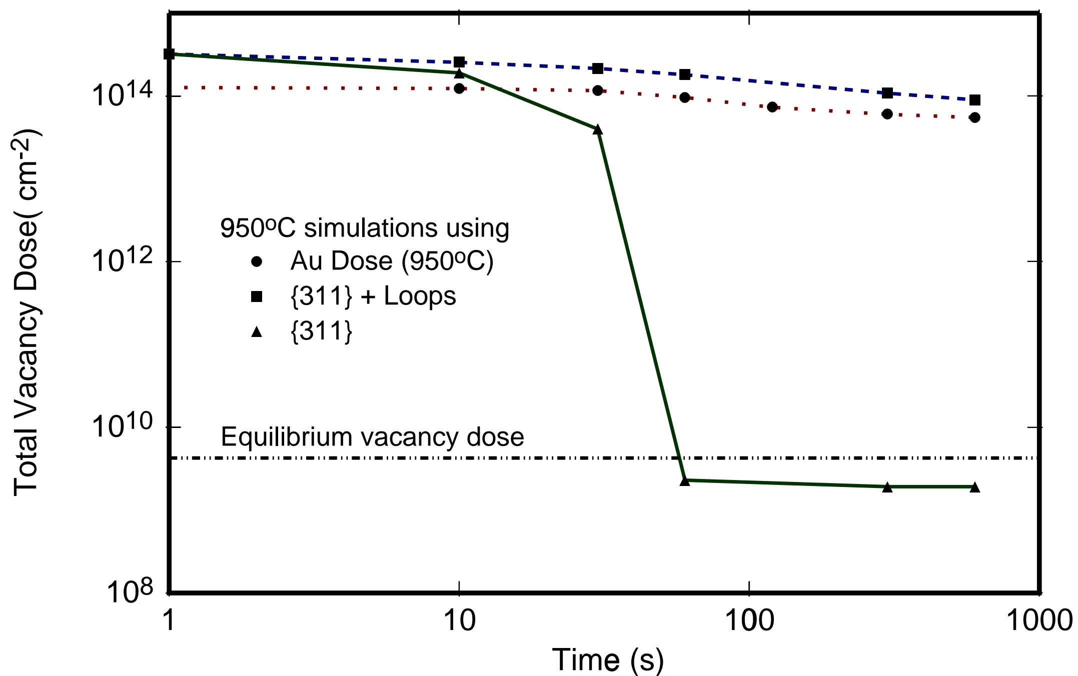

Figure 6.9: Time dependence of vacancies in system (depth of 1000 μm). Using only a $\{311\}$ model without any loop formation leads to dissolution of all the clusters by about 60 s, contrary to experiments. It should be noted that the experimental value reported by Venezia *et al*. [96] is measured between 0.2 – 1 μm to avoid including the Au implant profile. This method also leaves out the dose of vacancies below 0.2 μm. Hence the experimental results are expected to be lower than the simulation results despite having a good agreement in the depth distributions. Also, without loops the vacancy concentration drops below the equilibrium value due to the interstitial supersaturation from the dissolving $\{311\}$ defects.

6.3 Moment based models

The physical rate equation model described in the previous sections is computationally very expensive since the full size distribution is tracked at each point in space. Even if one limits the number of precipitate sizes that will be solved for, the number of variables is still very large for efficient solution of the equation system. If the system has multiple spatial dimensions, the number of solution variables becomes prohibitively large. Clejan *et al.* developed a more efficient approach based on considering the size distribution in terms of a small number of moments [23]. Only the evolution of those moments are considered rather than the full distribution at each point in space. We restate the equations as described in Section 4.1 again for convenience. The moments are defined as [23]:

$$m_i = \sum_{n=2}^{\infty} n^i f_n, \tag{6.13}$$

where $i = 0, 1, 2, \ldots$. The zeroth order moment of the distribution is simply the precipitate density, while the first moment corresponds to the density of precipitated solute atoms. Higher order moments further describe the shape of the size distribution. This transforms the system of equations to the following set [23]:

$$\frac{\partial m_i}{\partial t} = 2^i R_2 + \sum_{n=2}^{\infty} \left[(n+1)^i - n^i\right] R_n \tag{6.14}$$

Note that the sums over the R_n can all be written in terms of sums over f_n, nf_n, etc. Hence, they can be calculated from the moments if moments are used to describe the distribution. This reduces the system of equations to be solved to:

$$\begin{aligned}
\frac{\partial m_i}{\partial t} &= D_\text{V}\left[2^i \lambda_1 C_\text{V}^2 + m_0 C_\text{V} \gamma_i^+ - m_0 C_\text{ss} \gamma_i^-\right] \\
\gamma_i^+ &= \sum_{n=2}^{\infty} \left[(n+1)^i - n^i\right] \lambda_n \hat{f}_n \\
\gamma_i^- &= \lambda_1 \hat{C}_1^* \hat{f}_2 + \sum_{n=2}^{\infty} \left[n^i - (n-1)^i\right] \lambda_{n-1} \hat{C}_{n-1}^* \hat{f}_n
\end{aligned} \tag{6.15}$$

where $\hat{C}_n^* = C_n^*/C_\text{ss}$ and $\hat{f}_n = f_n/m_0$.

If we allow interstitials react with the vacancy clusters, we would need to add extra terms to the moment equations. We can further neglect the generation of interstitials from vacancy clusters (backward reaction of Eq. 6.2). Thus, with the same definitions of γ_i as before and setting $\bar{\gamma}_0 = \lambda_2 \hat{f}_2$ the moments can be derived to be:

$$\frac{\partial m_0}{\partial t} = D_\text{V}\left[\lambda_1 C_\text{V}{}^2 - m_0 C_\text{ss} \gamma_0\right] - D_\text{I} C_\text{I} m_0 \bar{\gamma}_0 \tag{6.16}$$

$$
\begin{aligned}
\frac{\partial m_1}{\partial t} &= D_{\rm V}\left[2\lambda_1 C_{\rm V}{}^2 + m_0 C_{\rm V}\gamma_1^+ - m_0 C_{\rm ss}\gamma_1^-\right] - D_{\rm I} C_{\rm I} m_0\left[\bar{\gamma}_0 + \gamma_1^+\right] \\
\frac{\partial m_2}{\partial t} &= D_{\rm V}\left[4\lambda_1 C_{\rm V}{}^2 + m_0 C_{\rm V}\gamma_2^+ - m_0 C_{\rm ss}\gamma_2^-\right] - D_{\rm I} C_{\rm I} m_0\left[\bar{\gamma}_0 + \gamma_2^+ - 2\gamma_1^+\right] \\
\frac{\partial C_{\rm V}}{\partial t} &= -D_{\rm V}\left[2\lambda_1 C_{\rm V}{}^2 + m_0 C_{\rm V}\gamma_1^+ - m_0 C_{\rm ss}\gamma_1^-\right] + D_{\rm I} C_{\rm I} m_0 \bar{\gamma}_0 \\
\frac{\partial C_{\rm I}}{\partial t} &= -D_{\rm I} C_{\rm I} m_0\left[\bar{\gamma}_0 + \gamma_1^+\right]
\end{aligned}
$$

Since any finite number of moments is insufficient to describe an arbitrary distribution, it is necessary to add a closure assumption, which is an assumption about the form of the distribution, $f_n = f(n, z_i)$. The z_i are parameters of the distribution which can be determined from the moments. The number of moments we need to keep track of equals the number of parameters in the distribution function.

Since we want to develop the most computationally efficient model, we consider the possibility of representing the system in terms of its first two moments following the work of Gencer and Dunham [43]. The value can be found approximately from a weighted sum of λ_n. Therefore, our system reduces to:

$$
\begin{aligned}
\frac{\partial m_0}{\partial t} &= R_2 = D\lambda\left(C_{\rm V}^2 - m_0 C_{\rm ss}\gamma_0\right) - D_{\rm I}\lambda C_{\rm I} m_0 \bar{\gamma}_0 \\
\frac{\partial m_1}{\partial t} &= 2R_2 + D\lambda m_0\left(C_{\rm V} - C_{\rm ss}\gamma_1\right) - D_{\rm I}\lambda C_{\rm I} m_0\left(1 - \bar{\gamma}_0\right) \\
\frac{\partial C_{\rm V}}{\partial t} &= -\left[2R_2 + D\lambda m_0\left(C_{\rm V} - C_{\rm ss}\gamma_1\right) + D_{\rm I}\lambda C_{\rm I} m_0 \bar{\gamma}_0\right] \\
\frac{\partial C_{\rm I}}{\partial t} &= -D_{\rm I}\lambda C_{\rm I} m_0\left(1 + \bar{\gamma}_0\right)
\end{aligned}
\tag{6.17}
$$

with

$$
\begin{aligned}
\gamma_0 &= \hat{C}_1^* \hat{f}_2 \\
\bar{\gamma}_0 &= \hat{f}_2 = \gamma_0 / \hat{C}_1^* \\
\gamma_1 &= \sum_{n=2}^{\infty} \hat{C}_n^* \hat{f}_{n+1}
\end{aligned}
\tag{6.18}
$$

Using the full set of rate equations, it is now possible to calculate γ_i numerically. The full rate equation model was simulated at a single grid point. A large maximum size of 1000 was chosen to remove any errors due to pile-up at the largest size. The simulation was run for different times to extract γ_i and $\hat{m}_1$. Figs. 6.10 and 6.11 show γ_i plotted against $\hat{m}_1$ extracted from the full model. It can be noted that γ_i satisfy the following limits as

expected [43]:

$$\begin{aligned}
\lim_{\hat{m}_1 \to 2} \gamma_0 &= \hat{C}_1^* \\
\lim_{\hat{m}_1 \to \infty} \gamma_0 &= 0 \\
\lim_{\hat{m}_1 \to 2} \gamma_1 &= 0 \\
\lim_{\hat{m}_1 \to \infty} \gamma_1 &= 1
\end{aligned} \qquad (6.19)$$

For larger $\hat{m}_1$, γ_i are found to have only a weak dependence on temperature. Further, γ_i seem to be unique functions of $\hat{m}_1$ within reasonable errors. However to confirm this hypothesis it is necessary to be able to obtain the same γ_i irrespective of its thermal history. Figs. 6.10 and 6.11 also show comparisons between two-step anneal. It was found samples simulated at 1000°C with and without a 400°C preanneal gave very similar γ_i, giving credence to the possibility of using only the first two moments to model this system. It is now possible to find analytic expressions to fit the obtained γ_i. For example, we can now use the obtained γ_i in the set of equations given by Eqns. 6.18. There are no other free parameters in this system. Note that C_{ss} can be taken as C_{V}^* and is not a fitting parameter. Using the γ_i thus derived, we however found the simulation to be numerically unstable due to the strong change in γ_i at small average sizes. Hence a new set of γ_i were constructed neglecting small size effects. A kinetic barrier can be added to correct for the growth rate at small sizes. Figs. 6.12 and 6.13 show such γ_i values. A barrier of 0.4 eV was added to all reactions as a correction to include small size effects. This system was now found to give good match to experimental data and the full rate equation model. As shown in Fig. 6.15 the AKPM model matches the full rate equation model fairly well over both dissolution and depth at 1000°C. Further Fig. 6.14 shows anneals at 950°C showing good time and temperature dependence.

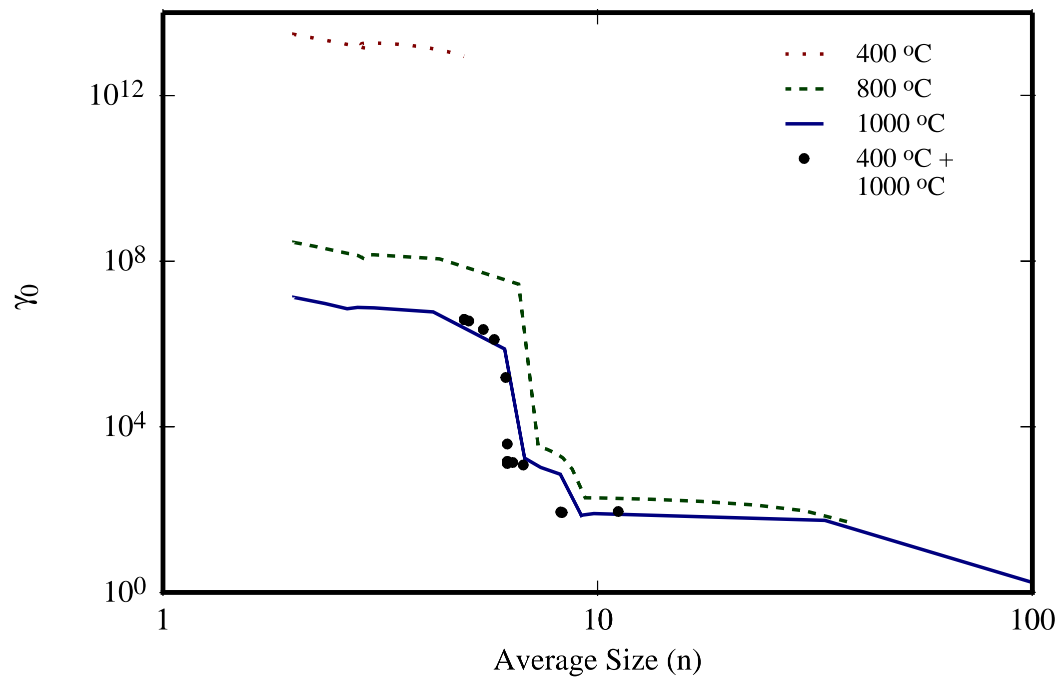

Figure 6.10: γ_0 values extracted from simulations of the full system of rate equations for three different temperatures (400, 800, 1000°C) . Also shown in the same plot is γ_0 value for a 1000°C anneal after a preanneal at 400°C. Note that the γ_0 is almost independent of its thermal history.

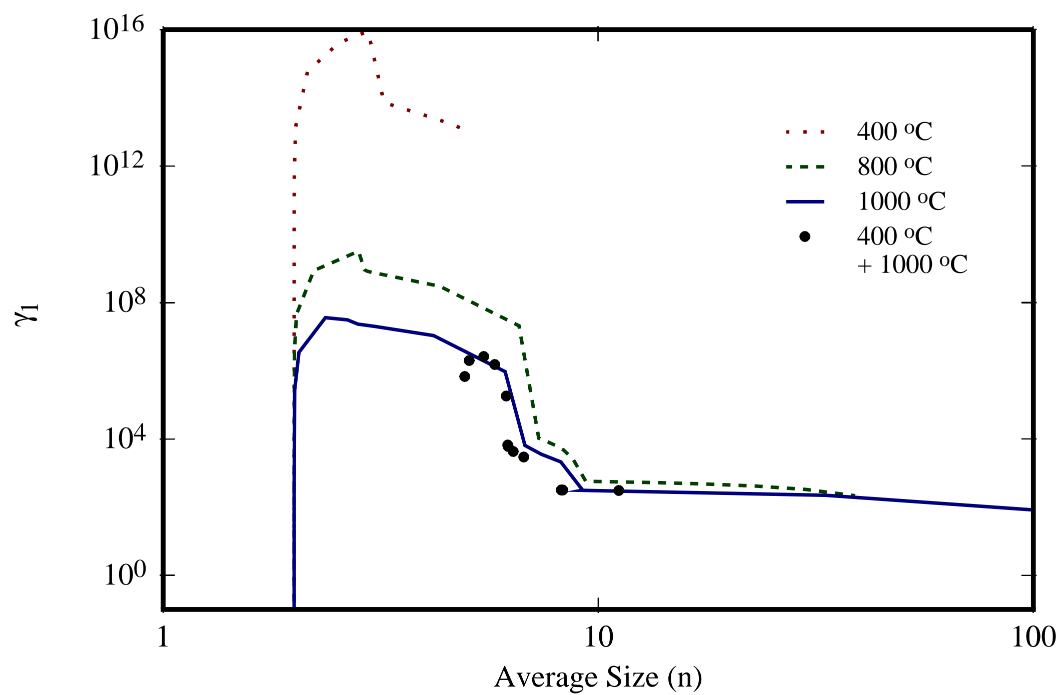

Figure 6.11: γ_1 values extracted from simulations of the full system of rate equations for three different temperatures (400, 800, 1000°C) . Also shown in the same plot is γ_1 value for a 1000°C anneal after a preanneal at 400°C. Note that the γ_1 is almost independent of its thermal history.

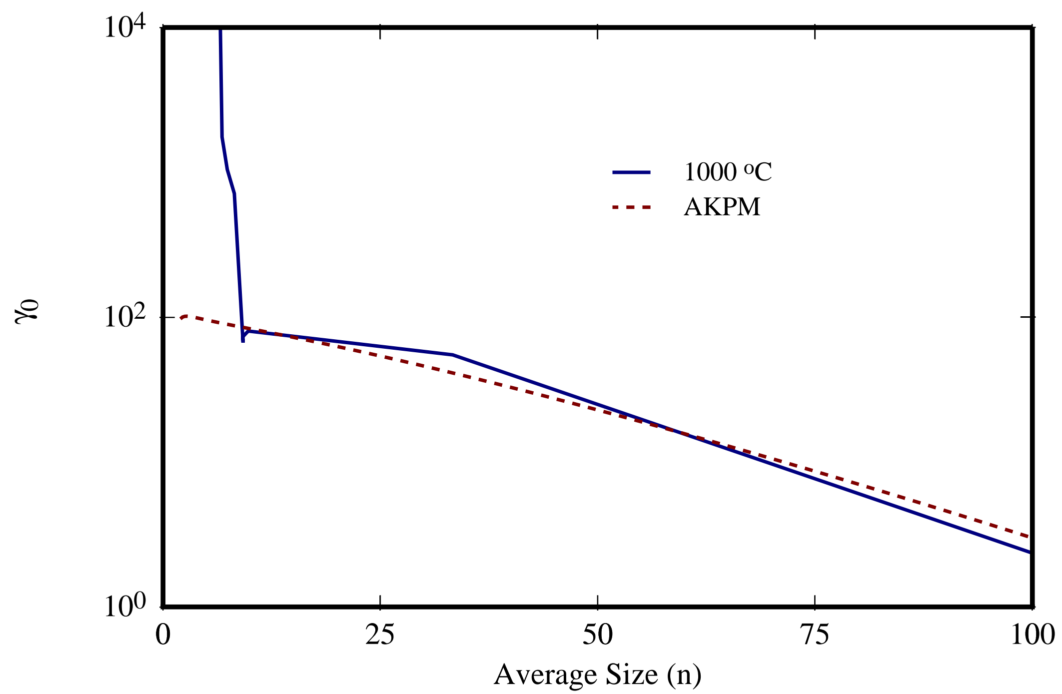

Figure 6.12: Analytic fit to γ_0 neglecting small size effects. This was done to avoid the exponential change in γ_i values.

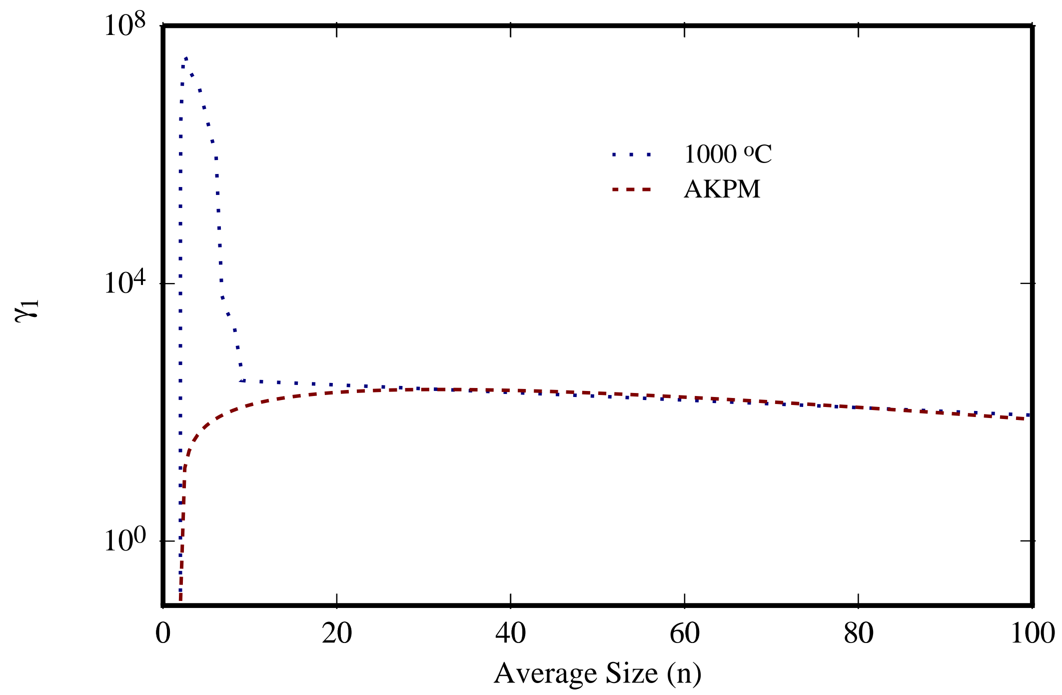

Figure 6.13: Analytic fit to γ_1 neglecting the near exponential change near small sizes.

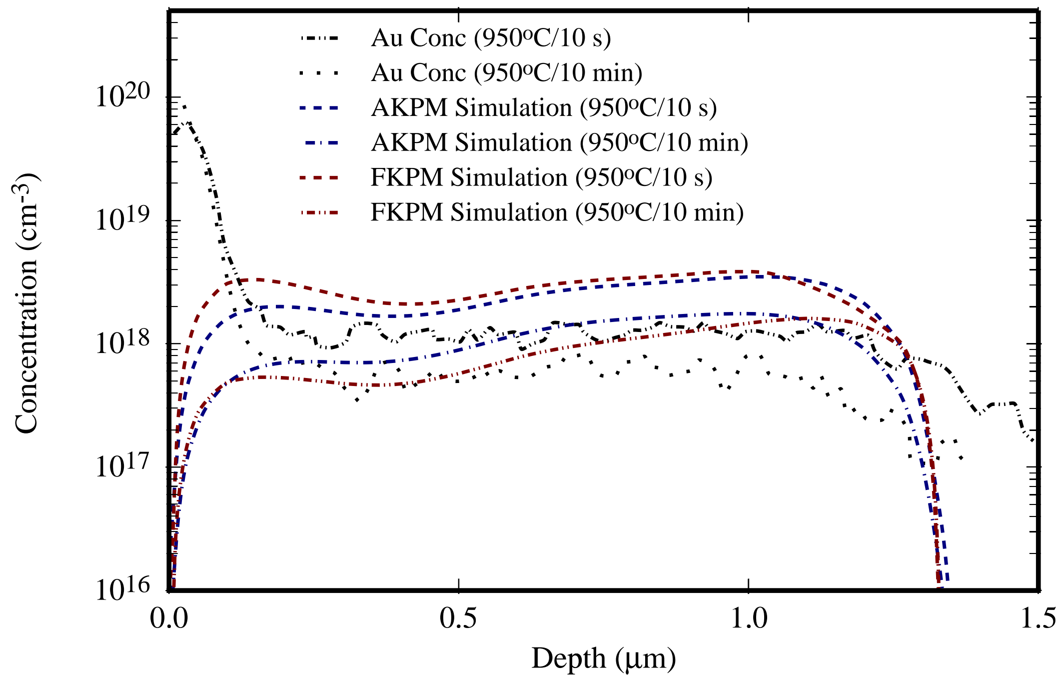

Figure 6.14: Comparison of AKPM and full discrete cluster model at 950°C

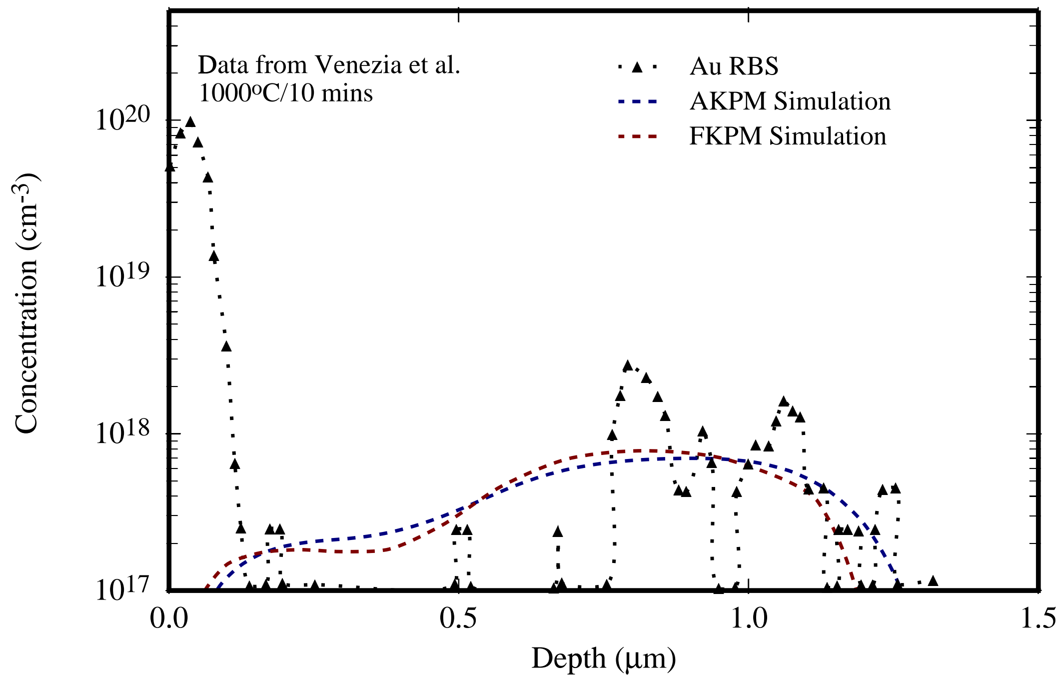

Figure 6.15: Comparison of AKPM and full discrete cluster model at 1000°C

6.4 Summary

A set of discrete clusters are used to model vacancy cluster evolution after high energy ion-implantation in Si. The parameters for this system are from atomistic calculations. It was found that this system is able to predict the temperature, time and depth dependence of vacancy clusters seen in the experimental results. A procedure has been proposed to reduce this complex model into a simple two-moment model. The parameters for this two moment model are derived from the full rate equation model and are found to give good prediction to data. This efficient two-moment model can be easily incorporated into technology modeling tools and applied to model more complex situations.

Chapter 7

Conclusions and Future Work

7.1 Summary

Our aim in this work was to understand and model the evolution of ion implanted silicon during annealing, particularly with respect to the characteristics shown by boron. In our work, we have contributed over a range of topics necessary to help in the understanding of the evolution of an ion implanted Si wafer.

We evaluated metal diffusion experiments to better understand point defect properties. Using a consistent modeling approach, we found the vacancy diffusivity to be of the same order of magnitude as the interstitial diffusivity. The resulting vacancy diffusivity is much faster than derived from previous analysis but is much closer to atomistic calculations. However, we found it was not possible to identify vacancy transport properties accurately from metal diffusion experiments alone.

To understand the initial conditions for our simulations, we simulated the initial damage annealing process to determine the point defect concentrations present after recombination within the damage cascade. It was found that for low dose or high energy implants, the number of interstitials remaining after this recombination can strongly deviate from a "+1" of the implant dose due to diffusion of vacancies to the surface. We also simulated the full damage to understand the effect of formation of interstitial and vacancy clusters. It was found that though vacancy clusters can survive to relatively long times at low temperatures, the change in observed supersaturation (relative to using a "+1" model) is neglible, and hence a "+1" model can be used effectively under these circumstances.

We evaluated different approaches to modeling boron/interstitial clustering. In particular, we looked at modeling boron clusters using a moment-based kinetic precipitation model and cluster based models. We found that both models can predict existing data well if necessary parameters can be optimized. Since *ab-initio* calculations have emerged as a powerful tool to help determine cluster precursors, cluster based models have the advan-

tage of being more physically-based for modeling initial stages of clustering. A simple cluster model was derived from an extensive model based on atomistic calculations performed at Lawrence Livermore National Labs [60]. This simple model was successfully used in modeling boron interstitial clusters, was further extended to include charge states of clusters and understand marker experiments. This model was also able to match electrical activation data.

The boron model was used successfully in understanding and modeling ultra low energy boron implants for both soak and spike anneals. It was found that it is possible to model new behavior like saturation of obtainable minimum junction depth in agreement with experimental results. We also looked at modeling the excess vacancy layer formed after high energy implantation. For this, a vacancy cluster model was developed based on cluster energetics values from Tight Binding Molecular Dynamics (TBMD) calculations [11]. This model was further simplified using a moment-based approach to enable efficient incorporation into industrial process simulators.

7.2 Future Directions

In recent years, progress in atomistic calculations have made it possible to obtain formation energies of dopant/defect clusters. However, these techniques become computationally prohibitive for larger sized clusters that can evolve during the annealing process. Hence, although they help us understand the cluster precursors, no calculations exist for larger cluster sizes. The behavior of larger clusters can often be estimated from experimental observations, and the properties exhibited by such larger clusters can be modeled efficiently by using moment-based approaches. Effective modeling of such systems should include discrete clusters at small sizes and moments to represent larger sized clusters. This situation is complicated for two component systems like boron-interstitial clusters. Here the clusters can grow into larger interstitial or boron rich phases, and the moment based model itself needs to be derived carefully. This can be simplified by working with a full discrete model as a basis for deriving the coupling between the moments. It can be expected that these may depend on the form chosen for the formation energy of these clusters.

Ultra low energy implants have been found to form an amorphous layer which forms a new boride phase. The implications of the formation of this new phase are not yet fully clear with regard to contributing to point defect supersaturations or electrical activation. New experiments are needed to highlight the effect of the formation of this new phase. Experimental research groups are focussed on increasing the activation beyond the solid solubility of boron by different methods like laser anneals, pre-amorphization implants. The underlying physical activation mechanisms during these processes is an important area for future study.

According to the International Technology Roadmap for Semiconductors [1], devices produced around 2010 with gate lengths of 50 nm will need highly active sub-20 nm junc-

tion depths (around 100–200 monolayers). As the channel length decreases, lateral diffusion becomes more important. However, according to current understanding of dopant diffusion, such junctions are unattainable for boron. Overcoming these barriers requires a better understanding of all processes at an atomistic level. This not only includes interaction of boron with point defects but also includes interaction with interfaces (oxide, silicides) and other bulk traps and impurities.

Bibliography

[1] "The international technology roadmap for semiconductors". International Semiconductor Manufacturing Technology (SEMATECH), Semiconductor Industry Association (SIA) (1999).

[2] A. Agarwal, D. J. Eaglesham, H.-J. Gossmann, L. Pelaz, S. B. Herner, D. C. Jacobson, T. E. Haynes, and Y. Erokhin. "Boron-enhanced-diffusion of boron from ultalow-energy boron implantation". In **Semiconductor Silicon 1998**, Electrochem. Soc. Proc., 1232 (1998).

[3] A. Agarwal, D. J. Eaglesham, H.-J. Gossmann, L. Pelaz, S. B. Herner, D. C. Jacobson, T. E. Haynes, Y. Erokhin, and R. Simonton. "Boron-enhanced-diffusion of boron: the limiting factor for ultra-shallow junctions". In **Internatinal Electron Device Meeting (IEDM) Technical Digest**, IEEE, 467 (1997).

[4] A. Agarwal, A. T. Fiory, and H.-J. L. Gossmann. "Optimizing RTA ramp rate for ultrashallow junctions". *Semiconductor International* **22**(5), 71 (1999).

[5] A. Agarwal and H.-J Gossmann. "Temperature- and time-dependence of boron-enhanced-diffusion from evaporated and ultra-low energy ion-implanted boron layers". In **Si Front-End Processing – Phys. and Tech. of Dopant-Defect Interactions**, Materials Research Society, 19 (1999).

[6] A. Agarwal, H.-J. Gossmann, and D. J. Eaglesham. "Boron-enhanced diffusion of boron: Physical mechanisms". *Applied Physics Letters* **74**(16), 2331 (1999).

[7] A. Agarwal, H.-J. Gossmann, D. J. Eaglesham, L. Pelaz, S. B. Herner, D. C. Jacobson, T. E. Haynes, and R. Simonton. "Damage, defects and diffusion from ultra-low energy (0–5 kev) ion implantation of silicon". *Solid State Electronics* **42**, A17 (1998).

[8] R. Angelucci, F. Cembali, P. Negrini, M. Servidori, and S. Solmi. "Temperature and time dependence of dopant enhanced diffusion in self ion implanted silicon". *Journal of Electrochemical Society* **134**(12), 3130 (1987).

[9] R. Angelucci, P. Negrini, and S. Solmi. “Transient enhanced diffusion of dopants in silicon induced by implantation damage”. *Appl. Phys. Lett.* **49**(21), 1468 (1986).

[10] J.P. Biersack. “Three-dimensional distributions of ion range and damage including recoil transport”. *Nuclear Instruments and Methods B* **19**, 32 (1986).

[11] A. Bongiorno, L. Colombo, and T. Diaz de la Rubia. “Structural and binding properties of vacancy clusters in silicon”. *Europhysics Letters* **43**(6), 695 (1998).

[12] H. Bracht, N. A. Stolwijk, and H. Mehrer. “Properties of intrinsic point defects in silicon determined by zinc diffusion experiments under nonequilibrium conditions”. *Physics Review B* **52**(23), 16542 (1995).

[13] H. Bracht, N. A. Stolwijk, I. Yonenaga, and H. Mehrer. “Thermodynamic properties of self-interstitials in silicon: An experimental investigation”. *Physics Status Solidi A* **137**, 499 (1993).

[14] R. A. Brown, O. Kononchuk, G. A. Rozgonyi, S. Koveshnikov, A. P. Knights, P. J. Simpson, and F. Gonz*á*lez. “Impurity gettering to secondary defects created by MeV ion implantation in silicon”. *Europhysics Letters* **43**(6), 695 (1998).

[15] M. Bunea. “Kinetic lattice monte carlo and *ab-initio* study of point defect mediated diffusion of dopants in silicon”. Ph.D. thesis, Boston University (2000).

[16] S. Chakravarthi and S.T. Dunham. “Point defect properties from metal diffusion experiments— what does the data really tell us?”. In **Defects and Diffusion in Silicon Processing**, Materials Research Society, 47 (1997).

[17] S. Chakravarthi and S. T. Dunham. “Influence of extended defect models on prediction of boron transient enhanced diffusion”. In **Silicon Front End Technology — Materials Processing and Modeling**, Materials Research Society, (1998).

[18] S. Chakravarthi and S. T. Dunham. “A simple continuum model for simulation of boron interstitial clusters based on atomistic calculations”. In **1998 International Conference on Simulation of Semiconductor Process and Devices, SISPAD’98 Technical Digest**, IEEE, (1998).

[19] S. Chakravarthi and S. T. Dunham. “Modeling of vacancy cluster formation in ion implanted silicon”. In **Process Physics and Modeling in Semiconductor Technology**, Electrochemical Society, (1999).

[20] S. Chakravarthi and S. T. Dunham. “Modeling of boron deactivation/activation kinetics during ion implant annealing”. In **International Conference on Simulation of Semiconductor Process and Devices, SISPAD’2000 Technical Digest**, IEEE, (2000).

[21] S. Chakravarthi, A. H. Gencer, S. T. Dunham, and D. F. Downey. “Understanding and modeling ramp rate effects on shallow junction formation”. In **Si Front-End Processing Physics and Technology of Dopant-Defect Interactions II**, Materials Research Society, (2000).

[22] J. Chen, S. Bharatan, and K.S. Jones. “The effect of dose rate and implanted temperature on transient enhanced diffusion in crystalline silicon”. In **Defects and Diffusion in Silicon Processing**, Materials Research Society, (1997).

[23] I. Clejan and S.T. Dunham. “A reduced moment based model for precipitaion kinetics and application to dopant deactivation in silicon”. *Journal of Applied Physics* **78**(12), 7327 (1995).

[24] I. Clejan and S.T. Dunham. “Interactions of point defects with boron and arsenic precipitates”. In **Process Physics and Modeling in Semiconductor Technology**, Electrochemical Society, 398 (1996).

[25] N.E.B. Cowern, G.F.A.van de Walle, D.J. Gravesteija, and C.J. Vriezema. “Experiments on atomic-scale mechanisms of diffusion”. *Physics Review B* **67**, 212 (1991).

[26] N.E.B. Cowern, K.T.F. Janssen, and H.F.F. Jos. “Transient diffusion of ion implanted B in Si: Dose, time and matrix dependence of atomic and electrical profiles”. *Journal of Applied Physics* **68**(12), 6191 (1990).

[27] N.E.B. Cowern, G. Mannino, P.A. Stolk, F. Roozeboom, H. G. A. Huizing, and J. G. M. van Berkum. “Energetics of self-interstitial clusters in si”. *Physics Review Letters* **82**(22), 4460 (1999).

[28] N.E.B. Cowern, G.F.A. van de Walle, P.C. Zalm, and D.W.E. Vandenhoudt. “Mechanisms of implant damage annealing and transient enhanced diffusion in Si”. *Applied Physics Letters* **65**(23), 2981 (1994).

[29] P.S. Dobson. “On phosphorus diffusion in silicon under oxidizing atmospheres”. *Philosophical Magazine* **24**, 567 (1971).

[30] D. F. Downey, S. F. Felch, and S. W. Falk. “Doping and annealing requirements to satisfy the 100 nm technology node”. In **Advances in Rapid Thermal Processing**, Electrochemical Society, 101 (1999).

[31] S.T. Dunham. “Interactions of silicon point defects with silicon oxide films”. *Journal of Applied Physics* **71**, 685 (1991).

[32] S.T. Dunham, Iuval Clejan, and A. H. Gencer. “Accurate and efficient modeling of nucleation and growth processes”. *Materials Science and Engineering A* **238**, 152 (1997).

[33] S. T. Dunham. “A quantitative model for the coupled diffusion of phosphorus and point defects in silicon”. *Journal of Electrochemical Society* **139**, 2628 (1992).

[34] S. T. Dunham, S. Chakravarthi, and Alp H. Gencer. “Beyond TED: Understanding boron shallow junction formation”. In **International Electron Devices Meeting 1998, Technical Digest**, IEEE, (1998).

[35] D.J. Eaglesham, P.A. Stolk, H.J. Gossmann, and J.M. Poate. “Implantation and transient B diffusion in Si: The source of the interstitials”. *Applied Physics Letters* **65**(18), 2305 (1994).

[36] D. J. Eaglesham, T. E. Haynes, H. J. Gossmann, D. C. Jacobson, P. A. Stolk, and J. M. Poate. “Transient enhanced diffusion of Sb and B due to mev silicon implants”. *Applied Physics Letters* **70**(24), 3281 (1997).

[37] P. Fahey, P. B. Griffin, and J. D. Plummer. “Point defects and dopant diffusion in silicon”. *Reviews of Modern Physics* **61**(2), 289 (1989).

[38] R.B. Fair, J.J. Wortman, and J. Liu. “Modeling rapid thermal annealing processes for shallow junction formation in silicon”. In **Internatinal Electron Device Meeting (IEDM) Technical Digest**, 658 (1983).

[39] B. Garben, W. A. Orr-Arienzo, and R. F. Lever. “Investigation of boron diffusion from polycrystalline silicon”. *Journal Electrochemical Society* **133**, 2152 (1986).

[40] A.H. Gencer, S. Chakravarthi, I. Clejan, and S.T. Dunham. “Fundamental modeling of transient enhanced diffusion through extended defect evolution”. In **Defects and Diffusion in Silicon Processing**, Materials Research Society, 359 (1997).

[41] A.H. Gencer and S.T. Dunham. “A predictive model for transient enhanced diffusion based on evolution of $\{311\}$ defects”. *Journal of Applied Physics* **81**(2), 631 (1997).

[42] A.H. Gencer and S.T. Dunham. “Modeling extended defect formation and dissolution: Analytic formulation of kinetic precipitation model”. In **Si Front-End Processing-Physics and Technology of Dopant-Defect Interactions**, Materials Research Society, (1999).

[43] A. H. Gencer. “Modeling and simulation of transient enhanced diffusion based on interactions of point and extended defects”. Ph.D. thesis, Boston University (1999).

[44] M.D. Giles. SIMS data from Intel Corporation.

[45] M.D. Giles. “Defect-coupled diffusion at high concentrations”. *IEEE transactions on computer-aided design of integrated circuits and systems* **8**, 460 (1989).

[46] M.D. Giles. “Transient phosphorus diffusion below the amorphization threshold”. *Journal of Electrochemical Society* **138**(4), 1160 (1991).

[47] M.D. Giles, H.W. Kennel, P.A. Packan, and S. Yu. “Modeling silicon implantation damage and transient enhanced diffusion effects for silicon technology development”. In **Defects and Diffusion in Silicon Processing**, Materials Research Society, 253 (1997).

[48] U. Gösele, W. Frank, and A. Seeger. *Applied Physics* **23**, 361 (1980).

[49] U. Gösele, A. Plößl, and T.Y. Tan. In **Defects in Semiconductors**, Electrochemical Society Proceedings, 309 (1996).

[50] U. Gösele and H. Strunk. *Applied Physics* **20**, 263 (1979).

[51] U. Gösele and T.Y. Tan. In **Defects in Semiconductors II**, North-Holland, New York, 45 (1983).

[52] H.-J. Gossmann. “Dopants and intrinsic point-defects during Si device processing”. In **Semiconductor Silicon 1998**, Electrochemical Society Proceedings, 884 (1998).

[53] H. J. Gossmann, T. E. Haynes, P. A. Stolk, D. C. Jacobson, G. H. Gilmer, J. M. Poate, H. S. Luftman, T. K. Mogi, and M. O. Thompson. “The interstitial fraction of diffusivity of common dopants in Si”. *Applied Physics Letters* **71**(26), 3862 (1997).

[54] H.-J. Gossmann, T. E. Haynes, P. A. Stolk, D. C. Jacobson, G. H. Gilmer, J. M. Poate, H. S. Luftman, T. K. Mogi, and M. O. Thompson. “The interstitial fraction of diffusivity of common dopants in Si”. *Applied Physics Letters* **71**, 3862 (1997).

[55] T.E. Haynes, D.J. Eaglesham, P.A. Stolk, H.J. Gossmann, D.C. Jacobson, and J.M. Poate. “Interactions of ion-implantation-induced interstitials with boron at high concentrations in silicon”. *Applied Physics Letters* **69**(10), 1376 (1996).

[56] S. B. Herner, H. J. Gossmann, L. P. Pelaz, G. H. Gilmer, M. Jaraiz, and D. C. Jacobson. “Ion mass influence on transient enhanced diffusion and boron clustering in silicon: Deviation from the ”+1” model”. *Journal of Applied Physics* **83**(11), 6182 (1998).

[57] R.T. Hodgson, V.R. Deline, S. Mader, and J.C. Gelpey. “Rapid thermal annealing of boron-implanted silicon using an ultrahigh power arc lamp”. *Applied Physics Letters* **44**, 589 (1984).

[58] S.M. Hu and S. Schmidt. *Journal of Applied Physics* **39**, 4273 (1968).

[59] M. Jaraiz, G. H. Gilmer, J. M. Poate, and T. D. de la Rubia. “Atomistic calculations of ion implantation in Si: Point defect and transient enhanced diffusion phenomena”. *Applied Physics Letters* **68**(3), 409 (1996).

[60] M. J.Caturla, M. D. Johnson, and T. D. de la Rubia. “The fraction of substitutional boron in silicon during ion implantation and thermal annealing”. *Applied Physics Letters* **72**(21), 2736 (1998).

[61] R. Kalyanaramana, T. E. Haynes, V. C. Venezia, D. C. Jacobson, H.-J. Gossmann, and C. S. Rafferty. “Quantification of excess vacancy defects from high-energy ion implantation in Si by Au labeling”. *Applied Physics Letters* **76**, 3379 (2000).

[62] K. M. Klein, C. Park, and A.F. Tasch. “Modeling of cumulative damage effects on ion implantation in silicon”. *Nuclear Instruments Physics Letters* **B59/60**, 60 (1991).

[63] J.B. Lasky. “Rapid isothermal annealing of boron ion implanted junctions”. *Applied Physics Letters* **54**, 6009 (1983).

[64] T. J. Lenosky, S. K. Theiss, and T.D. de la Rubia. “Private communication”.

[65] W. Lerch, M. Glück, N. A. Stolwijk, H. Walk, M. Schäfer, S. D. Marcus, D. F. Downey, J. W. Chow, and H. Marquardt. “Simulation of rapid thermal annealed boron ultra-shallow junctions in inert and oxidizing ambients”. In **Rapid Thermal and Integrated Processing VII**, Materials Society Proceedings, (1998).

[66] W. Lerch, N. A. Stolwijk, H. Mehrer, and Ch. Poisson. “Diffusion of platinum into dislocated and non-dislocated silicon”. *Semiconductor Science and Technology* **10**(9), 1257 (1995).

[67] A.D. Lilak, S.K. Earles, K.S. Jones, M. E. Law, and M. D. Giles. “A physics-based modeling approach for the simulation of anomalous boron diffusion and clustering behaviors”. In **Internatinal Electron Device Meeting (IEDM) Technical Digest**, IEEE, 493 (1997).

[68] G. Mannino, N.E.B. Cowern, F. Roozeboom, and J. G. M. van Berkum. “Role of self- and boron-interstitial clusters in transient enhanced diffusion in silicon”. *Applied Physics Letters* **76**(7), 855 (2000).

[69] G. Masetti, S. Solmi, and G. Soncini. “The effect of oxidation on anomalous diffusion in silicon”. *Solid-State Electronics* **16**, 1419 (1973).

[70] D. Mathiot. “Gold, self-, and dopant diffusion in silicon”. *Physics Review B* **45**(23), 13345 (1992).

[71] D. Mathiot and J. C. Pfister. “Influence of the nonequilibrium vacancies on the diffusion of phosphorus into silicon”. *Journal of Applied Physics* **53**, 3035 (1982).

[72] D. Mathiot and J. C. Pfister. “Dopant diffusion in silicon: A consistent view involving nonequilibrium defects”. *Journal of Applied Physics* **55**(10), 3518 (1984).

[73] M. Miyake and S. Aoyama. "Transient enhanced diffusion of ion implanted boron in Si during rapid thermal annealing". *Journal of Applied Physics* **63**(5), 1754 (1988).

[74] F. Morehead. In **Defects in Electronic Materials**, Materials Society Proceedings, 99 (1987).

[75] F. Morehead. In **Defects in Electronic Materials**, Materials Society Proceedings, 99 (1988).

[76] J. Narayan, O.W. Holland, R.E. Eby, J.Y. Wortman, V. Ozguz, and G. A. Rozgonyi. "Rapid thermal annealing of arsenic and boron-implantedsilicon". *Applied Physics Letters* **43**, 957 (1983).

[77] C.S. Nichols, C.G. Van de Walle, and S.T. Pantelides. "Mechanisms of dopant impurity diffusion in silicon". *Physics Review B* **40**, 5484 (1989).

[78] G.S. Oehrlein, S.A. Cohen, and T.O. Sedgwick. "Diffusion of phosphorus during rapid thermal annealing of ion-implanted silicon". *Applied Physics Letters* **45**, 417 (1984).

[79] P.A. Packan. "Physical modeling of transient diffusion effects in silicon due to surface oxidation and ion-implantation". Ph.D. thesis, Stanford University (1991).

[80] P.A. Packan and J.D. Plummer. "Transient diffusion of low-concentration B in Si due to ^{29}Si implantation damage". *Applied Physics Letters* **56**(18), 1787 (1990).

[81] G.Z. Pan, K.N. Tu, and S. Prussin. "Size distribution of end-of-rage dislocation loops in silicon-implanted silicon". *Applied Physics Letters* **68**(12), 1654 (1996).

[82] L. Pelaz, G.H. Gilmer, H.-J. Gossmann, C. S. Rafferty, M. Jaraiz, and J. Barbolla. "B cluster formation and dissolution in Si: A scenario based on atomistic modeling". *Applied Physics Letters* **74**(24), 3657 (1999).

[83] L. Pelaz, M. Jaraiz, G. H. Gilmer, H. J. Gossmann, C. S. Rafferty, and D. J. Eaglesham. "B diffusion and clustering in ion implanted Si: The role of B cluster precursors". *Applied Physics Letters* **70**(17), 2285 (1997).

[84] L. Pelaz, V.C. Venezia, H.-J. Gossmann, G.H. Gilmer, A.T. Fiory, C.S. Rafferty, M. Jaraiz, and J. Barbolla. "Activation and deactivation of implanted B in Si". *Applied Physics Letters* **75**(24), 662 (1999).

[85] E. G. Roth, O.W. Holland, and A. Meldrum. "Manipulating ion-induced defects to improve implantation processing of silicon". In **Silicon Materials Science and Technology**, Electrochemical Society, 938 (1998).

[86] B. Sadigh, T.J. Lenosky, S.K. Theiss, M.J. Caturla, T.D. de la Rubia, and M.A. Foad. "Mechanism of boron diffusion in silicon: An *ab initio* and kinetic monte carlo study". *Physics Review Letters* **83**, 4341 (1999).

[87] T.E. Seidel and A.U. MacRae. "Isothermal annealing of boron implanted silicon". In **First International Conference on Ion Implantation**, 149 (1971).

[88] M. Servidori, R. Angelucci, F. Cembali, P. Negrini, S. Solmi, P. Zaumsteil, and U. Winter. "Retarded and enhanced dopant diffusion in silicon related implantation induced excess vacancies and interstitials". *Journal of Applied Physics* **61**(5), 1834 (1987).

[89] R.O. Simmons and R.W. Ballafi. *Physics Review* **117**, 52 (1960).

[90] S. Solmi and F. Baruffaldi. "Diffusion of boron in silicon during post-implantation annealing". *Journal of Applied Physics* **69**(4), 2135 (1991).

[91] P. A. Stolk, H.-J. Gossmann, D. J. Eaglesham, D. C. Jacobson, J. M. Poate, and H. S. Luftman. "Trap-limited interstitial diffusion and enhanced boron clustering in silicon". *Applied Physics Letters* **66**(5), 568 (1995).

[92] A. Sultan, S. Banerjee, S. List, and V. McNeil. "An approach using a subamorphizing threshold dose silicon implant of optimal energy to achieve shallower junctions". *Journal of Applied Physics* **83**(12), 8046 (1998).

[93] S. Takeda, M. Kohyama, and K. Ibe. "Interstitial defects on $\{311\}$ in Si and Ge: line defect configuration incorporated with a self interstitial atom chain". *Philosophical Magazine A* **70**(2), 28 (1994).

[94] M. Tang, L. Colombo, J. Zhu, and T. Diaz de la Rubia. "Intrinsic point defects in crystalline silicon: Tight-binding molecular dynamics studies of self-diffusion, interstitial-vacancy recombination, and formation volumes". *Physics Review B* **55**(21), 14279 (1997).

[95] W. Taylor and U. Gösele. In **Process Physics and Modeling in Semiconductor Technology**, Electrochemical Society Proceedings Pennington, NJ, 108 (1993).

[96] V. C. Venezia, D. J. Eaglesham, T. E. Haynes, A. Agarwal, D. C. Jacobson, H. J. Gossmann, and F. H. Baumann. "Depth profiling of vacancy clusters in mev-implanted Si using Au labeling". *Applied Physics Letters* **73**(20), 2980 (1998).

[97] G. D. Watkins. In **Radiation Damage in Semiconductors**, 97 (1965).

[98] W. Windl, M. M. Bunea, R. Stumpf, S. T. Dunham, and M. P. Masquelier. "First-principles study of boron diffusion in silicon". *Physics Review Letters* **83**, 4345 (1999).

[99] F. Wittel. “Development and characterization of process simulation models for diffusion and co-diffusion of dopants in silicon”. Ph.D. thesis, Boston University (1995).

[100] M. Yoshida. *Japanese Journal of Applied Physics* **18**, 479 (1979).

[101] M. Yoshida. *Japanese Journal of Applied Physics* **22**, 1404 (1983).

[102] J. Zhu, M.-J. Caturla, M. Johnson, and T.D. de la Rubia. “Private communication”.

[103] J. Zhu, M.-J. Caturla, M. Johnson, and T.D. dela Rubia. “Ab initio pseudopotential calculations of B diffusion and pairing in Si”. *Physics Review B* **54**, 4741 (1996).

[104] H. Zimmermann. “Accurate measurement of the vacancy equilibrium concentration in silicon”. *Applied Physics Letters* **59**(24), 3133 (1991).

[105] H. Zimmermann and H. Ryssel. “Direct determination of point-defect equilibrium concentrations”. *Physics Review B* **44**(16), 9064 (1991).

[106] H. Zimmermann and H. Ryssel. “Observation of inverse u-shaped profiles after platinum diffusion in silicon”. *Applied Physics Letters* **59**(10), 1209 (1991).

[107] H. Zimmermann and H. Ryssel. *Applied Physics A* **55**, 121 (1992).

[108] H. Zimmermann and H. Ryssel. “Gold and platinum diffusion: The key to the understanding of point defect behavior in silicon”. *Applied Physics A* **55**, 121 (1992).

[109] H. Zimmermann and H. Ryssel. “Modeling of platinum diffusion in silicon under non-equilibrium conditions”. *Journal of Electrochemical Society* **139**(1), 256 (1992).

VITA

EDUCATION

- **Ph.D. in Manufacturing Engineering** **2001**
  Boston University, Department of Manufacturing Engineering, Boston, MA.
- **Bachelor of Technology in Metallurgical Engineering** **1995**
  Institute of Technology, Banaras Hindu University, Varanasi, India.

EXPERIENCE

- **Boston University,** Boston, MA **1996–2000**
  Research Assistant for Assoc. Prof. Scott Dunham in the Department of Electrical and Computer Engineering.
- **Intel Corporation,** Hillsboro, OR **1997**
  TCAD Engineer (summer intern).
- **Boston University,** Boston, MA **1995–1996**
  Teaching Assistant in the Department of Manufacturing Engineering.

PUBLICATIONS

- **S. Chakravarthi** and S.T. Dunham, "A Simple Continuum Model For Boron Clustering Based on Atomistic Calculations", Submitted (after revision) J. Appl. Phys., (2000).
- **S. Chakravarthi** and S.T. Dunham, A Physical Model for Simulation of Vacancy Clusters in Ion Implanted Silicon, in Preparation. to be submitted to J. Appl. Phys.
- S.T. Dunham, A.H. Gencer and **S. Chakravarthi**, "Modeling of Dopant Diffusion in Silicon", IEICE Trans. Electron. E82C (6) 800-812 June (1999).
- **S. Chakravarthi** and S.T. Dunham, "Modeling of Boron Deactivation/Activation Kinetics during Ion-implant Annealing", International Conference on Simulation of Semiconductor Process and Devices (SISPAD) 2000, Technical Digest, (2000).
- **S. Chakravarthi**, A.H. Gencer, S.T. Dunham and D.F. Downey, "Understanding and Modeling Ramp Rate Effects on Shallow Junction Formation", Si Front-End Processing Physics and Technology of Dopant-Defect Interactions II, Materials Research Society Proceedings, (2000).
- **S. Chakravarthi** and S. T. Dunham, "Modeling Of Vacancy Cluster Formation in Ion Implanted Silicon", in Fifth Intl. Symp. On Process Phys. and Modeling in Semiconductor Device Manufacturing, Electrochemical Society Meeting Proceedings, (1999).

- **S. Chakravarthi** and S. T. Dunham, “A Simple Continuum Model for Simulation of Boron Interstitial Clusters based on Atomistic Calculations”, International Conference on Simulation of Semiconductor Process and Devices (SISPAD) 1998, Technical Digest, p.55 (1998).
- S. T. Dunham, **S. Chakravarthi**, and Alp H. Gencer, Beyond TED: Understanding Boron Shallow Junction Formation, In International Electron Devices Meeting 1998, Technical Digest, IEEE (1998).
- **S. Chakravarthi** and S. T. Dunham , “Point Defect Properties From Metal Diffusion Experiments - What does the data really tell us”, in Defects and Diffusion in Silicon Processing, V.469 (Materials Research Society Proceedings, Pittsburgh, PA, 1997)
- **S. Chakravarthi** and S. T. Dunham, Influence of Extended Defect Models on Prediction of Boron Transient Enhanced Diffusion, In Silicon Front End Technology — Materials Processing and Modeling EE3.5, (Materials Research Society Meeting, 1998).
- A.H. Gencer, **S. Chakravarthi**, I. Clejan and S.T. Dunham, Fundamental Modeling of Transient Enhanced Diffusion through Extended Defect Evolution, in Defects and Diffusion in Silicon Processing, V. 469 (Materials Research Society Proceedings, Pittsburgh, PA, 1997)
- A.H. Gencer, **S. Chakravarthi** and S.T. Dunham, Physical Modeling of Transient Enhanced Diffusion and Dopant Deactivation via Extended Defect Evolution, International Conference on Simulation of Semiconductor Process and Devices (SISPAD) 1997, Technical Digest, (IEEE, Piscataway, NJ, 1997).